Available online at www.sciencedirect.com
ScienceDirect
Comput. Methods Appl. Mech. Engrg. 318 (2017) 148–192
Computer methods in applied mechanics and engineering
www.elsevier.com/locate/cma

Some basic formulations of the virtual element method (VEM) for finite deformations

H. Chi[a], L. Beirão da Veiga[b], G.H. Paulino[a,*]

[a] School of Civil and Environmental Engineering, Georgia Institute of Technology, 790 Atlantic Drive, Atlanta, GA, 30332, USA
[b] Dipartimento di Matematica e Applicazioni, Università di Milano–Bicocca, Via Cozzi 53, I-20153, Milano, Italy

Received 10 August 2016; received in revised form 5 December 2016; accepted 12 December 2016
Available online 21 December 2016

Dedicated to the memory of Professor William S. Klug (1976–2016)

Highlights

- General Virtual Element Method (VEM) framework for finite elasticity.
- The VEM displacement spaces allow exact computation of element-level volume changes.
- New stabilization term captures large and highly localized deformations.
- Convergence and accuracy of the VEM are verified.
- An engineering application of the VEM is demonstrated.

Abstract

We present a general virtual element method (VEM) framework for finite elasticity, which emphasizes two issues: element-level volume change (volume average of the determinant of the deformation gradient) and stabilization. To address the former issue, we provide exact evaluation of the average volume change in both 2D and 3D on properly constructed local displacement spaces. For the later issue, we provide a new stabilization scheme that is based on the trace of the material tangent modulus tensor, which captures highly heterogeneous and localized deformations. Two VEM formulations are presented: a two-field mixed and an equivalent displacement-based, which is free of volumetric locking. Convergence and accuracy of the VEM formulations are verified by means of numerical examples, and engineering applications are demonstrated.

Keywords: Virtual element method (VEM); Finite elasticity; Mixed variational principle; Filled elastomers

1. Introduction

In this paper, we put forth a Virtual Element Method (VEM) framework for finite elasticity problems. The introduced VEM framework allows for general two-dimensional polygonal and three-dimensional polyhedral meshes.

* Corresponding author.
E-mail addresses: hchi6@gatech.edu (H. Chi), lourenco.beirao@unimib.it (L.B. da Veiga), paulino@gatech.edu (G.H. Paulino).

http://dx.doi.org/10.1016/j.cma.2016.12.020

Two VEM formulations are presented: a two-field mixed VEM formulation and an equivalent displacement-based VEM formulation, which is free of volumetric locking. We highlight that both VEM formulations utilize the average volume change (the volume average of the determinant of the deformation gradient) in the element level, which can be computed exactly for both polygonal and polyhedral virtual elements under any given deformation fields. For polyhedral virtual elements, the local displacement space is properly constructed such that the average volume change can be exactly computed. We study various choices of constructing the loading terms and the stabilization terms for the VEMs. A new stabilization scheme is further proposed for isotropic materials, which is based on the trace of the material tangent modulus tensor. We conduct thorough numerical assessments to evaluate the convergence of the proposed VEM. Through an application example, the performance of the proposed VEM is demonstrated in a problem that involves heterogeneous and localized deformations.

This paper is inspired by the original work of Bill Klug [1]. The remainder of this paper is organized as follows. Section 2 provides motivations of this paper and summarizes the related work in the VEM literature. Section 3 reviews the displacement-based and two-field mixed variational principles for finite elasticity. Section 4 introduces the constructions of displacement and pressure VEM spaces, together with derivations of the exact average volume changes of virtual elements under given displacement fields. In Section 5, a two-field mixed VEM approximation and its equivalent displacement-based counterpart are presented together with detailed discussion on the construction of loading and stability terms. A new stabilization scheme is also proposed in this section. Several numerical assessments are presented in Section 6 to evaluate the convergence as well as the accuracy of the proposed VEM approximations. In Section 7, a two dimensional application example is presented, which studies the nonlinear elastic response of a filled elastomer, to showcase and evaluate the performance of the VEM formulations in problems involving large heterogeneous and localized deformations. Section 8 contains several concluding remarks and future research directions. Three Appendices complement the paper. A complete list of the notation adopted in this paper is provided in the nomenclature in Appendix C.

2. Motivation and related work

Due to their unique and intriguing properties, polygonal and polyhedral elements have been attracting high level of attention in the computational mechanics community. Despite their relatively short history of development, polygonal and polyhedral finite elements have been successfully applied to several fields of computational mechanics and have revealed several advantages over classical finite elements, i.e., triangular/tetrahedral and quadrilateral/brick elements. For instance, polygonal and polyhedral finite elements have been shown to better capture crack propagation and branching in computational fracture simulations [2–5], to produce numerically stable results in topology optimization [6–8] and fluid mechanics [9], and to better model contact [10] and arbitrary internal interface [11] in large deformation elasto-plasticity problems. Furthermore, recent studies have demonstrated that polygonal finite elements also possess great potential in the study of two-dimensional finite elasticity problems [12,13]. More specifically, from a geometrical point of view, polygonal finite elements are well suited to modeling complex microstructures, such as porous or particulate microstructures and microstructures involving different length scales, and to dealing with periodic boundary conditions (introducing hanging nodes). From an analysis point of view, two-field mixed polygonal finite elements are found to be numerically stable on Voronoi-type meshes, to produce more accurate results, and to be more tolerant to large localized deformations.

On the other hand, polygonal and polyhedral finite elements also suffer from drawbacks. First, while the performance of the finite element results strongly depends on the quality of the shape functions, the use of polygonal and polyhedral elements with general shapes, such as concave polyhedrons, is limited by the availability of well-defined shape functions. Particularly in 3D, most of the existing shape functions for polyhedral finite elements are either restrictive in element geometries or computationally expensive to compute. For instance, although closed-form expressions are available, the Wachspress shape functions are restricted to strictly convex and simple polyhedrons (meaning the collection of faces that include each vertex consists of exactly three faces) [14], and the Mean Value coordinates are mainly applicable to polyhedrons with simplicial faces [15]. In contrast, while allowing for more general polyhedrons (e.g., concave ones), harmonic shape functions [16–18] and max-entropy shape functions [19–21] need to be computed numerically at the quadrature points element by element. Moreover, especially for nonlinear and three-dimensional problems, efficient yet consistent numerical quadrature rules on general polygons and polyhedrons

are difficult to construct and typically contain numerous quadrature points (see [22–24] for some recent work to alleviate this issue), which is also undesirable from a computational perspective.

The Virtual Element Method (VEM) has been recently introduced as a generalization of the finite element method (FEM). The VEM is able to handle general polygonal and polyhedral meshes [25,26] as it abstracts from the shape functions, which are essential to any FEM approximation. Unlike FEM, the shape functions in VEM are constructed implicitly, and the approximations of the weak forms are decomposed into consistency and stability terms, both of which are directly computed from the degrees of freedoms (DOFs) of the unknown fields. By doing this, only numerical quadratures of polynomials (and not of more complex functions) are needed in VEM. These favorable features make the VEM an attractive framework to efficiently deal with general meshes in 2D and 3D. While most of the studies in the VEM literature consider linear problems in 2D (see, e.g. [25,27–30,26,31–34]), some attempts have been made for nonlinear [35,36] and 3D [30] problems. In the context of structural mechanics, VEM has been introduced in [27] for (possibly incompressible) two dimensional linear elasticity, in [30] for three dimensional linear elasticity, in [35] for general two dimensional elastic and inelastic problems under small deformations, and in [37] for simple contact problems.

The goal of this paper is to put forward a VEM framework for finite elasticity problems, which is capable of handling general polygonal and polyhedral elements, including concave ones, in both 2D and 3D. Two formulations are presented: a two-field mixed VEM formulation, which involves an additional pressure field, and an equivalent displacement-based VEM formulation, which is numerically shown to be free of volumetric locking on a wide class of meshes (as opposed to the standard displacement-based FEM). Both formulations make use of the exact average volume change (the volume average of the determinant of the deformation gradient) of each element, the analytical expressions of which are derived in both 2D and 3D cases under given displacement fields. For polyhedral elements in 3D, the analytical expression for this average volume change is obtained through a proper definition of the local displacement VEM space. In both 2D and 3D, the VEM formulations are shown to deliver optimally convergent results, even for meshes with non-convex elements. Moreover, since nonlinear elastic materials are characterized by non-convex stored-energy functions as a result of the large reversible deformation, the stabilization term plays a crucial role on the performance of the VEM. *We study various choices of the stabilization term and discuss their influence on the performance in finite elasticity VEM problems. We also propose a new stabilization scheme for isotropic materials, which is based on the trace of the material tangent modulus tensor*. A two dimensional practical application example is presented, which addresses the nonlinear elastic response of a filled elastomer, and demonstrates the performance proposed VEM formulations in a problem that involves large heterogeneous and localized deformations.

3. Theoretical background

This section revisits the variational principles for finite elastostatics [38]. Displacement-based and two field mixed variational principles are presented. Throughout, Lagrangian description of the fields is adopted.

Consider an elastic solid that occupies a domain $\Omega \in \mathbb{R}^d$ with $\partial\Omega$ being its boundary in its stress-free, undeformed configuration and d being the dimension. It is subjected to a prescribed displacement field $\mathbf{u}^0$ on $\Gamma^{\mathbf{X}}$ and a prescribed surface traction $\mathbf{t}$ (per unit undeformed surface) on $\Gamma^{\mathbf{t}}$, such that $\Gamma^{\mathbf{X}} \cup \Gamma^{\mathbf{t}} = \partial\Omega$ and $\Gamma^{\mathbf{X}} \cap \Gamma^{\mathbf{t}} = \varnothing$ for a well-posed problem. Additionally, we also prescribe a body-force $\mathbf{f}$ (per unit undeformed volume) in the solid. A stored-energy function W is used to characterize the constitutive behavior of the body, which is assumed to be an objective function of the deformation gradient tensor $\mathbf{F}$. Throughout this paper, we further assume that the stored energy function is composed of two terms, namely,

$$W(\mathbf{X}, \mathbf{F}) = \Psi(\mathbf{X}, \mathbf{F}) + U(\mathbf{X}, J). \tag{1}$$

U is the volumetric part of the stored energy function that depends only on $J = \det\mathbf{F}$, such that (i) U is strictly convex (at least in the neighborhood of $J = 1$); (ii) U achieves minimum 0 at $J = 1$, and (iii) $U \to +\infty$ as $J \to +\infty$. For instance, in the case of purely incompressible solids, U takes the form

$$U(\mathbf{X}, J) = \begin{cases} 0 & \text{if } J = 1 \\ +\infty & \text{otherwise.} \end{cases} \tag{2}$$

Once $\mathbf{U}(\mathbf{X}, J)$ is identified, $\Psi(\mathbf{F})$ is the remaining term of the stored-energy function $W(\mathbf{F})$. The first Piola–Kirchhoff stress tensor $\mathbf{P}$ at each material point $\mathbf{X} \in \Omega$ is given by the following relation:

$$\mathbf{P}(\mathbf{X}) = \frac{\partial W}{\partial \mathbf{F}}(\mathbf{X}, \mathbf{F}) = \frac{\partial \Psi}{\partial \mathbf{F}}(\mathbf{X}, \mathbf{F}) + \frac{\partial U}{\partial \mathbf{F}}(\mathbf{X}, J) \tag{3}$$

which is used as the stress measure of choice in this paper.

3.1. Displacement-based variational principle

In the displacement-based formulation, the displacement field $\mathbf{u}$ is taken to be the only independent variable. The deformation gradient $\mathbf{F}$ is then assumed to be dependent on $\mathbf{u}$ through $\mathbf{F}(\mathbf{u}) = \mathbf{I} + \nabla\mathbf{u}$, where ∇ denotes the gradient operator with respect to the undeformed configuration and $\mathbf{I}$ stands for identity in the space of second order tensors. Similarly, J depends on $\mathbf{u}$ through $J(\mathbf{u}) = \det\mathbf{F}(\mathbf{u})$. Based on the principle of minimum potential energy, the displacement-based formulation consists of seeking the unknown displacement $\mathbf{u}$ which minimize the potential energy Π among all the kinematically admissible displacements $\mathbf{v}$

$$\Pi(\mathbf{u}) = \min_{\mathbf{v}\in\mathcal{K}} \Pi(\mathbf{v}), \tag{4}$$

with

$$\Pi(\mathbf{v}) = \int_\Omega [\Psi(\mathbf{X}, \mathbf{F}(\mathbf{v})) + U(\mathbf{X}, J(\mathbf{v}))]\, d\mathbf{X} - \int_\Omega \mathbf{f}\cdot\mathbf{v} d\mathbf{X} - \int_{\Gamma^{\mathbf{t}}} \mathbf{t}\cdot\mathbf{v} dS, \tag{5}$$

where $\mathcal{K}$ stands for the set of kinematically admissible displacements such that $\mathbf{v} = \mathbf{u}^0$ on $\Gamma^{\mathbf{X}}$.

The weak form of the Euler–Lagrange equations of the minimization problem is given by

$$\begin{aligned} G(\mathbf{v}, \delta\mathbf{v}) = &\int_\Omega \left[\frac{\partial \Psi}{\partial \mathbf{F}}(\mathbf{X}, \mathbf{F}(\mathbf{v})) + \frac{\partial U}{\partial \mathbf{F}}(\mathbf{X}, J(\mathbf{v}))\right] : \nabla(\delta\mathbf{v}) d\mathbf{X} \\ &- \int_\Omega \mathbf{f}\cdot\delta\mathbf{v} d\mathbf{X} - \int_{\Gamma^{\mathbf{t}}} \mathbf{t}\cdot\delta\mathbf{v} dS = 0 \quad \forall\delta\mathbf{v}\in\mathcal{K}^0, \end{aligned} \tag{6}$$

where the trial displacement field $\delta\mathbf{v}$ is the variation of $\mathbf{v}$, and $\mathcal{K}^0$ denotes the set of all the kinematically admissible displacement fields that vanish on $\Gamma^{\mathbf{X}}$.

3.2. A general two-field mixed variational principle

For nearly and purely incompressible materials, the two-field mixed variational principle is typically utilized. Under the assumption of (1), different types of two-field mixed variational principles can be derived based on different forms of the decompositions. In the $\mathbf{F}$-formulation, Ψ is assumed to be a general function on $\mathbf{F}$, i.e., no multiplicative decomposition of the deformation gradient is used, whereas, in the commonly used $\overline{\mathbf{F}}$-formulation, Ψ is assumed to solely depend on the deviatoric part of the deformation gradient, that is, $\overline{\mathbf{F}} = J^{-1/3}\mathbf{F}$. In the latter case, Ψ is the stored energy induced by the deviatoric component of the deformation.

This section briefly reviews the $\mathbf{F}$-formulation proposed in [12]. For the $\overline{\mathbf{F}}$-formulation, the derivation follows similar procedures and therefore is not presented here. The interested readers are referred to [39,40,38,41,42] and references therein.

The basic idea is to introduce a Legendre transformation of the term $U(J)$ in the stored-energy function as follows [12]

$$\widehat{U}^*(\mathbf{X}, \widehat{q}) = \max_J \widehat{q}(J-1) - U(\mathbf{X}, J). \tag{7}$$

Since $U(J)$ is assumed to be convex over J, then the duality of the transformation yields

$$U(\mathbf{X}, J) = \max_{\widehat{q}} \widehat{q}(J-1) - \widehat{U}^*(\mathbf{X}, \widehat{q}). \tag{8}$$

Direct substitution of (8) into the displacement-based formulation (4) and (5) renders the following two-field mixed variational principle, which seeks the unknown displacement field $\mathbf{u}$ and pressure-like field $\widehat{p}$ such that

$$\widehat{\Pi}(\mathbf{u}, \widehat{p}) = \min_{\mathbf{v}\in\mathcal{K}} \max_{\widehat{q}\in\mathcal{Q}} \widehat{\Pi}(\mathbf{v}, \widehat{q}), \tag{9}$$

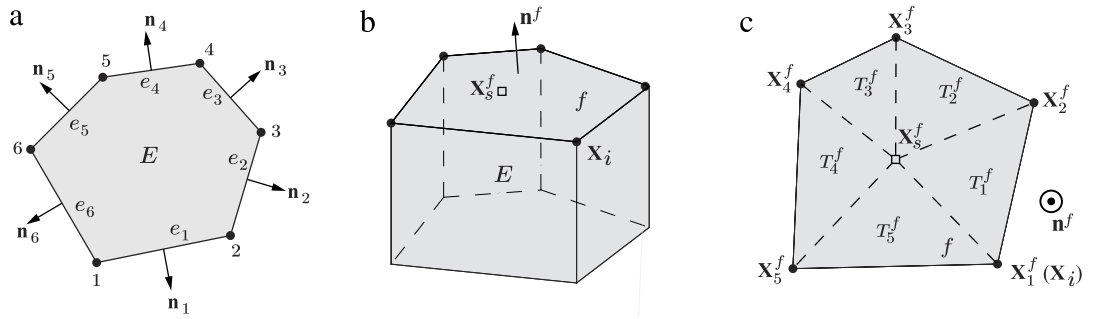

Fig. 1. Illustration of (a) a two dimensional polygonal element E in its undeformed configuration, (b) a three dimensional polyhedral element E in its undeformed configuration, and (c) a generic face f of the polyhedral element E.

where $\widehat{\Pi}(\mathbf{v}, \widehat{q})$ is of the form

$$\widehat{\Pi}(\mathbf{v}, \widehat{q}) = \int_{\Omega} \left\{ \Psi(\mathbf{X}, \mathbf{F}(\mathbf{v})) + \widehat{q}\,[J(\mathbf{v}) - 1] - \widehat{U}^*(\mathbf{X}, \widehat{q}) \right\} \mathrm{d}\mathbf{X} - \int_{\Omega} \mathbf{f} \cdot \mathbf{v} \mathrm{d}\mathbf{X} - \int_{\Gamma^{\mathbf{t}}} \mathbf{t} \cdot \mathbf{v} \mathrm{d}S, \tag{10}$$

and $\mathcal{Q}$ denotes the set of square-integrable functions. Unlike the commonly adopted $\overline{\mathbf{F}}$-formulation, whose unknown pressure field is the equilibrium Cauchy hydrostatic pressure field $p \doteq \mathrm{tr}\boldsymbol{\sigma}$, the additional unknown field $\widehat{p}$ in the $\mathbf{F}$-formulation is found to be a pressure-like scalar field which relates to p through

$$p = \widehat{p} + \frac{1}{3J} \frac{\partial \Psi}{\partial \mathbf{F}} (\mathbf{X}, \mathbf{F}) : \mathbf{F}. \tag{11}$$

The weak forms of the Euler–Lagrange equations from (9) and (10) are obtained as

$$\begin{aligned} G^{\mathbf{v}}(\mathbf{v}, \widehat{q}, \delta\mathbf{v}) \;=\; & \int_{\Omega} \left[\frac{\partial \Psi}{\partial \mathbf{F}} (\mathbf{X}, \mathbf{F}(\mathbf{v})) + \widehat{q}\, \frac{\partial J}{\partial \mathbf{F}} (\mathbf{F}(\mathbf{v})) \right] : \nabla(\delta\mathbf{v}) \mathrm{d}\mathbf{X} \\ & - \int_{\Omega} \mathbf{f} \cdot \delta\mathbf{v} \mathrm{d}\mathbf{X} - \int_{\Gamma^{\mathbf{t}}} \mathbf{t} \cdot \delta\mathbf{v} \mathrm{d}S = 0 \quad \forall \delta\mathbf{v} \in \mathcal{K}^0, \end{aligned} \tag{12}$$

$$G^{\widehat{q}}(\mathbf{v}, \widehat{q}, \delta\widehat{q}) = \int_{\Omega} \left[J(\mathbf{v}) - 1 - \frac{\partial \widehat{U}^*}{\partial \widehat{q}} (\mathbf{X}, \widehat{q}) \right] \delta\widehat{q} \mathrm{d}\mathbf{X} = 0 \quad \forall \delta\widehat{q} \in \mathcal{Q}, \tag{13}$$

where the trial pressure field $\delta\widehat{q}$ is the variation of $\widehat{q}$.

4. Virtual element spaces and projection operators

Consider Ω_h to be a tessellation of the domain Ω into non-overlapping polygon/polyhedral elements with h being the maximum element size. The boundary of the mesh, denoted as Γ_h is assumed to be compatible with the applied boundary condition, that is, $\Gamma_h^{\mathbf{t}}$ and $\Gamma_h^{\mathbf{X}}$ are both unions of edges/faces of the mesh. We denote $E \in \Omega_h$ as a generic element of the mesh with e standing for its generic edge. In the three dimensional case, we also use f to denote a generic face of E. Additionally, we denote by $|E|$ the area or volume of E respectively.

4.1. Displacement VEM space and projection operators

The global virtual displacement space $\mathcal{K}_h$ associated with the mesh Ω_h is a conforming finite dimensional space that is defined as:

$$\mathcal{K}_h = \{ \mathbf{v}_h \in \mathcal{K} : \mathbf{v}_h|_E \in \mathcal{V}(E), \forall E \in \Omega_h \}, \tag{14}$$

where $\mathcal{V}(E)$ is a local VEM space defined on $E \in \Omega_h$.

Local VEM space in 2D. In two dimensions (2D), let us consider a given element E with m vertices, denoted as $\mathbf{X}_i = \{X_i, Y_i\}^T$, $i = 1, \ldots, m$, which are numbered counterclockwisely as shown in Fig. 1(a). We define the local

displacement VEM space as [25,27]

$$\mathcal{V}(E) \doteq \left\{ \mathbf{v} \in \left[\mathcal{H}^1(E)\right]^2 : \Delta \mathbf{v} = 0 \text{ in } E,\ \mathbf{v}|_e \in [\mathcal{P}_1(e)]^2\ \forall e \in \partial E \right\}, \tag{15}$$

where Δ stands for the Laplacian operator. As inferred by its definition, the VEM space contains harmonic functions which are implicitly known in the interior of E and explicitly known to possess linear variations on the edges of E. Moreover, the VEM space $\mathcal{V}(E)$ is linearly complete, namely, $[\mathcal{P}_1(E)]^2 \subseteq \mathcal{V}(E)$. In order to guarantee the continuity of the global displacement space $\mathcal{K}_h$, the DOFs of the $\mathcal{V}(E)$ are taken at the vertices of E, which are identical to those in the first order finite element spaces on general polygons.

By construction, we are able to compute the area average of the gradient of any given function $\mathbf{v} \in \mathcal{V}(E)$ using only the DOFs of $\mathbf{v}$ and geometrical information of E. Indeed, using integration by parts, for any given function $\mathbf{v}$ in $\mathcal{V}(E)$ it holds:

$$\frac{1}{|E|}\int_E \nabla \mathbf{v} \mathrm{d}\mathbf{X} = \frac{1}{|E|}\sum_{e\in\partial E}\int_e \mathbf{v} \otimes \mathbf{n}_e \mathrm{d}S, \tag{16}$$

where $\mathbf{n}_e$ is the outward norm vector associated with edge e. Realizing that the functions in $\mathcal{V}(E)$ possess linear variations on each edge of E, the edge integral on the right hand side of the above relation can be expressed as

$$\sum_{e\in\partial E}\int_e \mathbf{v} \otimes \mathbf{n}_e \mathrm{d}S = \frac{1}{2}\sum_{i=1}^{m} \mathbf{v}(\mathbf{X}_i) \cdot (|e_i|\mathbf{n}_i + |e_{i-1}|\mathbf{n}_{i-1}), \tag{17}$$

yielding

$$\frac{1}{|E|}\int_E \nabla \mathbf{v} \mathrm{d}\mathbf{X} = \frac{1}{2|E|}\sum_{i=1}^{m} \mathbf{v}(\mathbf{X}_i) \cdot (|e_i|\mathbf{n}_i + |e_{i-1}|\mathbf{n}_{i-1}) \tag{18}$$

where $|e_i|$ is the length of the ith edge, as shown in Fig. 1(a). For convenience, in the sums we follow the standard convention that $i+1 = 1$ whenever $i = m$ and $i-1 = m$ whenever $i = 1$.

Local VEM space in 3D. We proceed to define the displacement VEM space in 3D. To begin with, let us consider a polyhedron E whose boundary consists of planar faces as shown in Fig. 1(b). Suppose that E contains m vertices, which are numbered as $\mathbf{X}_i = \{X_i, Y_i, Z_i\}^T$, $i = 1, \ldots, m$. For the ith vertex $\mathbf{X}_i$, we denote $\mathcal{F}_i$ as the set of faces that are connected to it. Moreover, for any given face $f \in \partial E$ with m^f vertices, we assume that the vertices are renumbered locally as $\mathbf{X}_j^f$, $j = 1, \ldots, m^f$, such that the numbering is in a counterclockwise fashion with respect to the outward normal $\mathbf{n}^f$ pointing out of the element, as shown in Fig. 1(c). A map $\mathcal{G}_f$ is utilized to denote the relation between the global numbering and the local numbering on face f. If the ith vertex of E (with global numbering) becomes the jth vertex of f (with local numbering), we write $\mathbf{X}_j^f = \mathbf{X}^f_{\mathcal{G}_f(i)}$ or $\mathbf{X}_i = \mathbf{X}_{\mathcal{G}_f^{-1}(j)}$. Notice that for any given $f \notin \mathcal{F}_i$, $\mathcal{G}_f(i) = \emptyset$. Additionally, any given face $f \in \partial E$ is assumed to be star-convex [18] with respect to a point $\mathbf{X}_s^f$ given by

$$\mathbf{X}_s^f = \sum_{j=1}^{m^f} \beta_j^f \mathbf{X}_j^f, \tag{19}$$

where β_j^f are chosen weights that satisfy $\beta_j^f \geq 0$, $j = 1, \ldots, m^f$ and $\sum_{j=1}^{m^f} \beta_j^f = 1$. It follows that for any linear function $\mathbf{p} \in [\mathcal{P}_1(\mathbb{R})]^3$,

$$\mathbf{p}\left(\mathbf{X}_s^f\right) = \sum_{j=1}^{m^f} \beta_j^f \mathbf{p}\left(\mathbf{X}_j^f\right). \tag{20}$$

By assuming star-convexity of each face, we can introduce triangulations of all the faces $f \in \partial E$ by connecting all the vertices to $\mathbf{X}_s^f$, as shown in Fig. 1(c). We use T_j^f, $j = 1, \ldots, m^f$ to denote the triangulated subfaces of f, such that T_j^f and T_{j-1}^f are connected to vertex $\mathbf{X}_j^f$, as shown in Fig. 1(c).

The virtual space on E is defined as

$$\mathcal{V}(E) \doteq \left\{ \mathbf{v} \in \left[\mathcal{H}^1(E)\right]^3 : \mathbf{v}|_{\partial E} \in \left[C^0(\partial E)\right]^3,\ \mathbf{v}\left(\mathbf{X}_s^f\right) = \sum_{j=1}^{m^f} \beta_j^f \mathbf{v}\left(\mathbf{X}_j^f\right) \quad \text{and} \right.$$
$$\left. \mathbf{v}|_{T_j^f} \in \left[\mathcal{P}_1\left(T_j^f\right)\right]^3, \quad j = 1, \ldots, m^f,\ \forall f \in \partial E \quad \text{and} \quad \Delta \mathbf{v} = 0,\ \text{in } E \right\}. \tag{21}$$

By the above definition, the above space contains harmonic functions which are continuous and piecewise linear on each face of the element E. Moreover, due to (20), we have $[\mathcal{P}_1(E)]^3 \subseteq \mathcal{V}(E)$. As for the degrees of freedom for $\mathcal{V}(E)$, we take the pointwise values at the vertices of E; these are a valid set of DOFs for the local VEM space.

Under the definition above, the volume average of the gradient for any function $\mathbf{v}$ in $\mathcal{V}(E)$ can be computed exactly taking the steps from the 3D analog of Eq. (16):

$$\frac{1}{|E|}\int_E \nabla \mathbf{v} \mathrm{d}\mathbf{X} = \frac{1}{|E|}\sum_{f\in\partial E}\int_f \mathbf{v} \otimes \mathbf{n}^f \mathrm{d}S. \tag{22}$$

Notice that since f is assumed to be planar, its outward unit normal vector $\mathbf{n}^f$ is a constant vector. Upon realizing that $\mathbf{v}$ is piecewise linear on f, the face integral $\int_f \mathbf{v} \otimes \mathbf{n}^f \mathrm{d}S$ can be explicitly carried out by using a vertex-based quadrature rule over each triangulated face:

$$\int_f \mathbf{v} \otimes \mathbf{n}^f \mathrm{d}S = \sum_{j=1}^{m^f} \left\{ \frac{|T_j^f|}{3}\left[\mathbf{v}\left(\mathbf{X}_j^f\right) + \mathbf{v}\left(\mathbf{X}_{j+1}^f\right) + \mathbf{v}\left(\mathbf{X}_s^f\right)\right] \right\} \otimes \mathbf{n}^f, \tag{23}$$

where $|T_j^f|$ is the (signed) area of T_j^f defined as

$$|T_j^f| = \frac{1}{2}\mathbf{n}^f \cdot \left(\mathbf{X}_j^f - \mathbf{X}_s^f\right) \wedge \left(\mathbf{X}_{j+1}^f - \mathbf{X}_s^f\right). \tag{24}$$

Again, analogous summing conventions as in (17)–(18) are used. The above expression (24) can be further recast into a vertex based quadrature rule over f as follows

$$\int_f \mathbf{v} \otimes \mathbf{n}^f \mathrm{d}S = \sum_{j=1}^{m^f} \left\{ \left[\frac{\beta_j^f}{3}|f| + \frac{1}{3}\left(|T_j^f| + |T_{j-1}^f|\right) \right] \mathbf{v}\left(\mathbf{X}_j^f\right) \right\} \otimes \mathbf{n}^f = \sum_{j=1}^{m^f} w_j^f \mathbf{v}\left(\mathbf{X}_j^f\right) \otimes \mathbf{n}^f \tag{25}$$

by assigning each vertex $\mathbf{X}_j^f$ with a weight w_j^f of the form $w_j^f \doteq \frac{\beta_j^f}{3}|f| + \frac{1}{3}\left(|T_j^f| + |T_{j-1}^f|\right)$, where $|f|$ is the (absolute) area of f. Several remarks are worthwhile making on the above vertex based quadrature rule. First, notice that with the assumption that each f is star-convex with respect to $\mathbf{X}_s^f$, the weight w_j^f associated with each vertex is guaranteed to be strictly positive. On the other hand, for cases where f is not star-convex with respect to $\mathbf{X}_s^f$ (including $\mathbf{X}_s^f$ lies outside of f), the weights w_j^f may take negative values. However, we observe that the resulting vertex based quadrature rule on f still enjoy first order accuracy, as will be discussed in detail in Appendix B. Note that, in such non star-convex case, definition (21) makes no sense anymore; but (thanks to the above observations) it turns out that one can still implement the above formulas and obtain a convergent scheme.

As a result, the volume average of $\nabla \mathbf{v}$ takes the final form

$$\frac{1}{|E|}\int_E \nabla \mathbf{v} \mathrm{d}\mathbf{X} = \frac{1}{|E|}\sum_{f\in\partial E}\sum_{j=1}^{m^f}\left\{ w_j^f \mathbf{v}\left(\mathbf{X}_j^f\right) \otimes \mathbf{n}_f \right\}. \tag{26}$$

Observe that, as in the 2D case, the above expression only makes use of the DOFs of $\mathbf{v}$ and the geometric information of E.

In the proposed VEM approximation, we make use of two projection operators [35]. The first projection operator, denoted as Π_E^0, is a tensor-valued $\mathcal{L}^2$ projection operator which projects any given second order tensor $\mathbf{G} \in [\mathcal{L}^2(E)]^{d\times d}$ onto its average value over E, that is,

$$\Pi_E^0 \mathbf{G} = \frac{1}{|E|}\int_E \mathbf{G} \mathrm{d}\mathbf{X}. \tag{27}$$

We remark that for any given element $E \in \Omega_h$ and $\mathbf{v} \in \mathcal{V}(E)$, the projection $\Pi_E^0(\nabla \mathbf{v})$ is explicitly computable in both 2D and 3D using the DOFs of $\mathbf{v}$ and geometric information of E, which is a direct consequence of (18) and (26).

On the other hand, the second projection operator, denoted as Π_E^∇, is a vector-valued projection operator, which projects from the VEM space $\mathcal{V}(E)$ onto $[\mathcal{P}_1(E)]^d$. It is defined such that

$$\begin{cases} \nabla\left(\Pi_E^\nabla \mathbf{v}\right) = \Pi_E^0\left(\nabla \mathbf{v}\right) \\ \sum_{i=1}^m (\Pi_E^\nabla \mathbf{v})\left(\mathbf{X}_i\right) = \sum_{i=1}^m \mathbf{v}\left(\mathbf{X}_i\right). \end{cases} \tag{28}$$

As we can see, for any given $\mathbf{v} \in \mathcal{V}(E)$, $\Pi_E^\nabla \mathbf{v}$ becomes a linear function. The first condition in the above definition ensures that the gradient of the linear function equals the average gradient of $\mathbf{v}$ over E and the second condition determines the constant component of the linear function by ensuring that the average value of $\Pi_E^\nabla \mathbf{v}$ at vertices is equal to the average value of $\mathbf{v}$ at vertices. With the two aforementioned conditions, the linear function $\Pi_E^\nabla \mathbf{v}$ is uniquely determined and depends only on the DOFs of $\mathcal{V}(E)$ and on geometric information of E.

We close this section with an important observation. Our choice (21) for the definition of $\mathcal{V}(E)$ on faces is different from those proposed in [43,30,35]. The reason is that, differently from the aforementioned papers, the definition of space in (21) guarantees that the faces of the deformed element are piecewise planar. Our choice is therefore more suitable for large deformation problems and the associated computations.

4.2. Area/volume average of J on general polygonal and polyhedral elements[1]

For a given displacement field $\mathbf{v} \in \mathcal{V}(E)$, let us denote $\widetilde{E}$ as the deformed configuration of element E and $\widetilde{\mathbf{X}}_i$ (where $\widetilde{\mathbf{X}}_i = \{\widetilde{X}_i, \widetilde{Y}_i\}^T$ in 2D or $\widetilde{\mathbf{X}}_i = \{\widetilde{X}_i, \widetilde{Y}_i, \widetilde{Z}_i\}^T$ in 3D) as the position vector of vertex i of $\widetilde{E}$ such that $\widetilde{\mathbf{X}}_i = \mathbf{X}_i + \mathbf{v}(\mathbf{X}_i)$, as shown in Fig. 2(a) and (b). Similarly, we also utilize $\widetilde{e}$, $\widetilde{f}$ and $\widetilde{\mathcal{F}}^i$ to denote the deformed edge, deformed face and the set of deformed faces that are connected to vertex i, respectively. The deformation does not change neither the vertex-face connectivity nor the relation between the global and local numbering of the vertices of element E. In other words, if a given $f \in \mathcal{F}_i$ in the undeformed configuration, we have $\widetilde{f} \in \widetilde{\mathcal{F}}_i$. Additionally, if the ith vertex of E is renumbered as jth vertex on face f in the undeformed configuration, the relations $\widetilde{\mathbf{X}}_j^f = \widetilde{\mathbf{X}}_{\mathcal{G}_f(i)}^f$ and $\widetilde{\mathbf{X}}_i = \widetilde{\mathbf{X}}_{\mathcal{G}_{\widetilde{f}}^{-1}(j)}$ still hold in the deformed configuration.

The area/volume average of J over E under $\mathbf{v}$, denoted as J_E henceforth, is defined as

$$J_E\left(\mathbf{v}\right) = \frac{1}{|E|}\int_E J\left(\mathbf{v}\right) \mathrm{d}\mathbf{X}. \tag{29}$$

Pushing the integral forward into the deformed configuration and applying the divergence theorem, we end up with the following expression

$$J_E\left(\mathbf{v}\right) = \frac{1}{|E|}\int_{\widetilde{E}} \mathrm{d}\widetilde{\mathbf{X}} = \frac{1}{d|E|}\int_{\widetilde{E}} \widetilde{\nabla}\cdot\widetilde{\mathbf{X}} \mathrm{d}\widetilde{\mathbf{X}} = \frac{1}{d|E|}\int_{\partial\widetilde{E}} \widetilde{\mathbf{X}}\cdot\widetilde{\mathbf{n}} \mathrm{d}\widetilde{S}, \tag{30}$$

where $\widetilde{\nabla}$ stands for the gradient operator with respect to the deformed configuration and $\widetilde{\mathbf{n}}$ is the unit normal vector in the deformed configuration.

[1] For later use, this subsection demonstrates that, based on the definitions of $\mathcal{V}(E)$, the volume average of $J = \det \mathbf{F}$ over E, as well as its first and second variations, can be computed exactly for any given displacement field $\mathbf{v} \in \mathcal{V}(E)$ both in 2D and 3D.

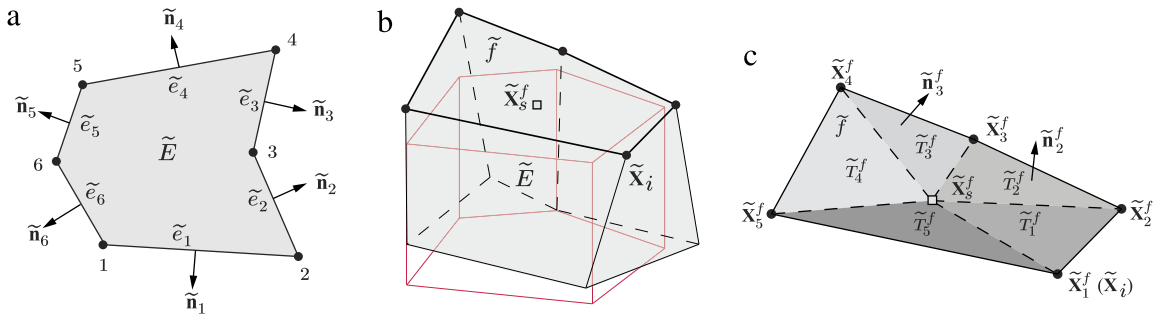

Fig. 2. Illustration of (a) a 2D polygonal element $\widetilde{E}$ in its deformed configuration, (b) a 3D polyhedral element $\widetilde{E}$ in its deformed configuration, and (c) a generic face $\widetilde{f}$ (not necessarily planar) of the polyhedral element $\widetilde{E}$.

Computing J_E in the 2D case. In the 2D case, because any displacement field $\mathbf{v} = \{v_x, v_y\}^T \in \mathcal{V}(E)$ varies linearly on each edge e, then $\widetilde{e}$ remains straight in the deformed configuration, as shown in Fig. 2(a). Thus, we can expand (30) as

$$J_E(\mathbf{v}) = \frac{1}{2|E|}\int_{\partial\widetilde{E}} \widetilde{\mathbf{X}}\cdot\widetilde{\mathbf{n}}\mathrm{d}\widetilde{S} = \frac{1}{4|E|}\sum_{i=1}^{m}\widetilde{\mathbf{X}}_i\cdot\left(|\widetilde{e}_i|\widetilde{\mathbf{n}}_i + |\widetilde{e}_{i-1}|\widetilde{\mathbf{n}}_{i-1}\right), \tag{31}$$

where $|\widetilde{e}_i|$ and $\widetilde{\mathbf{n}}_i$ denote the length and outward unit normal vector of the ith deformed edge $\widetilde{e}_i$.

By introducing a matrix $\mathbf{R} \in \mathbb{R}^{2\times 2}$ representing a 90° degree counterclockwise rotation, which is of the form

$$\mathbf{R} = \begin{bmatrix} 0 & -1 \\ 1 & 0 \end{bmatrix} \tag{32}$$

and satisfies $|\widetilde{e}_i|\widetilde{\mathbf{n}}_i = \mathbf{R}(\widetilde{\mathbf{X}}_i - \widetilde{\mathbf{X}}_{i+1})$, we simplify the above relation as

$$J_E(\mathbf{v}) = \frac{1}{4|E|}\sum_{i=1}^{m}\widetilde{\mathbf{X}}_i\cdot\mathbf{R}\left(\widetilde{\mathbf{X}}_{i-1} - \widetilde{\mathbf{X}}_{i+1}\right). \tag{33}$$

By direct derivation of (33), the first variation of J_E with respect to $\delta\mathbf{v} = \{\delta v_x, \delta v_y\} \in \mathcal{V}(E)$ can be obtained as

$$DJ_E(\mathbf{v})\cdot\delta\mathbf{v} = \frac{1}{2|E|}\sum_{i=1}^{m}\delta\mathbf{v}(\mathbf{X}_i)\cdot\mathbf{R}\left(\widetilde{\mathbf{X}}_{i-1} - \widetilde{\mathbf{X}}_{i+1}\right). \tag{34}$$

For practical computations, it is convenient to recast the above expressions into matrix representation. By introducing $\mathbf{H} \in \mathbb{R}^{2m\times 2m}$ of the form

$$\mathbf{H} = \begin{bmatrix} \mathbf{0} & -\mathbf{R} & \mathbf{0} & \cdots & \mathbf{0} & \mathbf{R} \\ \mathbf{R} & \mathbf{0} & -\mathbf{R} & \cdots & \mathbf{0} & \mathbf{0} \\ & & \vdots & & & \\ -\mathbf{R} & \mathbf{0} & \mathbf{0} & \cdots & \mathbf{R} & \mathbf{0} \end{bmatrix}, \tag{35}$$

which is a symmetric matrix (since $\mathbf{R}$ is skew-symmetric), we can rewrite Eqs. (33) and (34) as

$$J_E(\mathbf{v}) = \frac{1}{4|E|}\widetilde{\mathbf{N}}^T\mathbf{H}\widetilde{\mathbf{N}} \quad\text{and}\quad DJ_E(\mathbf{v})\cdot\delta\mathbf{v} = \frac{1}{2|E|}\delta\mathbf{V}^T\mathbf{H}\widetilde{\mathbf{N}}, \tag{36}$$

where $\widetilde{\mathbf{N}}$ and $\delta\mathbf{V} \in \mathbb{R}^{2m}$ are given by

$$\widetilde{\mathbf{N}} = \begin{Bmatrix} \widetilde{X}_1 & \widetilde{Y}_1 & \cdots & \widetilde{X}_m & \widetilde{Y}_m \end{Bmatrix}^T \text{ and } \delta\mathbf{V} = \begin{Bmatrix} \delta v_x(\mathbf{X}_1) & \delta v_y(\mathbf{X}_1) & \cdots & \delta v_x(\mathbf{X}_m) & \delta v_y(\mathbf{X}_m) \end{Bmatrix}^T, \tag{37}$$

respectively.

The second variation of J_E can be obtained directly in matrix representation by a plain derivation of (36). From the relation between $\widetilde{\mathbf{N}}$ and $\mathbf{v}$, we obtain the following result

$$D\left(DJ_E(\mathbf{v})\cdot\delta\mathbf{v}\right)\cdot\mathbf{w}=\frac{1}{|E|}\int_E\left(\nabla(\delta\mathbf{v}):\frac{\partial^2 J}{\partial\mathbf{F}\partial\mathbf{F}}(\mathbf{v})\right):\nabla\mathbf{w}\mathrm{d}\mathbf{X}=\frac{1}{2|E|}\delta\mathbf{V}^T\mathbf{H}\mathbf{W}, \tag{38}$$

where $\mathbf{w}=\{w_x,w_y\}^T\in\mathcal{V}(E)$ is the incremental displacement field and $\mathbf{W}\in\mathbb{R}^{2m}$ is a vector of the form

$$\mathbf{W}=\left\{w_x\left(\mathbf{X}_1\right)\quad w_y\left(\mathbf{X}_1\right)\quad\cdots\quad w_x\left(\mathbf{X}_m\right)\quad w_y\left(\mathbf{X}_m\right)\right\}^T. \tag{39}$$

Computing J_E in the 3D case. The calculation of J_E in the 3D case is more complicated because the planar face f typically deforms into a non-planar $\widetilde{f}$ in its deformed configuration, as shown in Fig. 2(c). As a result, the associated deformed normal vector $\widetilde{\mathbf{n}}_f$ becomes non-constant over $\widetilde{f}$. Yet, each deformed triangulated subface $\widetilde{T}_i^f$ of the T_i^f still remains planar. If we denote the deformed normal of $\widetilde{T}_i^f$ as $\widetilde{\mathbf{n}}_i^f$ and employ a vertex-based integration rule, we have

$$\begin{aligned}J_E\left(\mathbf{v}\right)&=\frac{1}{3|E|}\int_{\partial\widetilde{E}}\widetilde{\mathbf{X}}\cdot\widetilde{\mathbf{n}}\mathrm{d}\widetilde{S}=\frac{1}{3|E|}\sum_{\widetilde{f}\in\partial\widetilde{E}}\sum_{j=1}^{m^f}\left[|\widetilde{T}_j^f|\,\widetilde{\mathbf{n}}_j^f\cdot\frac{1}{3}\left(\widetilde{\mathbf{X}}_j^f+\widetilde{\mathbf{X}}_{j+1}^f+\widetilde{\mathbf{X}}_s^f\right)\right]\\&=\frac{1}{3|E|}\sum_{\widetilde{f}\in\partial\widetilde{E}}\sum_{j=1}^{m^f}\left\{\frac{1}{6}\left(\widetilde{\mathbf{X}}_j^f+\widetilde{\mathbf{X}}_{j+1}^f+\widetilde{\mathbf{X}}_s^f\right)\cdot\left(\widetilde{\mathbf{X}}_j^f-\widetilde{\mathbf{X}}_s^f\right)\wedge\left(\widetilde{\mathbf{X}}_{j+1}^f-\widetilde{\mathbf{X}}_s^f\right)\right\}.\end{aligned} \tag{40}$$

Further simplification of the above equation yields, after some calculations,

$$J_E\left(\mathbf{v}\right)=\frac{1}{6|E|}\sum_{\widetilde{f}\in\partial\widetilde{E}}\sum_{j=1}^{m^f}\left\{\widetilde{\mathbf{X}}_s^f\cdot\widetilde{\mathbf{X}}_j^f\wedge\widetilde{\mathbf{X}}_{j+1}^f\right\}. \tag{41}$$

Notice that, since J_E is an algebraic function of the DOFs of $\mathbf{v}$, then its first variation with respect to any given $\delta\mathbf{v}\in\mathcal{V}(E)$ is obtained as

$$DJ_E\left(\mathbf{v}\right)\cdot\delta\mathbf{v}=\frac{1}{6|E|}\sum_{i=1}^{m}\left\{\delta\mathbf{v}\left(\mathbf{X}_i\right)\cdot\left[\sum_{\widetilde{f}\in\widetilde{\mathcal{F}}^i}\left(\beta_i^f\sum_{j=1}^{m_f}\widetilde{\mathbf{X}}_{j-1}^f\wedge\widetilde{\mathbf{X}}_j^f+\widetilde{\mathbf{X}}_s^f\wedge\left(\widetilde{\mathbf{X}}_{\mathcal{G}_f(i)-1}^f-\widetilde{\mathbf{X}}_{\mathcal{G}_f(i)+1}^f\right)\right)\right]\right\}. \tag{42}$$

Following the same procedure above, the second variation of J_E is given by

$$D\left(DJ_E(\mathbf{v})\cdot\delta\mathbf{v}\right)\cdot\mathbf{w}=\sum_{i=1}^{m}\sum_{j=1}^{m}\delta\mathbf{v}\left(\mathbf{X}_i\right)\cdot\frac{\partial^2 J_E}{\partial\widetilde{\mathbf{X}}_i\partial\widetilde{\mathbf{X}}_j}(\mathbf{v})\cdot\mathbf{w}\left(\mathbf{X}_j\right), \tag{43}$$

where the 3×3 matrices $\partial^2 J_E/\partial\widetilde{\mathbf{X}}_i\partial\widetilde{\mathbf{X}}_j$ can be expressed in the form

$$\begin{aligned}\frac{\partial^2 J_E}{\partial\widetilde{\mathbf{X}}_i\partial\widetilde{\mathbf{X}}_j}(\mathbf{v})=\frac{1}{6|E|}\sum_{\widetilde{f}\in\widetilde{\mathcal{F}}_{ij}}&\left\{\beta_i^f[\widetilde{\mathbf{X}}_{\mathcal{G}_f(j)-1}^f-\widetilde{\mathbf{X}}_{\mathcal{G}_f(j)+1}^f]_\wedge+\beta_j^f[\widetilde{\mathbf{X}}_{\mathcal{G}_f(i)+1}^f-\widetilde{\mathbf{X}}_{\mathcal{G}_f(i)-1}^f]_\wedge\right.\\&\left.+\left(\delta_{\mathcal{G}(j),\mathcal{G}_f(i)-1}-\delta_{\mathcal{G}(j),\mathcal{G}_f(i)+1}\right)\left[\widetilde{\mathbf{X}}_s^f\right]_\wedge\right\}\end{aligned} \tag{44}$$

and $\widetilde{\mathcal{F}}_{ij}$ denotes the set of faces that are connected to both the ith and the jth vertices (with global numbering) of E. In the above expression, $\delta_{i,j}$ denotes the Kronecker delta function and we have made use of the notation

$$[\mathbf{a}]_\wedge=\begin{bmatrix}0&-a_z&a_y\\a_z&0&a_x\\-a_y&-a_x&0\end{bmatrix} \tag{45}$$

for a given vector $\mathbf{a}=\{a_x,a_y,a_z\}^T$.

Table 1
Approaches for computing area or volume average of $J = \det \mathbf{F}$ over element E.

Approaches	Associated equations
Robust	(36), (38), (41), (42), (43)
Simple	(46), (47), (48)

We remark that in both 2D and 3D cases, J_E and its first and second variations are all algebraic functions that can be exactly computed using only the coordinates of the vertices in the deformed configuration and the DOFs of fields $\delta\mathbf{v}$ and $\mathbf{w}$.

We also remark that another option of approximating J_E is to simply use the projected gradient. For any given $\delta\mathbf{v}$, $\mathbf{w} \in \mathcal{V}(E)$, we obtain

$$J_E(\mathbf{v}) = \det\left(\mathbf{I} + \Pi_E^0(\nabla\mathbf{v})\right), \tag{46}$$

$$DJ_E(\mathbf{v}) \cdot \delta\mathbf{v} = \frac{\partial J}{\partial \mathbf{F}}\left(\mathbf{I} + \Pi_E^0(\nabla\mathbf{v})\right) : \Pi_E^0(\nabla(\delta\mathbf{v})), \tag{47}$$

$$D\left(DJ_E(\mathbf{v}) \cdot \delta\mathbf{v}\right) \cdot \mathbf{w} = \Pi_E^0(\nabla(\delta\mathbf{v})) : \frac{\partial^2 J}{\partial \mathbf{F}\partial \mathbf{F}}\left(\mathbf{I} + \Pi_E^0(\nabla\mathbf{v})\right) : \Pi_E^0(\nabla\mathbf{w}). \tag{48}$$

As compared to the previous formula of J_E derived in this subsection, the above approximations take simpler forms and are easier for computational implementations, especially in the 3D case. Moreover, we observe that the approximated J_E becomes exact for any $\mathbf{v} \in [\mathcal{P}_1(E)]^d$, meaning that the approximation (46) is also first-order consistent. Therefore, as demonstrated by numerical examples, the above approximations in the VEM construction can also lead to optimally convergent results. However, we remark that (46) is less robust than (29) in the sense that, when the level of deformation increases and the shape of the element becomes more irregular, this approach is more prone to experience non-convergence in the Newton–Raphson algorithm and may provide less accurate solutions. We will present both approaches of computing J_E and their variations in the numerical examples of this paper. For convenience, we refer to the VEM following (29), i.e. using expressions (36), (38) and (41)–(43), as to the "Robust" approach and to the VEM using (46)–(48) as to the "Simple" approach. This is illustrated by Table 1.

4.3. Pressure VEM spaces

For the two-field mixed virtual elements used in this paper, we assume a piecewise constant approximation of the pressure field, which takes constant value over each element E. This approximation has been shown to lead to numerically stable solutions on several polygonal meshes in 2D, such as the Centroidal Voronoi Tessellation (CVT) and structured hexagonal meshes [44,9,12]. Accordingly, the finite dimensional pressure space $\mathcal{Q}_h$ is then identified with the following definition:

$$\mathcal{Q}_h \doteq \{\widehat{q}_h \in \mathcal{Q} : \widehat{q}|_E = \text{constant}\ \forall E \in \Omega_h\}. \tag{49}$$

5. Variational approximations

Having defined the displacement and pressure VEM spaces, we proceed to propose the displacement-based and two-field mixed VEM approximations on the polygonal/polyhedral mesh Ω_h. In particular, we first introduce the two field-mixed Galerkin approximation assuming the piecewise constant pressure field and exact integration, as well as an equivalent displacement-based Galerkin approximation, which also assumes exact integration. Subsequently, decomposition of the exact integral into consistency and stability components is introduced for both approximations, which leads to the final form of the displacement-based and mixed VEM approximations. Moreover, we discuss different constructions of stability and loading terms and propose a new stabilization scheme for isotropic solids. Finally, the polynomial consistency of the VEM approximations is demonstrated.

5.1. Two-field mixed and equivalent displacement-based Galerkin approximations with exact integration

For lower-order mixed elements, whose pressure field $\widehat{q}_h$ is assumed to be constant over each element, the Galerkin approximation consists of finding the equilibrating displacement $\mathbf{u}_h$ and pressure $\widehat{p}_h$, such that

$$\widehat{\Pi}_h\left(\mathbf{u}_h, \widehat{p}_h\right) = \min_{\mathbf{v}_h \in \mathcal{K}_h} \max_{\widehat{q}_h \in \mathcal{Q}_h} \widehat{\Pi}\left(\mathbf{v}_h, \widehat{q}_h\right), \tag{50}$$

where

$$\widehat{\Pi}_h\left(\mathbf{v}_h, \widehat{q}_h\right) = \sum_E \int_E \left\{ \Psi(\mathbf{F}\left(\mathbf{v}_h\right)) + \widehat{q}_h\left[J\left(\mathbf{v}_h\right) - 1\right] - \widehat{U}^*\left(\widehat{q}_h\right) \right\} \mathrm{d}\mathbf{X} - \sum_E \int_E \mathbf{f} \cdot \mathbf{v}_h \mathrm{d}\mathbf{X} - \int_{\Gamma_h^{\mathbf{t}}} \mathbf{t} \cdot \mathbf{v}_h \mathrm{d}S. \tag{51}$$

For the time being, we assume exact integration over E in our Galerkin approximations. Since $\widehat{q}_h$ takes constant values over E the above formulation can be rewritten as

$$\begin{aligned} \widehat{\Pi}_h\left(\mathbf{v}_h, \widehat{q}_h\right) = & \sum_E \int_E \Psi(\mathbf{F}\left(\mathbf{v}_h\right)) \mathrm{d}\mathbf{X} + \sum_E \left\{ |E| \left[\widehat{q}_h|_E \Big(J_E\left(\mathbf{v}_h\right) - 1 \Big) - \widehat{U}^*\left(\widehat{q}_h|_E\right) \right] \right\} \\ & - \sum_E \int_E \mathbf{f} \cdot \mathbf{v}_h \mathrm{d}\mathbf{X} - \int_{\Gamma_h^{\mathbf{t}}} \mathbf{t} \cdot \mathbf{v}_h \mathrm{d}S. \end{aligned} \tag{52}$$

Observe that J_E appears in the second term on the right hand side of the above expression, which can be evaluated either exactly (29) or approximately (46) using the formulas provided in the preceding section.

We also introduce a displacement-based Galerkin approximation that consists of seeking the unknown displacement field such that

$$\Pi_h\left(\mathbf{u}_h\right) = \min_{\mathbf{v}_h \in \mathcal{K}_h} \Pi_h\left(\mathbf{v}_h\right), \tag{53}$$

where

$$\Pi_h\left(\mathbf{v}_h\right) = \sum_E \int_E \Psi(\mathbf{F}\left(\mathbf{v}_h\right)) \mathrm{d}\mathbf{X} + \sum_E |E| \, U\left(J_E(\mathbf{v}_h)\right) - \sum_E \int_E \mathbf{f} \cdot \mathbf{v}_h \mathrm{d}\mathbf{X} - \int_{\Gamma_h^{\mathbf{t}}} \mathbf{t} \cdot \mathbf{v}_h \mathrm{d}S. \tag{54}$$

By realizing that

$$\sum_E |E| U\left(J_E(\mathbf{v}_h)\right) = \max_{\widehat{q}_h \in \mathcal{Q}_h} \left\{ \sum_E |E| \left[\widehat{q}_h|_E \left(J_E(\mathbf{v}_h) - 1 \right) - \widehat{U}^*\left(\widehat{q}_h|_E\right) \right] \right\} \tag{55}$$

as a consequence of (8), we note that the displacement-based approximation is equivalent to the two-field mixed one except for the case of purely incompressible materials, where the displacement approximation fails because of (2). In the finite element method (FEM) literature, this equivalence is also explored in [45]. Moreover, since $\mathrm{d}^2U/(dJ)^2 \to +\infty$ as the material approaches incompressibility, employing the above displacement-based approximation for nearly incompressible materials will lead to finite element systems with high condition numbers in the stiffness matrices, possibly resulting in poor convergence performance of the Newton–Raphson method. By contrast, the two-field mixed approximation is free of the above shortcomings and is valid for materials with any level of incompressibility, including those that are purely incompressible.

This work also considers the standard displacement-based and two-field mixed FEM approximations on polygonal meshes [12]. The Mean Value coordinates are used to construct the displacement spaces [46] and the gradient correction scheme [23] is also adopted to ensure the polynomial consistency of the finite element approximations.

5.2. Displacement-based and two-field mixed VEM approximations

This subsection proceeds to propose the displacement-based and two-field mixed VEM approximations. Following the original idea of the VEM, we decompose the exact integrals associated with Ψ in (52) and (54) into "consistency" and "stability" terms [25].

The displacement-based VEM approximation then consists of seeking the unknown displacement field $\mathbf{u}_h$ such that it satisfies Eq. (53) with

$$\Pi_h^{VEM}(\mathbf{v}_h) = \sum_E |E|\,\Psi\left(\mathbf{I} + \Pi_E^0 \nabla \mathbf{v}_h\right) + \frac{1}{2}\sum_E \alpha_E(\mathbf{s}_h)\, S_{h,E}\left(\mathbf{v}_h - \Pi_E^\nabla \mathbf{v}_h, \mathbf{v}_h - \Pi_E^\nabla \mathbf{v}_h\right) + \sum_E |E|\, U\left(J_E(\mathbf{v}_h)\right) - \langle \mathbf{f}, \mathbf{v}_h\rangle_h - \langle \mathbf{t}, \mathbf{v}_h\rangle_h. \tag{56}$$

In the above expression, $\langle \mathbf{f}, \mathbf{v}_h\rangle_h$ and $\langle \mathbf{t}, \mathbf{v}_h\rangle_h$ stand for the approximated loading terms associated with body force and surface traction respectively, whose forms will be discussed in the next subsection. Moreover, notice that the first term on the right hand side of (56) is first-order consistent, and is thus called the "consistency" term, meaning that if $\mathbf{v}_h$ is a first order polynomial function, this term recovers the first term in (54). However, unless E is a linear triangular/tetrahedral element, the consistency term contains non-physical kernel that may lead to spurious modes in the displacement solution. A stabilization term (the second term on the right hand size of (56)) is thus needed to penalize those non-physical kernels. The stabilization term is made up of two components, $\alpha_E(\mathbf{s}_h)$ and $S_{h,E}(\mathbf{v}_h - \Pi_E^\nabla \mathbf{v}_h, \mathbf{v}_h - \Pi_E^\nabla \mathbf{v}_h)$. In fact, $S_{h,E}(\cdot,\cdot)$ is a bilinear form given by [35]

$$S_{h,E}(\mathbf{v}_h, \mathbf{w}_h) = h_E^{d-2} \sum_{v\in E} \mathbf{v}_h(\mathbf{X}_v)\cdot \mathbf{w}_h(\mathbf{X}_v) \quad \forall \mathbf{v}_h, \mathbf{w}_h \in \mathcal{K}_h \quad \forall E \in \Omega_h \tag{57}$$

with $h_E = |E|^{1/d}$ measuring the size of E, whereas $\alpha_E(\mathbf{s}_h)$ is a scalar valued function of $\mathbf{s}_h \in \mathcal{K}_h$, a detailed discussion of which will be provided in the next subsection.

In the same manner, we also state the final form of the two-field mixed VEM approximation, which consists of finding the unknown displacement field $\mathbf{u}_h$ and pressure field $\widehat{p}_h$ such that it satisfies Eq. (50) with

$$\widehat{\Pi}_h^{VEM}(\mathbf{v}_h, \widehat{q}_h) = \sum_E |E|\,\Psi\left(\mathbf{I} + \Pi_E^0 \nabla \mathbf{v}_h\right) + \frac{1}{2}\sum_E \alpha_E(\mathbf{s}_h)\, S_{h,E}\left(\mathbf{v}_h - \Pi_E^\nabla \mathbf{v}_h, \mathbf{v}_h - \Pi_E^\nabla \mathbf{v}_h\right) + \sum_E |E|\left[\widehat{q}_h|_E\left(J_E(\mathbf{v}_h) - 1\right) - \widehat{U}^*\left(\widehat{q}_h|_E\right)\right] - \langle \mathbf{f}, \mathbf{v}_h\rangle_h - \langle \mathbf{t}, \mathbf{v}_h\rangle_h. \tag{58}$$

While the focus of this paper is on developing lower order VEM approximations, a few remarks are worthwhile making on their possible extension to the higher-order VEM approximations. For higher order VEM approximations, the local VEM spaces are well-defined and the associated projections are computable [43]. A possible extension using the "Simple" approach can follow the same methodology presented in this section: one can decompose the stored energy function into a consistency part which utilizes higher-order projections and then stabilize the remaining part. On the other hand, the extension to higher order VEM considering the "Robust" approach is a more challenging part, which deserves further theoretical developments.

5.3. Discussion on the stabilization parameter $\alpha_E(\mathbf{s}_h)$

In the sequel, we review and discuss the stabilization parameter α_E proposed in [35] for small deformation nonlinear elastic and inelastic problems. Motivated by the discussions, we hereby propose a new expression for the stabilization parameter α_E, which is based on the trace of the Hessian of Ψ.

Norm-based stabilization. In the work by Beirão da Veiga et al. [35], the stabilization parameter α_E is given by the following expression:

$$\alpha_E(\mathbf{s}_h) = \left\| \frac{\partial^2 \Psi}{\partial \mathbf{F}\partial \mathbf{F}}\left(\mathbf{I} + \Pi_E^0 \nabla \mathbf{s}_h\right)\right\|, \quad \forall \mathbf{s}_h \in \mathcal{K}_h \tag{59}$$

where $\|\!|\cdot|\!\|$ denotes any norm of a fourth order tensor. In the remainder of the paper, we refer this choice as the norm-based stabilization. As a common choice, the norm induced by the Euclidean vector norm is considered in this work. In this case, the stabilization parameter α_E equals the absolute value of the largest eigenvalue of the Hessian of Ψ. Intuitively, this amounts to assigning the moduli of a material in its stiffest direction to all its directions. As a result, as will be shown in the filled elastomer example, the VEM approximations adopting this stabilization parameter

typically yield over stiff responses in large deformation analysis. Notice that in this norm-based stabilization, unlike the original form of α_E used in [35], which essentially uses the Hessian of the entire stored-energy function W, we only use that of the first component of the stored-energy function Ψ (similar to the selective integration concept in the FEM literature).

The choice of $\mathbf{s}_h \in \mathcal{K}_h$ can be any kinematically admissible displacement. Two choices of $\mathbf{s}_h$ are discussed in [35], which are $\mathbf{s}_h = \mathbf{0}$ and $\mathbf{s}_h = \mathbf{u}_h^{n-1}$, where $\mathbf{u}_h^{n-1}$ is the equilibrium displacement field obtained in the last Newton–Raphson step. The former choice amounts to evaluating α_E in the undeformed configuration. For this choice, α_E is a constant scalar that is independent of the deformation state and, as shown in [35], can easily lead to unsatisfactory results also in small deformation regimes. By contrast, the latter choice evaluates α_E in the last deformed configuration that is solved by the Newton–Raphson method, implying that α_E keeps updating according to the deformation states. The motivation for the choice $\mathbf{s}_h = \mathbf{u}_h^{n-1}$ in [35] (instead of the more natural $\mathbf{s}_h = \mathbf{u}_h$ with $\mathbf{u}_h$ the displacement field that we are seeking for) is to simplify the Newton–Raphson iterations by avoiding to compute the derivatives of α_E in the associated tangent matrix. On the other hand, when applied to finite elasticity problems, especially to those involving heterogeneous and large localized deformations, also this second choice has its own shortcomings. As will be demonstrated by the filled elastomer example in Section 6, the choice of $\mathbf{s}_h = \mathbf{0}$ in α_E tends to under stabilize some elements at high deformation levels (which leads to noticeable hourglass-type deformations in those elements), while choosing $\mathbf{s}_h = \mathbf{u}_h^{n-1}$ renders the approximations dependent on the loading histories, possibly making it unsuited for problems involving very large and heterogeneous deformation fields. It is worthwhile noting that, although $\mathbf{s}_h = \mathbf{u}_h$ is a more intuitive choice, it is also more computationally demanding than $\mathbf{s}_h = \mathbf{u}_h^{n-1}$ for the reason mentioned above.

Trace-based stabilization. The expression (59) was introduced in [35] in order to obtain a (strictly) positive stabilization factor, that is a reasonable condition for small deformation regimes. On the other hand, this may become an unreliable choice in large deformation analysis, where issues related to the physical stability of the material appear. Motivated by the above discussion, we propose a new stabilization parameter α_E which is based on the trace of the Hessian of Ψ given by

$$\alpha_E(\mathbf{s}_h) = \frac{1}{d^2}\mathrm{tr}\left(\frac{\partial^2 \Psi}{\partial \mathbf{F}\partial \mathbf{F}}\left(\mathbf{I} + \Pi_E^0 \nabla \mathbf{s}_h\right)\right), \quad \forall \mathbf{s}_h \in \mathcal{K}_h, \tag{60}$$

where d is the dimension ($d = 2, 3$). We refer to it as the trace-based stabilization. Instead of taking into account only the largest eigenvalue of the Hessian of Ψ as in the norm-based stabilization using the Euclidean induced norm, α_E in the trace-based stabilization takes into account all the eigenvalues of the Hessian of Ψ (α_E equals the algebraic average of all the eigenvalues of the Hessian of Ψ). In addition, whereas the norm-based stabilization is always positive, the trace-based stabilization may take negative values, for instance, when the eigenvalues of the Hessian are dominantly negative. This issue is closely related to the physical stability of the material, a detailed analysis of which is beyond the scope of this paper and is subjected to future work [47].

When specialized to isotropic materials, explicit expressions can be obtained for α_E in the trace-based stabilization. For isotropic material, $\Psi(\mathbf{F})$ is a function $\Phi(I_1, I_2, J)$ which solely depends on the three invariants I_1, I_2 and J of the right Cauchy deformation tensor $\mathbf{C} = \mathbf{F}^T\mathbf{F}$, where $I_1 = \mathrm{tr}\mathbf{C}$ and $I_2 = 1/2[(\mathrm{tr}\mathbf{C})^2 - \mathrm{tr}(\mathbf{C}^2)]$. Under this condition, the proposed stabilization parameter α_E is given by:

$$\alpha_E(\mathbf{s}_h) = \frac{1}{d^2}\mathrm{tr}\left[\frac{\partial^2 \Phi}{\partial \mathbf{F}\partial \mathbf{F}}\left(I_1\left(\mathbf{I} + \Pi_E^0 \nabla \mathbf{s}_h\right), I_2\left(\mathbf{I} + \Pi_E^0 \nabla \mathbf{s}_h\right), J\left(\mathbf{I} + \Pi_E^0 \nabla \mathbf{s}_h\right)\right)\right]. \tag{61}$$

As will be shown in detail in Appendix A, making use of the Cayley–Hamilton theorem, the above expression can be further simplified as

Table 2
Summary of stabilization schemes and choices of $\mathbf{s}_h$. A symbol "×" means that such choice has not been tested numerically—the reason can be found in the corresponding footnote.

	$\mathbf{s}_h = \mathbf{0}$	$\mathbf{s}_h = \mathbf{u}_h^{n-1}$	$\mathbf{s}_h = \mathbf{u}_h$
Norm-based stabilization	✓	✓	×[a]
Trace-based stabilization	×[b]	✓	✓

[a] This choice in the norm-based stabilization is significantly more computationally demanding than other choices and is therefore not considered in this paper.
[b] Although this choice can be easily considered, we prefer to disregard it because it shares the same drawback as choosing $\mathbf{s}_h = \mathbf{0}$ in the norm-based stabilization.

$$\alpha_E(\mathbf{s}_h) = \frac{1}{4}\left[4I_1\frac{\partial^2\Phi}{\partial I_1\partial I_1} + \left(8I_1\,I_2 - 4J^2\,I_1\right)\frac{\partial^2\Phi}{\partial I_2\partial I_2} + I_1\frac{\partial^2\Phi}{\partial J\partial J} + 16I_2\frac{\partial^2\Phi}{\partial I_1\partial I_2} + 8J\frac{\partial^2\Phi}{\partial I_1\partial J} + 2J\,I_1\frac{\partial^2\Phi}{\partial I_2\partial J} + 8\frac{\partial\Phi}{\partial I_1} + 2I_1\frac{\partial\Phi}{\partial I_2}\right] \tag{62}$$

in 2D and

$$\alpha_E(\mathbf{s}_h) = \frac{1}{9}\left[4I_1\frac{\partial^2\Phi}{\partial I_1\partial I_1} + \left(4I_1\,I_2 + 12J^2\right)\frac{\partial^2\Phi}{\partial I_2\partial I_2} + I_2\frac{\partial^2\Phi}{\partial J\partial J} + 16I_2\frac{\partial^2\Phi}{\partial I_1\partial I_2} + 12J\frac{\partial^2\Phi}{\partial I_1\partial J} + 4J\,I_1\frac{\partial^2\Phi}{\partial I_2\partial J} + 18\frac{\partial\Phi}{\partial I_1} + 8I_1\frac{\partial\Phi}{\partial I_2}\right] \tag{63}$$

in 3D, where implicit dependences of I_1, I_2 and J on $\mathit{\Pi}_E^0\nabla\mathbf{s}_h$ are assumed. The above explicit expressions are helpful to enable the more intuitive choice of $\mathbf{s}_h = \mathbf{u}_h$ in the implementation, which is found to render the VEM approximations independent of the loading history, as well as more tolerant to heterogeneous and large localized deformations than the choice of $\mathbf{s}_h = \mathbf{u}_h^{n-1}$. On the other hand, unlike choosing $\mathbf{s}_h = \mathbf{0}$ and $\mathbf{u}_h^{n-1}$, $\alpha_E(\mathbf{u}_h)$ becomes a nonlinear function of $\mathbf{u}_h$, resulting additional terms in the weak forms of the VEM approximations in practice. A summary of the above stabilization choices can be found in Table 2. In this paper, we test most of the choices in our numerical studies.

5.4. Construction of the loading terms

We present the constructions of first order accurate loading terms which, according to [27], guarantee the optimal convergence of the displacement and its gradient in the $\mathcal{L}^2$ error.

To construct the loading term associated with surface traction $\langle\mathbf{t}, \mathbf{v}_h\rangle_h$, a first order Gauss–Lobatto quadrature rule is used in 2D with the quadrature points being the vertices v on $\mathit{\Gamma}_h^{\mathbf{t}}$,

$$\langle\mathbf{t}, \mathbf{v}_h\rangle_h = \sum_{v\in\mathit{\Gamma}_h^{\mathbf{t}}} w_v\mathbf{t}(\mathbf{X}_v)\cdot\mathbf{v}_h(\mathbf{X}_v), \quad \forall\mathbf{v}_h\in\mathcal{K}_h, \tag{64}$$

where X_v is the position vector associated with vertex v and w_v is the weight associated with v defined by a first order Gauss–Lobatto rule. On the other hand, the vertex-based quadrature defined by (25) over f with m^f vertices is adopted in 3D as follows:

$$\langle\mathbf{t}, \mathbf{v}_h\rangle_h = \sum_{f\in\mathit{\Gamma}_h^{\mathbf{t}}}\sum_{j=1}^{m^f} w_j^f\mathbf{t}\left(\mathbf{X}_j^f\right)\cdot\mathbf{v}_h\left(\mathbf{X}_j^f\right), \quad \forall\mathbf{v}_h\in\mathcal{K}_h. \tag{65}$$

Notice that in both 2D and 3D cases, the loading term $\langle\mathbf{t}, \mathbf{v}_h\rangle_h$ yields exact integral when $\mathbf{t}$ is constant on each edge or face of $\mathit{\Gamma}_h^{\mathbf{t}}$, i.e.

$$\langle\mathbf{t}, \mathbf{v}_h\rangle_h = \int_{\mathit{\Gamma}_h^{\mathbf{t}}}\mathbf{t}\cdot\mathbf{v}_h\mathrm{d}S, \quad \forall\mathbf{v}_h\in\mathcal{K}_h. \tag{66}$$

Regarding the loading term associated with the body force $\langle \mathbf{f}, \mathbf{v}_h \rangle_h$, various approaches can be utilized. We consider two approaches in this work, neither of which needs explicit knowledge of $\mathbf{v}_h$ in the interior of each element E. The first approach utilizes a (first order) vertex-based quadrature over each element in 2D and 3D,

$$\text{Approach \#1: } \langle \mathbf{f}, \mathbf{v}_h \rangle_h = \sum_E \sum_{v \in E} w_v^E \mathbf{f}(\mathbf{X}_v) \cdot \mathbf{v}_h(\mathbf{X}_v), \quad \forall \mathbf{v}_h \in \mathcal{K}_h, \tag{67}$$

where $\mathbf{X}_v$ denotes the location of vertex v of E and w_v^E is the associated weight defined in [27,30]. Notice that the first order accuracy of the nodal quadrature rule in [27,30] is only valid for convex elements and certain concave elements in 2D and 3D. For instance, with the presence of non star-convex elements, certain weights in the nodal become negative and moreover the first order accuracy may be no longer satisfied.

We also propose another approach for the construction of the loading term $\langle \mathbf{f}, \mathbf{v}_h \rangle_h$, which is of the form

$$\text{Approach \#2: } \langle \mathbf{f}, \mathbf{v}_h \rangle_h = \sum_E \mathbf{f}\left(\mathbf{X}_C^E\right) \cdot \left(\Pi_E^\nabla \mathbf{v}_h\right)\left(\mathbf{X}_C^E\right), \quad \forall \mathbf{v}_h \in \mathcal{K}_h, \tag{68}$$

where $\mathbf{X}_C^E \doteq \int_E \mathbf{X} \mathrm{d}\mathbf{X}/|E|$ stands for the centroid of element E, which can be calculated for any given elements with arbitrary shapes in 2D and 3D. Although the centroid $\mathbf{X}_C^E$ may not lie in the interior of E, we can show that this construction of the body force term is first order accurate for elements with arbitrary shapes, such as non star-shaped elements, in both 2D and 3D as long as Π_E^∇ is well defined. In fact, a two dimensional example will be presented in a subsequent section which confirms that VEM with the second load construction produces optimally convergent results also for non star-shaped elements. The only limitation of this second choice is that, whenever $\mathbf{X}_C^E \notin E$, loadings that are discontinuous across mesh edges may yield less accurate results.

5.5. Weak forms of the VEM approximations

With the proposed stabilization parameter and loading terms, the weak form for the displacement-based VEM approximation (53) and (56) is given by (assuming the trace-based stabilization scheme in which $\mathbf{s}_h$ is taken as the current displacement)

$$\begin{aligned} G_h(\mathbf{v}_h, \delta\mathbf{v}_h) = & \sum_E \left[|E| \frac{\partial \Psi}{\partial \mathbf{F}} \left(\mathbf{I} + \Pi_E^0 \nabla \mathbf{v}_h \right) + \frac{1}{2} S_{h,E} \left(\mathbf{v}_h - \Pi_E^\nabla \mathbf{v}_h, \mathbf{v}_h - \Pi_E^\nabla \mathbf{v}_h \right) \frac{\partial \alpha_E}{\partial \mathbf{F}} (\mathbf{v}_h) \right] : \Pi_E^0 \nabla (\delta \mathbf{v}_h) \\ & + \sum_E \alpha_E(\mathbf{v}_h) S_{h,E} \left(\mathbf{v}_h - \Pi_E^\nabla \mathbf{v}_h, \delta \mathbf{v}_h - \Pi_E^\nabla (\delta \mathbf{v}_h) \right) + \sum_E |E| \frac{\mathrm{d}U}{\mathrm{d}J} (J_E(\mathbf{v}_h)) \, DJ_E(\mathbf{v}_h) \cdot \delta \mathbf{v}_h|_E \\ & - \langle \mathbf{f}, \delta \mathbf{v}_h \rangle_h - \langle \mathbf{t}, \delta \mathbf{v}_h \rangle_h = 0 \quad \forall \delta \mathbf{v}_h \in \mathcal{K}_h^0. \end{aligned} \tag{69}$$

On the other hand, the weak forms of the first variation of the two-field mixed VEM approximation (50) and (58) take the following form:

$$\begin{aligned} G_h^{\mathbf{v}}(\mathbf{v}_h, \widehat{q}_h, \delta\mathbf{v}_h) = & \sum_E \left[|E| \frac{\partial \Psi}{\partial \mathbf{F}} \left(\mathbf{I} + \Pi_E^0 \nabla \mathbf{v}_h \right) + \frac{1}{2} S_{h,E} \left(\mathbf{v}_h - \Pi_E^\nabla \mathbf{v}_h, \mathbf{v}_h - \Pi_E^\nabla \mathbf{v}_h \right) \frac{\partial \alpha_E}{\partial \mathbf{F}} (\mathbf{v}_h) \right] : \Pi_E^0 \nabla (\delta \mathbf{v}_h) \\ & + \sum_E \alpha_E(\mathbf{v}_h) S_{h,E} \left(\mathbf{v}_h - \Pi_E^\nabla \mathbf{v}_h, \delta \mathbf{v}_h - \Pi_E^\nabla (\delta \mathbf{v}_h) \right) + \sum_E |E| \widehat{q}_h|_E \left(DJ_E(\mathbf{v}_h) \cdot \delta \mathbf{v}_h|_E \right) \\ & - \langle \mathbf{f}, \delta \mathbf{v}_h \rangle_h - \langle \mathbf{t}, \delta \mathbf{v}_h \rangle_h = 0 \quad \forall \delta \mathbf{v}_h \in \mathcal{K}_h^0, \end{aligned} \tag{70}$$

and

$$G_h^{\widehat{q}}(\mathbf{v}_h, \widehat{q}_h, \delta\widehat{q}_h) = \sum_E |E| \left\{ \widehat{q}_h|_E \left[J_E(\mathbf{v}_h) - 1 \right] - \frac{\mathrm{d}\widehat{U}^*}{\mathrm{d}\widehat{q}} (\widehat{q}_h|_E) \, \delta\widehat{q}_h|_E \right\} = 0 \quad \forall \delta\widehat{q}_h \in \mathcal{Q}_h. \tag{71}$$

We underline that, whenever $\mathbf{s}_h$ is taken as the displacement at the previous load increment iteration step $\mathbf{u}_h^{n-1}$ (see Section 5.3), the addendum involving $\partial \alpha_E / \partial \mathbf{F}$ in both the right hand sides of (69) and (70) vanishes, and $\alpha_E(\mathbf{v}_h)$ becomes $\alpha_E(\mathbf{u}_h^{n-1})$.

5.6. On the VEM patch test

We provide a brief discussion on the performance of VEM approximations in the patch test. In the discussion that follows, we restrict our attention to cases where the geometry and boundary conditions are exactly represented by the mesh, namely, no error arises from the approximation of geometry in the following discussion.

In the patch test, the unknown displacement field is taken to be a linear vector field, i.e., $\mathbf{u} = \mathbf{p}_1 \in [\mathcal{P}_1(\Omega)]^d$. Accordingly, the first Piola–Kirchhoff stress $\mathbf{P}$ is a constant tensor given by $\mathbf{P} = \partial\Psi(\mathbf{F}(\mathbf{p}_1))/\partial\mathbf{F} + \partial U(J(\mathbf{p}_1))/\partial\mathbf{F}$. The body force $\mathbf{f}$ is $\mathbf{0}$ everywhere and the boundary traction $\mathbf{t}$ is given by $\mathbf{t} = \mathbf{P}\mathbf{n}$ on $\Gamma^{\mathbf{X}}$ where $\mathbf{n}$ is the outward unit normal vector on the boundary. Additionally, the known pressure field $\widehat{p}_0$ is a constant field taking value $\frac{\partial U}{\partial J}(J(\mathbf{p}_1))$ unless in the presence of a purely incompressible solid, in which case $\widehat{p}_0$ is determined by the applied traction $\mathbf{t}$. Furthermore, for any linear function $\mathbf{p}_1 \in [\mathcal{P}_1(\Omega)]^d$, $\nabla\mathbf{p}_1$ and $\mathbf{F}(\mathbf{p}_1)$ are constant tensors. It follows that for any $E \in \Omega_h$,

$$\Pi_E^0(\nabla\mathbf{p}_1|_E) = \nabla\mathbf{p}_1 \tag{72}$$

$$\Pi_E^{\nabla}(\mathbf{p}_1|_E) = \mathbf{p}_1|_E \quad \text{and} \tag{73}$$

$$J_E(\mathbf{p}_1) = J(\mathbf{p}_1) = \det(\mathbf{F}(\mathbf{p}_1)). \tag{74}$$

We proceed to verify the exact satisfaction of the patch test with the proposed displacement-based and two-field mixed VEM approximations by demonstrating that $\mathbf{v}_h = \mathbf{p}_1$ and $\widehat{q}_h = \widehat{p}_0$ are solutions to Eqs. (69)–(71). Let us first consider the displacement-based VEM approximation. Realizing that exact integration is recovered in the following two terms as a result of (72)–(74)

$$|E|\frac{\partial\Psi}{\partial\mathbf{F}}(\mathbf{F}(\mathbf{p}_1)) : \Pi_E^0(\nabla(\delta\mathbf{v}_h)) = \int_E \frac{\partial\Psi}{\partial\mathbf{F}}(\mathbf{F}(\mathbf{p}_1)) : \nabla(\delta\mathbf{v}_h)\mathrm{d}\mathbf{X} \tag{75}$$

and

$$|E|\frac{\mathrm{d}U}{\mathrm{d}J}(J_E(\mathbf{p}_1))\, DJ_E(\mathbf{p}_1)\cdot\delta\mathbf{v}_h|_E = \int_E \frac{\mathrm{d}U}{\mathrm{d}J}(J(\mathbf{p}_1))\frac{\partial J}{\partial\mathbf{F}}(\mathbf{F}(\mathbf{p}_1)) : \nabla(\delta\mathbf{v}_h)\mathrm{d}\mathbf{X}, \tag{76}$$

we have that for any trial field $\delta\mathbf{v}_h \in \mathcal{K}_h^0$

$$\begin{aligned} G_h(\mathbf{p}_1, \delta\mathbf{v}_h) &= \sum_E \int_E \left[\frac{\partial\Psi}{\partial\mathbf{F}}(\mathbf{F}(\mathbf{p}_1)) + \frac{\mathrm{d}U}{\mathrm{d}J}(J(\mathbf{p}_1))\frac{\partial J}{\partial\mathbf{F}}(\mathbf{F}(\mathbf{p}_1))\right] : \nabla(\delta\mathbf{v}_h)\mathrm{d}\mathbf{X} - \langle\mathbf{t}, \delta\mathbf{v}_h\rangle_h \\ &= \int_\Omega \left[\frac{\partial\Psi}{\partial\mathbf{F}}(\mathbf{F}(\mathbf{p}_1)) + \frac{\mathrm{d}U}{\mathrm{d}J}(J(\mathbf{p}_1))\frac{\partial J}{\partial\mathbf{F}}(\mathbf{F}(\mathbf{p}_1))\right] : \nabla(\delta\mathbf{v}_h)\mathrm{d}\mathbf{X} - \int_{\Gamma_h^{\mathbf{t}}} \mathbf{t}\cdot\delta\mathbf{v}_h\mathrm{d}S = 0, \end{aligned} \tag{77}$$

where the second equality in the above relation follows from the fact that $\mathbf{t}$ is constant on each edge/face together with relation (66).

For the two-field mixed VEM approximation, we are able to show in a similar manner that for any $\delta\mathbf{v}_h \in \mathcal{K}_h^0$,

$$G_h^{\mathbf{v}}(\mathbf{p}_1, \widehat{p}_0, \delta\mathbf{v}_h) = \sum_E \int_E \left[\frac{\partial\Psi}{\partial\mathbf{F}}(\mathbf{F}(\mathbf{p}_1)) + \widehat{p}_0\frac{\partial J}{\partial\mathbf{F}}(\mathbf{F}(\mathbf{p}_1))\right] : \nabla(\delta\mathbf{v}_h)\mathrm{d}\mathbf{X} - \langle\mathbf{t}, \delta\mathbf{v}_h\rangle_h = 0, \tag{78}$$

and for any $\delta\widehat{q}_h \in \mathcal{Q}_h$

$$\begin{aligned} G_h^{\widehat{q}}(\mathbf{p}_1, \widehat{p}_0, \delta\widehat{q}_h) &= \sum_E |E| \left\{[J_E(\mathbf{p}_1) - 1]\,\delta\widehat{q}_h|_E - \frac{\mathrm{d}\widehat{U}^*}{\mathrm{d}\widehat{q}}(\widehat{p}_0)\,\delta\widehat{q}_h|_E\right\} \\ &= \sum_E \int_E \left[J(\mathbf{p}_1) - 1 - \frac{\mathrm{d}\widehat{U}^*}{\mathrm{d}\widehat{q}}(\widehat{p}_0)\right]\delta\widehat{q}_h\mathrm{d}\mathbf{X} = 0. \end{aligned} \tag{79}$$

According to the above analysis, both displacement-based and two-field mixed VEM approximations pass the patch test exactly in 2D and 3D. In fact, although not presented in this paper, our numerical studies confirm that the patch tests are passed with errors up to machine precisions for both displacement-based and mixed VEM approximations.

5.7. A note on the performance of polyhedral elements with non star-convex faces in patch tests

The discussion in the last subsection is applicable to meshes consisting of polyhedral elements with faces that are star-convex with respect to $\mathbf{X}_s^f$. In the case where the element E contains any face f that is not star-convex with respect to $\mathbf{X}_s^f$, the local displacement VEM space $\mathcal{V}(E)$ is not well defined according to its formal definition (21) because certain regions of the triangulated subdomains may lie outside of f. However, our numerical studies demonstrate that convergence (in terms of DOFs) is still achieved with the VEM formulations even for meshes with elements containing non star-convex faces. While a more rigorous theoretical analysis is beyond the scope of this paper, we demonstrate that the patch test is strictly passed with our mixed VEM formulation even when the meshes contain elements with non star-convex faces. A similar analysis can also be applied to the displacement-based VEM formulation.

To begin with, although the element space $\mathcal{V}(E)$ is not well defined when E contains non star-convex faces, we remark that the projection $\Pi_E^0 \nabla \mathbf{v}$, is still computable numerically using the nodal values of $\mathbf{v}$ and the vertex based quadrature rule defined in (25):

$$\Pi_E^0 \nabla \mathbf{v} = \frac{1}{|E|} \sum_{f \in \partial E} \sum_{j=1}^{m^f} \left\{ w_j^f \mathbf{v}\left(\mathbf{X}_j^f\right) \otimes \mathbf{n}_f \right\}, \tag{80}$$

where the weights w_j^f may take negative values. The same also applies to the other projection $\Pi_E^\nabla \mathbf{v}$.

As we will show in detail in Appendix B, with the definition of the vertex-based rule on f in (25) and (80), the following expression holds

$$\Pi_E^0 \nabla \mathbf{p}_1 = \frac{1}{|E|} \sum_{f \in \partial E} \sum_{j=1}^{m^f} \left\{ w_j^f \mathbf{p}_1\left(\mathbf{X}_j^f\right) \otimes \mathbf{n}_f \right\} = \frac{1}{|E|} \int_E \nabla \mathbf{p}_1 \mathrm{d}\mathbf{X}, \quad \forall \mathbf{p}_1 \in [\mathcal{P}_1(E)]^3 \tag{81}$$

even if E contains non star-convex faces.

Furthermore, if E contains non star-convex faces, we are able to show that both the "Robust" and "Simple" approaches of Table 1 give exact J_E for any linear displacement field $\mathbf{u} = \mathbf{p}_1 \in [\mathcal{P}_1(E)]^3$, namely,

$$\frac{1}{6|E|} \sum_{\widetilde{f}} \sum_{j=1}^{m^f} \left\{ \widetilde{\mathbf{X}}_s^f \cdot \widetilde{\mathbf{X}}_j^f \wedge \widetilde{\mathbf{X}}_{j+1}^f \right\} = J_E\left(\mathbf{p}_1\right). \tag{82}$$

Analogous calculations for the first variation of J_E show that expressions (42) (the "Robust" approach) and (47) (the "Simple" approach) are also valid for the non star-convex case, i.e.,

$$DJ_E(\mathbf{p}_1) \cdot \delta\mathbf{v} = |E| \frac{\partial J}{\partial \mathbf{F}}\left(\mathbf{F}(\mathbf{p}_1)\right) : \Pi_E^0\left(\nabla(\delta\mathbf{v})\right). \tag{83}$$

Based on (80)–(83) and realizing that relations (72)–(74) still hold when E contains non star-convex faces, we are able to show that for any trial fields $\delta\mathbf{v}_h \in \mathcal{K}_h^0$ and $\delta\widehat{q}_h \in \mathcal{Q}_h$, both the "Robust" and "Simple" approaches give

$$G_h^{\mathbf{v}}(\mathbf{p}_1, \widehat{p}_0, \delta\mathbf{v}_h) = 0 \text{ and } G_h^{\widehat{q}}(\mathbf{p}_1, \widehat{p}_0, \delta\widehat{q}_h) = 0, \tag{84}$$

indicating that the patch test is strictly passed for mixed VEM even when E contains non star-convex faces. Thorough derivations of expressions (81)–(84) are provided in Appendix B.

6. Numerical assessment

This section presents a series of numerical studies to assess the performance of the displacement-based and mixed VEM approximations in two- and three-dimensional finite elasticity problems. In particular, studies on families of subsequently refined meshes are conducted, through which we demonstrate the performance of VEM formulations on convergence and accuracy.

Unless otherwise stated, the VEM approximations adopt the trace-based stabilization with the choice of $\mathbf{s}_h = \mathbf{u}_h$ throughout this section. For any polyhedral element E, a uniform β_i^f on each face f with m^f vertices is assumed for the remainder of the paper, namely, $\beta_i^f = 1/m^f$, $i = 1, \ldots, m^f$. For any given convex polyhedron this choice leads to well-defined local VEM space $\mathcal{V}(E)$ because every face f is guaranteed to be star-shaped with respect to the resulting $\mathbf{X}_s^f$. To solve the nonlinear system of equations, the standard Newton–Raphson method is utilized; as a stopping criterion, we check at each iteration if the Euclidean norm of the residual vector reduces below 10^{-8} times that of the initial residual. To generate 2D polygonal meshes, the general purpose mesh generator "PolyMesher" [48] is used, while for generating 3D polyhedral meshes, the methodology and algorithm provided in [49] are adopted.

To evaluate the accuracy of the numerical solutions, two global error measures of the displacement field are used, the $\mathcal{L}^2$-norm and $\mathcal{H}^1$-seminorm of the displacement error, which are defined as[2]

$$\epsilon_{0,\mathbf{u}} = \|\mathbf{u} - \Pi_E^{\nabla}\mathbf{u}_h\| \text{ and } \epsilon_{1,\mathbf{u}} = \|\nabla\mathbf{u} - \Pi_E^0(\nabla\mathbf{u}_h)\| \tag{86}$$

where the $\|\cdot\|$ (when applied to functions) stands for the $\mathcal{L}^2$ norm over Ω that is evaluated using a fifth order triangulation quadrature scheme. For the meshes with non star-shaped elements, the above defined displacement error measures become difficult to evaluate due to the failure of the triangulation quadrature scheme. Instead, we adopt the following $\mathcal{L}^2$-type and $\mathcal{H}^1$-type displacement error measures, which utilize only the displacement errors at the vertices of the mesh,[3]

$$\epsilon_{0,\mathbf{u}}^v = \left[\sum_E \frac{|E|}{m}\sum_{v\in E}\mathbf{e}(\mathbf{X}_v)\cdot\mathbf{e}(\mathbf{X}_v)\right]^{1/2}, \tag{88}$$

$$\epsilon_{1,\mathbf{u}}^v = \left[\sum_E h_E\sum_{e\in E}\left[\mathbf{e}\left(\mathbf{X}_{v_1^e}\right)-\mathbf{e}\left(\mathbf{X}_{v_2^e}\right)\right]\cdot\left[\mathbf{e}\left(\mathbf{X}_{v_1^e}\right)-\mathbf{e}\left(\mathbf{X}_{v_2^e}\right)\right]/|e|\right]^{1/2} \quad \text{in 2D} \tag{89}$$

and

$$\epsilon_{1,\mathbf{u}}^v = \left\{\sum_E h_E\sum_{f\in E}h_f\sum_{e\in f}\left[\mathbf{e}\left(\mathbf{X}_{v_1^e}\right)-\mathbf{e}\left(\mathbf{X}_{v_2^e}\right)\right]\cdot\left[\mathbf{e}\left(\mathbf{X}_{v_1^e}\right)-\mathbf{e}\left(\mathbf{X}_{v_2^e}\right)\right]/|e|\right\}^{1/2} \quad \text{in 3D} \tag{90}$$

where $\mathbf{e} = \mathbf{u} - \mathbf{u}_h$ is the displacement error, m is the number of vertices in E, h_E and h_f denote the diameters of E and face f, and v_1^e and v_2^e are the two endpoints of edge e. We remark that expressions (89) and (90) mimic the $\mathcal{H}^1$-seminorms of the displacement in the following sense: they take differences of the displacement on the skeleton of the mesh, and those differences are then scaled in order to achieve the same behavior (with respect to element contractions/expansions) as the $\mathcal{L}^2$-norm of the displacement gradient.

For the mixed formulations in addition to the error measures for displacements defined in (86)–(90), we consider the $\mathcal{L}^2$ pressure errors[4]

$$\epsilon_{0,\widehat{p}} = \|\widehat{p} - \widehat{p}_h\|, \tag{92}$$

[2] Alternatively, the norms could be scaled as

$$\epsilon_{0,\mathbf{u}} \to \epsilon_{0,\mathbf{u}}/\|\mathbf{u}\|, \quad \epsilon_{1,\mathbf{u}} \to \epsilon_{1,\mathbf{u}}/\|\nabla\mathbf{u}\|. \tag{85}$$

[3] Alternatively, the norms could be scaled as

$$\epsilon_{0,\mathbf{u}}^v \to \epsilon_{0,\mathbf{u}}^v/\|\mathbf{u}\|, \quad \epsilon_{1,\mathbf{u}}^v \to \epsilon_{1,\mathbf{u}}^v/\|\nabla\mathbf{u}\|. \tag{87}$$

[4] Alternatively, the norms could be scaled as

$$\epsilon_{0,\widehat{p}} \to \epsilon_{0,\widehat{p}}/\|\widehat{p}\|, \quad \epsilon_{0,\widehat{p}}^v \to \epsilon_{0,\widehat{p}}^v/\|\widehat{p}\| \tag{91}$$

For the displacement-based formulation, the exact displacement field is given by Eq. (95) and $\|\mathbf{u}\| = 3.2953$, $\|\nabla\mathbf{u}\| = 3.5816$. For the mixed formulation, the exact displacement and pressure fields are given by Eqs. (99) and (101), and $\|\mathbf{u}\| = 3.4425$, $\|\nabla\mathbf{u}\| = 3.6736$, $\|\widehat{p}\| = 2.7572$, where the norms are computed exactly.

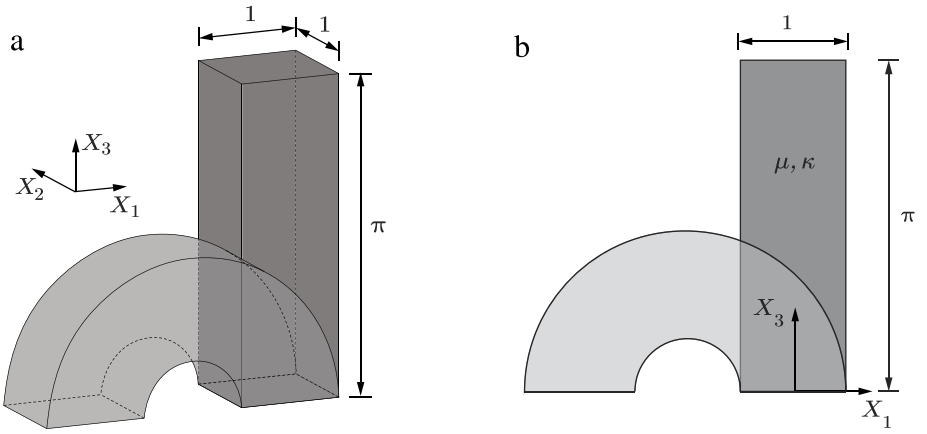

Fig. 3. (a) Illustration of the 3D boundary value problems where a rectangular block is bent into semicircular shapes. (b) Illustration of the simplified 2D plane strain problems. In the problem for the displacement-based VEM, the initial bulk modulus is set as $\kappa = 10$ and, in the one for the mixed VEM, κ is taken to be $\kappa \to \infty$. In all cases, $\mu = 1$.

where the norms are evaluated using a fifth order triangulation quadrature rule. For meshes with non star-shaped elements, a $\mathcal{L}^2$-type pressure error is defined as

$$\epsilon^v_{0,\widehat{p}} = \left[\sum_E |E| \sum_{v \in E} \left[\widehat{p}(\mathbf{X}_v) - \widehat{p}_h(\mathbf{X}_v) \right]^2 / m \right]^{1/2}, \tag{93}$$

which utilizes the pressure errors at the vertices of the mesh.

6.1. Displacement-based VEM

This subsection considers the numerical assessments on the performance of both two- and three-dimensional displacement-based VEM. Throughout this subsection, material behavior is considered to be neo-Hookean with the following stored-energy function [38]:

$$W(\mathbf{F}) = \frac{\mu}{2}(I_1(\mathbf{F}) - 3) - \mu(\det \mathbf{F} - 1) + \frac{3\kappa + \mu}{6}(\det \mathbf{F} - 1)^2, \tag{94}$$

where μ and κ are the initial shear and bulk moduli, which are taken to be $\mu = 1$ and $\kappa = 10$ in the remainder of this subsection. Realizing that $\Psi(\mathbf{F}) = \mu/2(\mathbf{F} : \mathbf{F} - 3)$ in the above stored energy function, we obtain the trace-based stabilization term $\alpha_E = \mu$ for both 2D and 3D cases according to (62) and (63), which is independent of the deformation state $\mathbf{u}$. Additionally, J_E is computed exactly using the "Robust" approach (Table 1) leading to (33) and (41) for 2D and 3D cases respectively. In general, we have found that computing J_E using the "Simple" approach also produces results with similar accuracy for the meshes with regular elements, e.g., convex elements.

This subsection considers a boundary value problem where a rectangular block of dimensions $1 \times 1 \times \pi$ is bent into a semi-circular shape, as illustrated in Fig. 3(a). The rectangular block is defined by $-0.5 < X_1 < 0.5, 0.5 < X_2 < 0.5$ and $0 < X_3 < \pi$ in a Cartesian coordinate system (X_1, X_2, X_3), and the analytical displacement describing the deformation is given by

$$u_x(\mathbf{X}) = -1 + (1 + X_1)\cos(X_3) - X_1, \quad u_y(\mathbf{X}) = 0, \quad u_z(\mathbf{X}) = (1 + X_1)\sin(X_3) - X_3. \tag{95}$$

Accordingly, the body force $\mathbf{f} = \{f_x, f_y, f_z\}^T$ is computed as

$$f_x(\mathbf{X}) = -\frac{(1 + X_1)\cos(X_3)(3\kappa - 2\mu)}{3}, \quad f_y(\mathbf{X}) = 0, \quad f_z(\mathbf{X}) = -\frac{(1 + X_1)\sin(X_3)(3\kappa - 2\mu)}{3}. \tag{96}$$

Since no deformation occurs in the X_2 direction, this problem simplifies into a plane strain problem in the $X_1 - X_3$ plane, as shown in Fig. 3(b). In the following studies, displacement boundary conditions are applied everywhere on

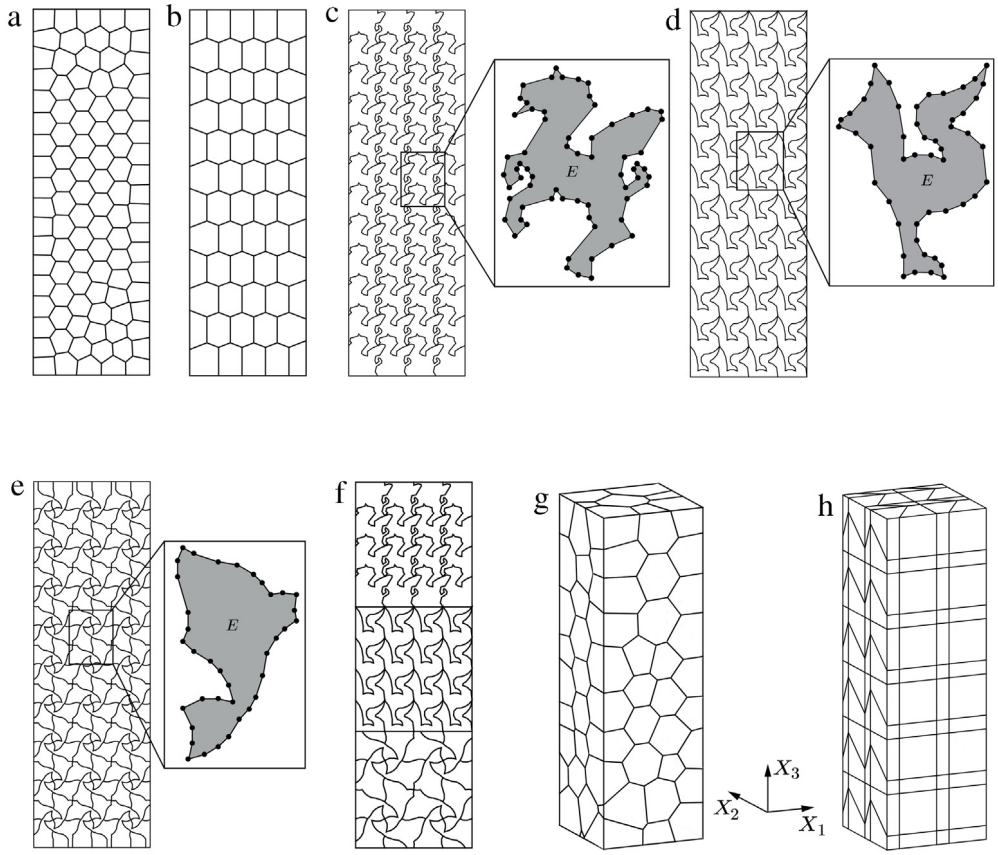

Fig. 4. Examples of (a) a CVT mesh consisting of 100 2D elements; (b) a structured hexagonal mesh consisting of 60 2D elements; (c) a pegasus mesh containing 48 non star-shaped 2D elements; (d) a bird mesh with 64 non star-shaped 2D elements; (e) a fish mesh consisting of 132 non star-shaped 2D elements; (f) a "zoo" mesh containing a total number of 64 non star-shape 2D elements, including 16 pegasus elements, 20 bird elements and 28 fish elements; (g) a CVT mesh consisting of 100 3D elements; and (h) a distorted hexahedral mesh consisting of 96 3D elements.

the boundary in both the original 3D problem and its 2D simplification. Both 2D and 3D problems have identical $\mathcal{L}^2$ norms for the exact displacement and its gradient, which are obtained as $\|\mathbf{u}\| = 3.2953$ and $\|\nabla\mathbf{u}\| = 3.5816$ analytically.

2D displacement-based VEM. We first consider the VEM in 2D and study its performance in the boundary value problems under plane strain conditions. To that end, we consider the simplified plane strain problem setup illustrated in Fig. 3(b). Two sets of convex meshes are considered, the structured hexagonal meshes and the CVT meshes, examples of which are provided in Fig. 4(a) and (b) respectively. The VEM results include both Approaches #1 and #2 for treating the body force term, i.e. expressions (67) and (68). For comparison purpose, we also conduct analysis using the standard displacement-based FEM with the gradient correction scheme [23,13] on the same sets of polygonal meshes. Fig. 5 plots the displacement errors as functions of the average mesh size h. Each data point for the CVT mesh represents an average of the results from five meshes. It is observed that VEM with both Approaches #1 and #2 for treating the body force term delivers optimal convergence rates (2 for the $\mathcal{L}^2$-norm of the displacement error and 1 for the $\mathcal{H}^1$-seminorm of the displacement errors), whose results have almost identical accuracy. When compared to the FEM, the VEM also gives displacement fields with similar accuracy (although the VEM results are slightly less accurate in terms of the $\mathcal{H}^1$-seminorm than the FEM results). However, the VEM is more efficient than the FEM in the sense that the VEM uses only one integration point per element whereas the FEM uses n integration points for n-sided elements.

One major advantage of the VEM is its ability to deal with more general meshes in an efficient way. To demonstrate this advantage, we consider three sets of Escher-based meshes [50]: the pegasus mesh as shown in Fig. 4(c), the bird

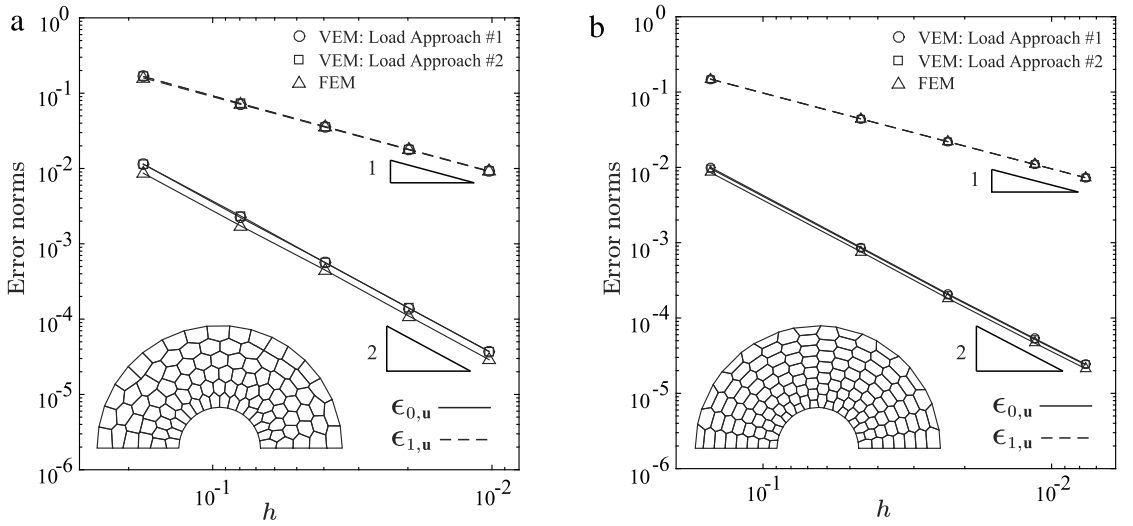

Fig. 5. The convergence plots of the error norms as functions of the average mesh size h for the (a) the CVT meshes and (b) the structured hexagonal meshes.

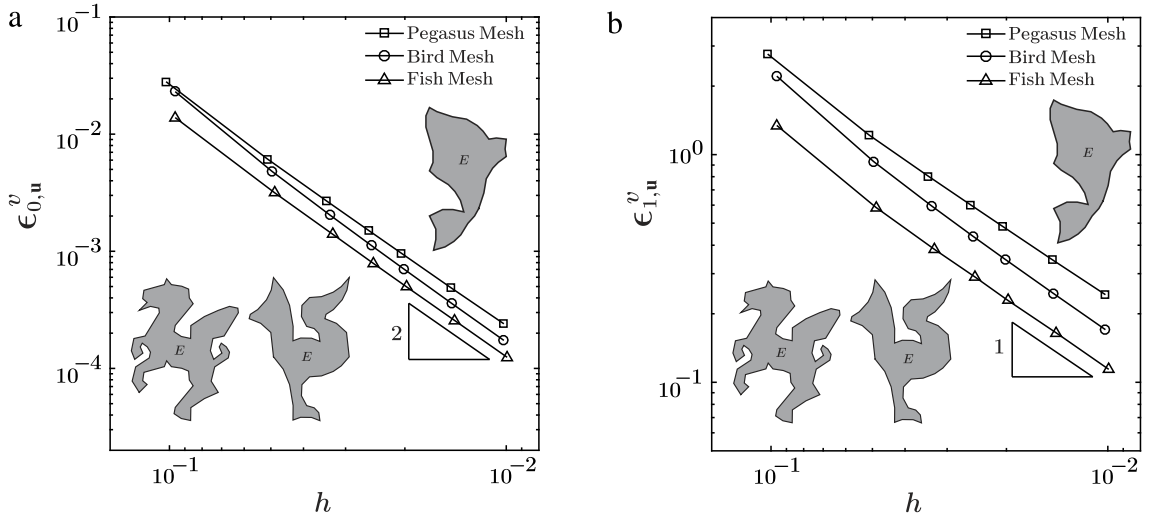

Fig. 6. The convergence plots of the displacement error norms against average mesh size h for both the bird and pegasus meshes: (a) the $\mathcal{L}^2$-type displacement error and (b) the $\mathcal{H}^1$-type displacement error.

mesh as shown in Fig. 4(d), and the fish mesh as shown in Fig. 4(e). Following the discussion of Section 4, because the Approach #1 in (67) fails with the non star-shaped elements, the body force term here is constructed using the Approach #2 given by (68). Fig. 6(a) and (b) show the two error measures (88) and (89) as functions of the average mesh size h. In addition, examples of the deformed shapes of all sets of meshes are shown in Figs. 7–9. Our numerical results confirm that optimal convergences are obtained in both the $\mathcal{L}^2$-type and $\mathcal{H}^1$-type norms of the displacement error. As an additional remark, we point out that the VEM using the "Simple" approach (see Table 1) to compute J_E in this case is found to lead to non-convergent results due to the failure of convergence in the Newton–Raphson method.

3D displacement-based VEM. We proceed to perform numerical assessments of the displacement-based VEM in 3D. In this case, we consider original 3D problem illustrated in Fig. 3(a) with the CVT and the distorted hexahedral meshes, examples of which are shown in Fig. 4(g) and (h), respectively. We also consider both approaches of treating the body force term given by (67) and (68), and the displacement error measures defined in (86) are used here. Fig. 10(a) and

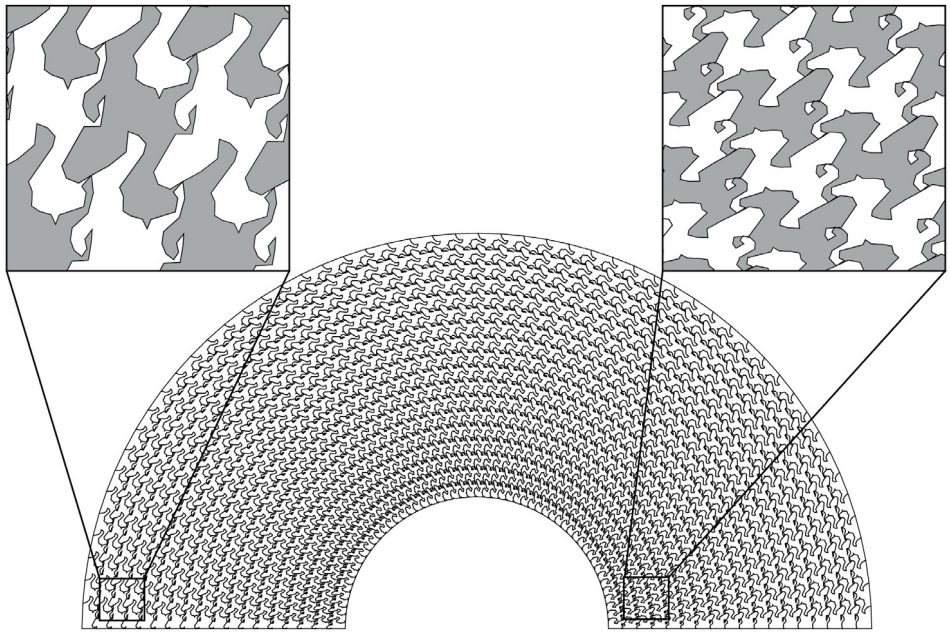

Fig. 7. The final deformed configuration is shown for the pegasus mesh with 972 elements. This deformed shape is obtained by the displacement-based VEM.

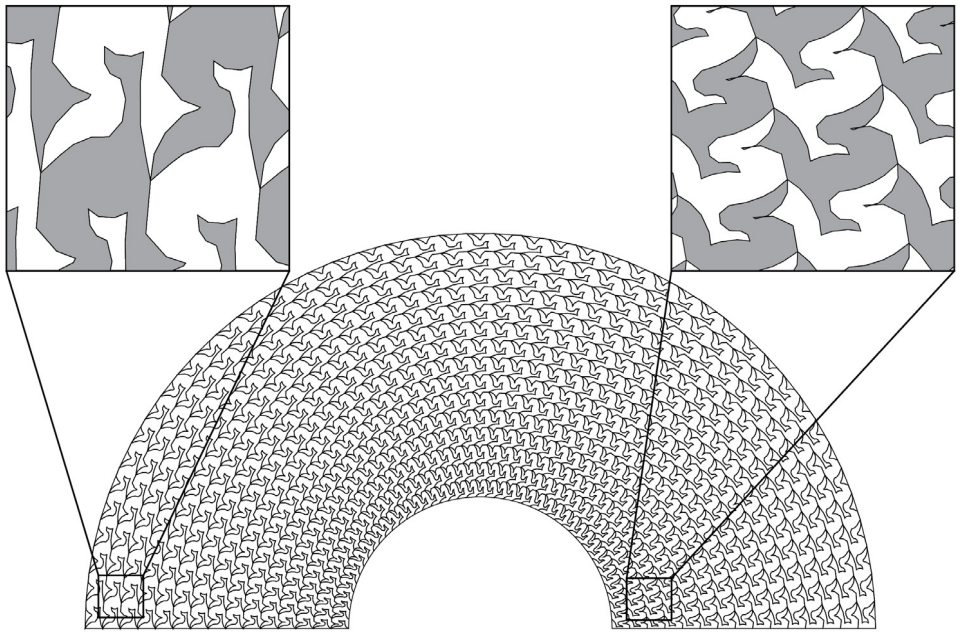

Fig. 8. The final deformed configuration is shown for the bird mesh with 735 elements. This deformed shape is obtained by the displacement-based VEM.

(b) show plots of the displacement error norms as functions of the average mesh sizes h. Each data point in the plots for the CVT mesh is obtained by averaging the results from five meshes. Again, VEM using both Approaches #1 and #2 of treating the body force term yields an optimally convergent displacement field with similar accuracy.

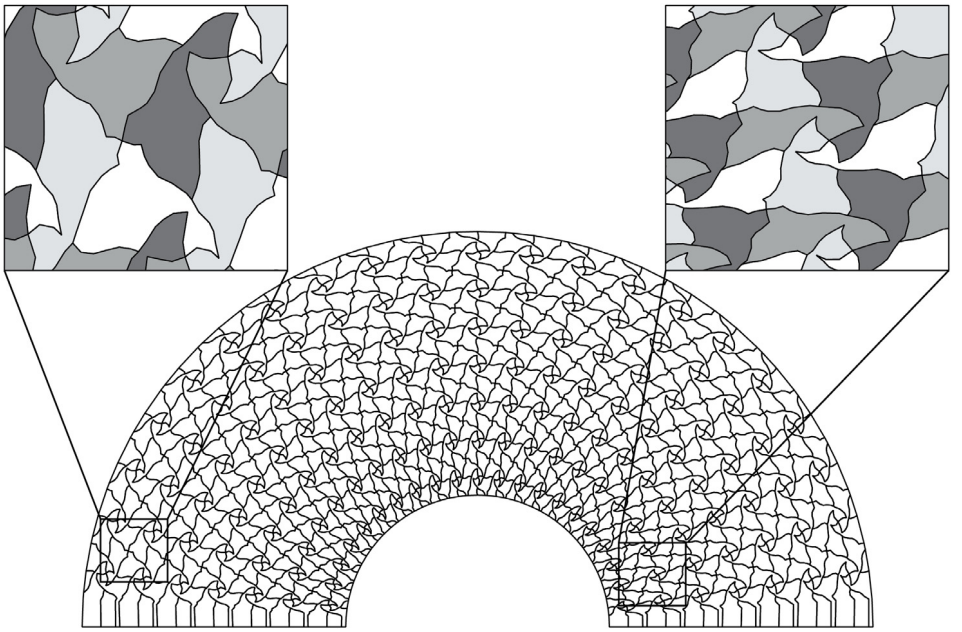

Fig. 9. The final deformed configuration is shown for the fish mesh with 644 elements. This deformed shape is obtained by the displacement-based VEM.

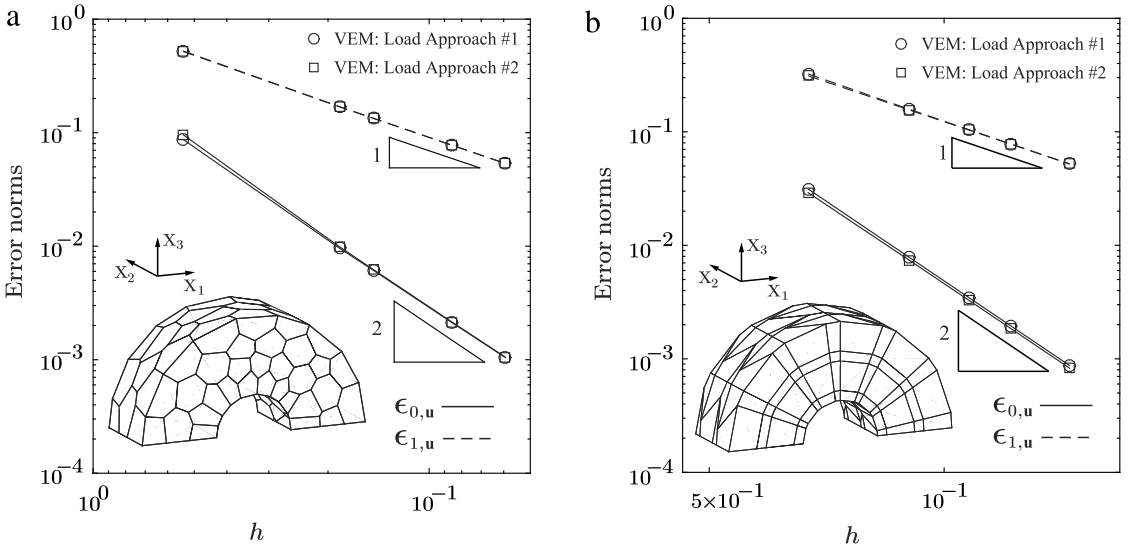

Fig. 10. The convergence plots of the error norms as functions of the average mesh size are shown in (a) for the CVT meshes and (b) for the distorted hexahedral meshes.

6.2. Mixed VEM

In this subsection, the performance of the mixed VEM is numerically evaluated. Throughout the subsection, the material is considered to be purely incompressible which is characterized by the following stored energy function [51]:

$$W(\mathbf{F}) = \begin{cases} \dfrac{3^{1-\alpha}}{2\alpha}\mu\left[(I_1(\mathbf{F}))^{\alpha} - 3^{\alpha}\right] & \text{if } \det\mathbf{F} = 1 \\ +\infty & \text{otherwise,} \end{cases} \tag{97}$$

with the initial shear modulus μ being 1 and the material parameter α being 3. For this material model, the trace-based stabilization gives

$$\alpha_E = \frac{3^{1-\alpha}\,(\alpha+1)\,\mu}{2} I_1^{\alpha-1} \text{ in 2D and } \alpha_E = \frac{(2\alpha+7)\,\mu}{3^{\alpha+1}} I_1^{\alpha-1} \text{ in 3D}, \tag{98}$$

both of which are nonlinear functions in $\mathbf{u}$.

We consider a similar boundary value problem in which an incompressible rectangular block of dimension $1\times1\times\pi$ is bent in to semi-circle shape. As depicted in Fig. 3(a), the rectangular block is defined by $-0.5 < X_1 < 0.5$, $-0.5 < X_2 < 0.5$ and $0 < X_3 < \pi$ in a Cartesian coordinate system (X_1, X_2, X_3), with both surfaces $X_1 = \pm 0.5$ being traction free. It is possible to obtain a closed-form solution for this problem [38]. In particular, the analytical displacement field takes the form [38]

$$u_x(\mathbf{X}) = -r(-0.5) + r(X_1)\cos(X_3) - 0.5 - X_1, \quad u_y(\mathbf{X}) = 0, \quad u_z(\mathbf{X}) = r(X_1)\sin(X_3) - X_3, \tag{99}$$

where the function $r(X_1)$ is given by

$$r(X_1) = \sqrt{2X_1 + \sqrt{2}}. \tag{100}$$

Additionally, one can obtain the analytical pressure field $\widehat{p}$ as

$$\widehat{p} = \frac{\left(22\sqrt{2}+25\right)\mu}{54} - \frac{\mu\left(r^2(X_1) + \frac{1}{r^2(X_1)} + 1\right)^3}{54} + \frac{\mu\left(r^2(X_1) + \frac{1}{r^2(X_1)} + 1\right)^2}{9r^2(X_1)}. \tag{101}$$

Unlike the problem in the preceding subsection, the body force $\mathbf{f}$ for this problem is $\mathbf{0}$. Again, this 3D problem can be simplified into a 2D plane strain problem, as illustrated in Fig. 3(b). In our following studies of both the 3D problem and its 2D simplification, in order to avoid the potential development of free surface instability (the performance of VEM on capturing the physical instability is beyond the scope of this paper and is a subject for future investigation), displacement is applied to all the surfaces except the surface $X_1 = 0.5$. Again, both 2D and 3D problems have identical $\mathcal{L}^2$ norms for the exact displacement, displacement gradient and pressure fields, which are obtained respectively as $\|\mathbf{u}\| = 3.4425$, $\|\nabla\mathbf{u}\| = 3.6736$ and $\|\widehat{p}\| = 2.7572$ analytically.

2D mixed VEM. We first consider the 2D mixed VEM and study its performance on the accuracy and convergence. We remind that the proposed approximation has been shown to lead to numerically stable schemes (in the linear regime) on several polygonal meshes in 2D, such as the CVT and structured hexagonal meshes [44,9,12]. The 2D plane strain problem shown in Fig. 3(b) is considered with the following sets of meshes: structured hexagonal, CVT, and non star-shaped "zoo" meshes made up of pegasus, bird and fish elements, as depicted in Fig. 4(a), (b) and (f) respectively. In Fig. 11 we plot the displacement and pressure error norms as functions of the average mesh sizes h for the VEM results using both "Robust" and "Simple" approaches to compute J_E. The results obtained form the mixed FEM with the gradient correction scheme for the CVT meshes and the structured hexagonal meshes are also included for comparison purposes. In addition, an example of the deformed shape of the "zoo" mesh is shown in Fig. 12. We remark that since the "zoo" meshes contain non star-shaped elements, it is difficult to perform mixed FEM analysis on them, however, the VEM analysis can be naturally conducted. Again, each data point in the plots for the CVT mesh is an average from five results. It is observed from the figures that mixed VEM using both "Robust" and "Simple" approaches to compute J_E delivers results that are optimally convergent in terms of both displacement and pressure errors. While the level of accuracy for the results obtained using the "Robust" and "Simple" approaches are almost identical with the CVT and structure hexagonal meshes, the results obtained using the former approach are slightly more accurate than the ones obtained by the latter approach with the non star-shaped "zoo" meshes, especially in terms of the $\mathcal{H}^1$-type norm of the displacement errors. This demonstrates the advantage of the "Robust" approach with respect to the "Simple" approach when dealing with highly irregular and non-convex meshes. Moreover, the comparison between the VEM and FEM results suggests that they have a similar level of accuracy. Again, the mixed VEM use only one integration point per element and thus is more computationally efficient than the mixed FEM.

3D mixed VEM. Our next step consists of performing numerical studies of the 3D mixed VEM with the original 3D problem shown in Fig. 3(a). We note that, differently from the 2D case [44], the inf–sup condition in the 3D case has

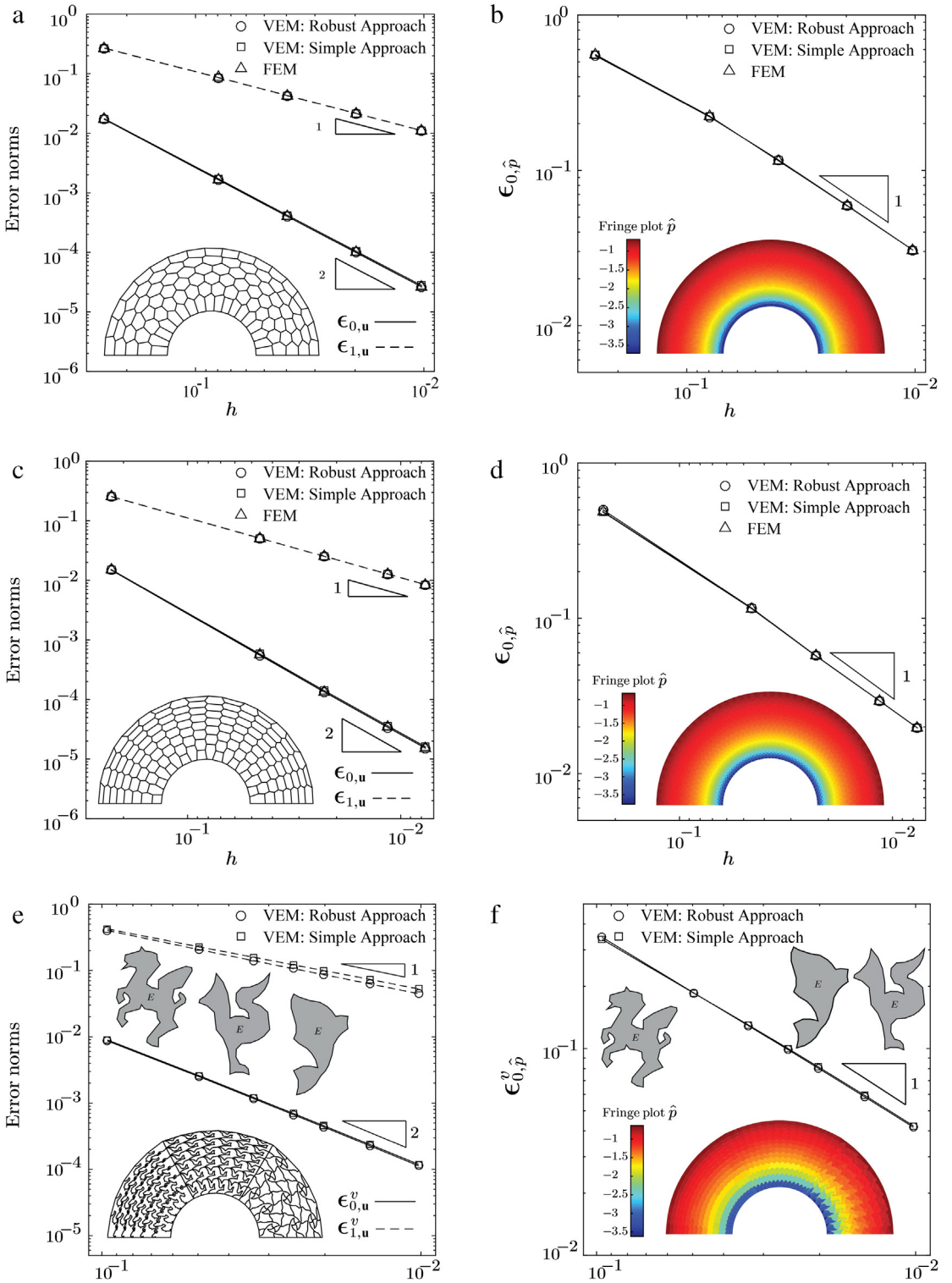

Fig. 11. The convergence plots of the error norms as functions of the average mesh size for (a) displacement errors and (b) the pressure error in the CVT meshes, (c) the displacement errors and (d) the pressure error in the structured hexagonal meshes, and (e) the displacement errors and (f) the pressure error in the non star-shaped "zoo" meshes.

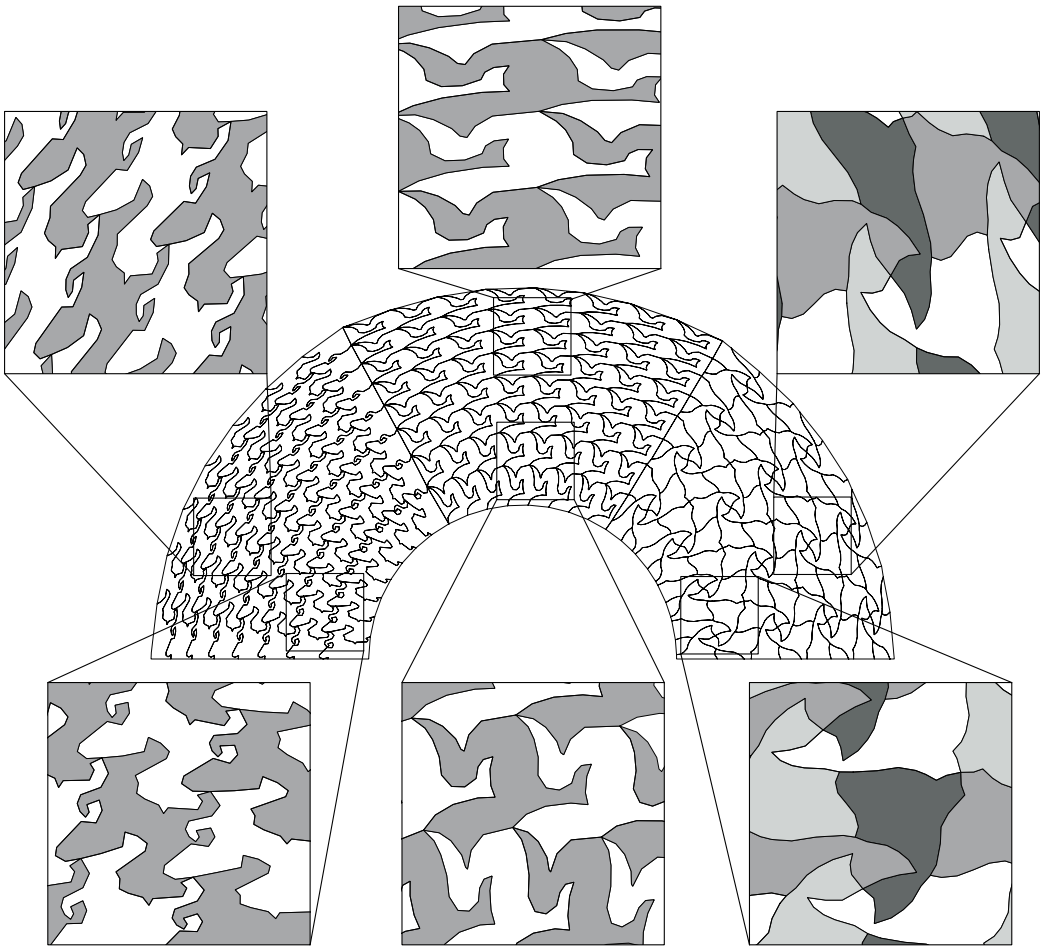

Fig. 12. The final deformed configuration is shown for the "zoo" mesh. The "zoo" mesh contains 224 elements with 64 pegasus, 72 bird, and 88 fish elements. This deformed shape is obtained by the mixed VEM.

not been proven, but it can be numerical investigated as has been done in the 2D (polygonal) FEM context [9,12]. Similarly to the displacement-based VEM case, CVT and distorted hexahedral meshes are considered, as shown in Fig. 2(e) and (f), respectively. Notice that both types of meshes only contain convex elements, hence it is possible to treat them using the standard FEM with the Wachspress shape functions [14]. On the other hand, we also consider two sets of concave meshes, the extruded octagonal meshes and the extruded version of the non star-shaped "zoo" meshes consist of pegasus, bird and fish elements, as shown in Fig. 13(a) and (b) respectively. We note that while all the elements in the extruded octagonal meshes satisfy the assumption in the definition of the 3D local VEM space, i.e., all the faces of each element are star convex with respect to $\mathbf{X}_s^f = 1/m^f \sum_{j=1}^{m^f} \mathbf{X}_j^f$, all the elements in the extruded "zoo" meshes contain non star-shaped faces, which violates this assumption. Figs. 14 and 15 show the displacement and pressure errors of the results obtained by the VEM with both the "Robust" and "Simple" approaches to compute J_E, together with illustrations of the deformed shapes and the fringe plots of the pressure field $\widehat{p}_h$. For the hexahedral meshes, VEM with both "Robust" and "Simple" approaches to compute J_E offers optimal convergence in the displacement errors. Yet, a slight degeneracy in the convergence of the pressure error occurs and their pressure fringe plots exhibit checkerboard modes. These indicate the occurrence of a mild numerical instability. For all the other meshes, optimal convergence in both displacement and pressure errors are observed for VEM with both approaches and the pressure fields are more smoothly distributed, suggesting numerical stability for those meshes. In particular, through the convergence observed in the results of the extruded "zoo" meshes, we highlight that our VEM

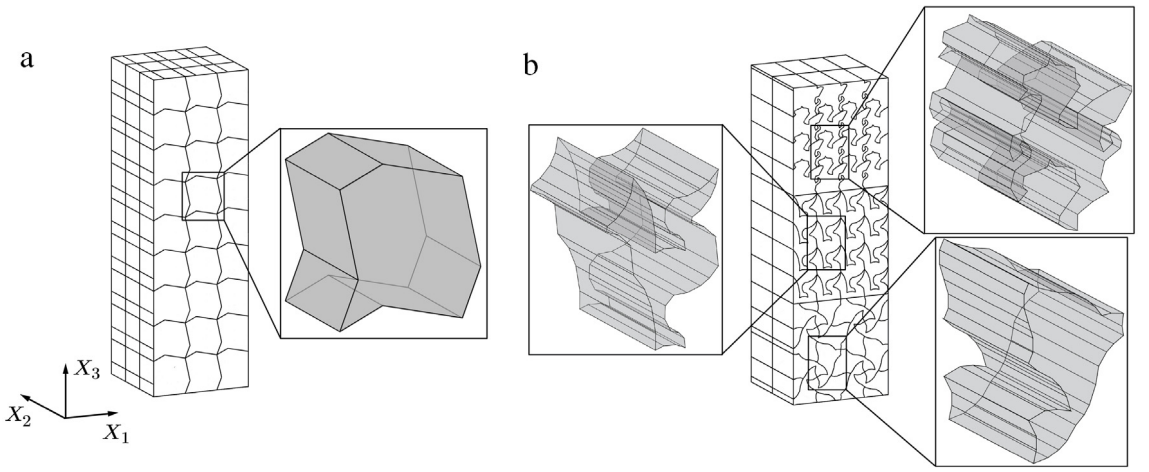

Fig. 13. Examples for (a) an extruded octagonal meshes with 81 elements and (b) a non star-shaped "zoo" meshes with 128 elements. This "zoo" mesh is made up of 32 extruded pegasus elements, 48 extruded bird elements, and 48 extruded fish elements.

formulation ensures convergence even though the meshes contain elements with non star-shaped faces (which violates our assumption in defining the local VEM space). Moreover, by comparing the results obtained from the "Robust" and "Simple" approaches to compute J_E, we remark that although both approaches appear to provide similarly accurate results for regular meshes (the hexahedral and CVT meshes), the "Robust" approach seems to produce more accurate results when the meshes become more irregular, e.g. the extruded "zoo" meshes.

7. Application example: Elastomer filled with rigid inclusions

In this section, we deploy the proposed VEM framework to the study of the nonlinear elastic response of an elastomer filled with an isotropic distribution of rigid circular particles in 2D. Through this application example, we aim to demonstrate the performance of the proposed displacement-based and mixed VEM formulations in problems which involve heterogeneous and large localized deformation fields. In the meantime, the influences of various choices of stabilization techniques and different approaches to compute J_E on the performance of the VEM in such problems are investigated.

We consider the filled elastomer to be a periodic repetition of a unit cell that contains a random distribution of a large number of particles constructed by means of a random sequential adsorption algorithm [52,53]. Motivated by the polydispersity in size of typical fillers, we consider a particular case with three families of particles with radii

$$\left\{r^{(1)}, r^{(2)}, r^3\right\} = \{r, 0.75r, 0.5r\} \quad \text{with} \quad r = \left(\frac{c^{(1)}}{N^{(1)}\pi}\right)^{(1/2)}, \text{ and} \tag{102}$$

concentrations

$$\left\{c^{(1)}, c^{(2)}, c^{(3)}\right\} = \{0.5c, 0.3c, 0, 2c\}, \tag{103}$$

where $N^{(1)}$ is the number of particles with the largest radius $r^{(1)}$, and c stands for the total are fraction of particles. In the present example, we take $N^{(1)} = 20$ and $c = 0.35$. A realization of such a unit cell containing a total number of 75 particles at area fraction $c = 35\%$ is shown in Fig. 16(a). Displacement periodic boundary conditions are applied, which implies

$$\begin{aligned} u_k(1, X_2) - u_k(0, X_2) &= \langle \mathbf{F} \rangle_{k1} - \delta_{k,1} \\ u_k(X_1, 1) - u_k(X_1, 0) &= \langle \mathbf{F} \rangle_{k2} - \delta_{k,2} \quad \forall k = 1, 2, \end{aligned} \tag{104}$$

where $\langle \mathbf{F} \rangle$ and $\delta_{k,l}$ are the macroscopic deformation gradient and Kronecker delta, respectively. The symbol u_k and X_k $(k = 1, 2)$ denote the components of the displacement field and initial position vector in a Cartesian frame of reference with its origin placed at the left lower corner of the unit cell.

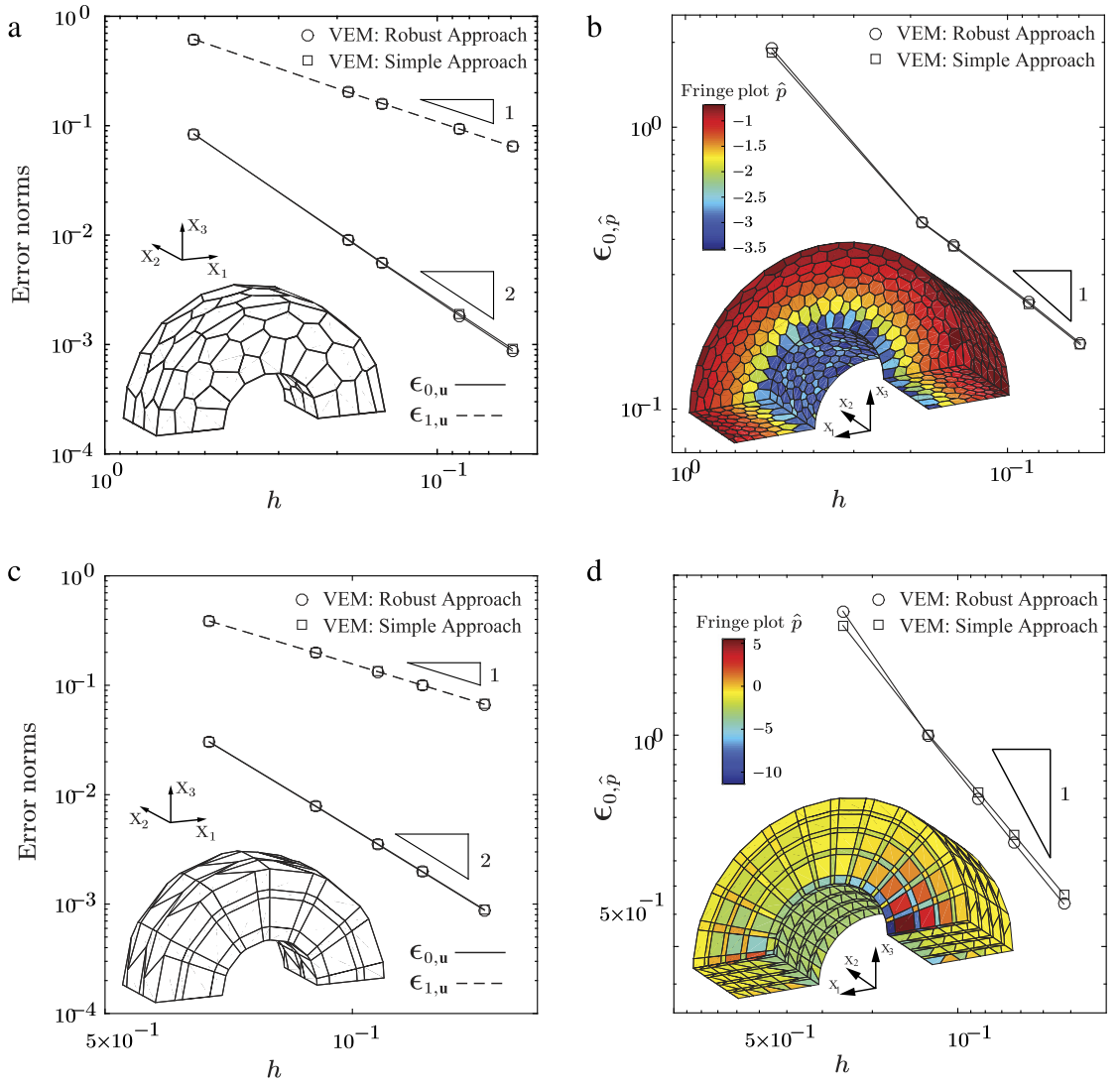

Fig. 14. The convergence plots of the error norms as functions of the average mesh size for (a) the displacement errors and (b) the pressure error in the CVT meshes, (c) the displacement errors and (d) the pressure error in the hexahedral meshes.

Throughout this section, we make use of a CVT mesh as depicted in Fig. 16, which is generated by "PolyMesher" [48]. The discretization contains a total of 20,000 elements and 40,196 nodes. To apply periodic displacement boundary conditions to this CVT mesh, we adopt the concept introduced in [12] of locally inserting additional nodes to achieve periodic nodal distributions on opposite boundaries of the mesh (a procedure that can be easily applied thanks to the flexibility of polygonal meshes). On the other hand, each particle in the CVT mesh is considered to be infinitely rigid by adopting the variational formulation proposed by Chi et al. [54], in which its presence is treated as a set of kinematic constraints on the displacement DOFs.

In the subsequent VEM and polygonal FEM simulations on the CVT mesh, the macroscopic deformation gradient is evaluated as

$$\langle \mathbf{F} \rangle \doteq \frac{\sum_E |E| \left(\mathbf{I} + \Pi_E^0 \nabla \mathbf{u}_h \right)}{|\Omega_h|}. \tag{105}$$

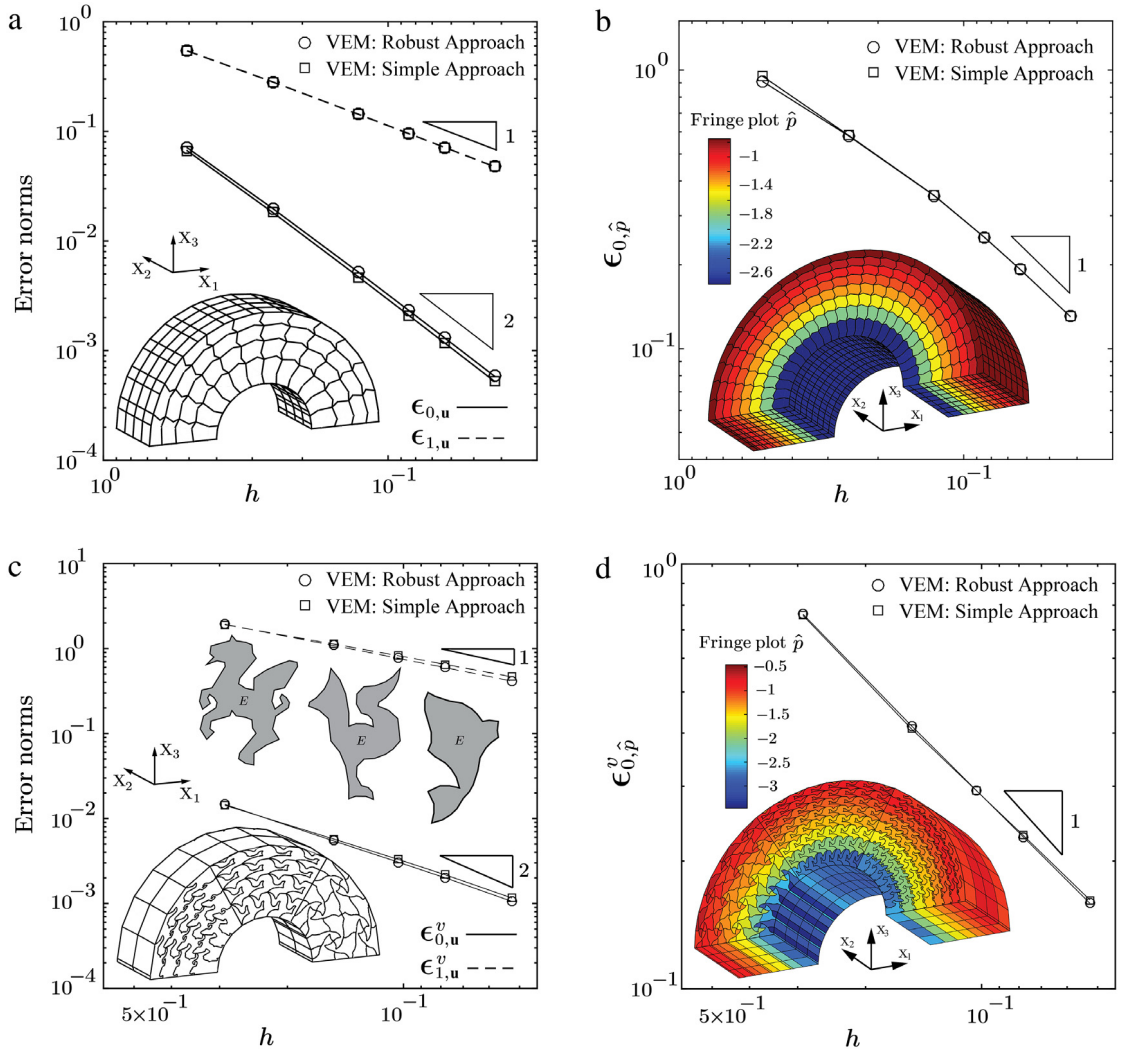

Fig. 15. The convergence plots of the error norms as functions of the average mesh size for (a) the displacement errors and (b) the pressure error in the extruded octagonal meshes, (c) the displacement errors and (d) the pressure error in the extruded "zoo" meshes.

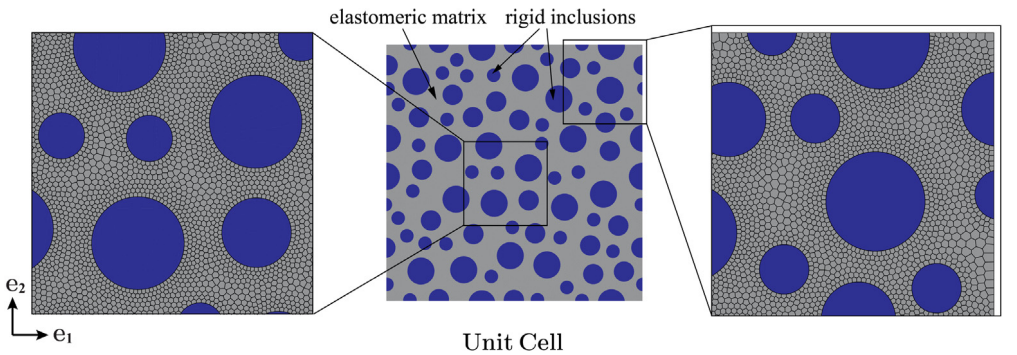

Fig. 16. Illustrations of the unit cell, which consists of 75 polydispersed particles at a total area fraction of $c = 35\%$, and the details of the CVT mesh, which consists of 20,000 elements and 40,196 nodes.

Table 3
VEM stability parameter $\alpha_E(\mathbf{s}_h)$.

Operator	Norm: Eq. (59)		Trace: Eq. (60)	
$\mathbf{s}_h$	$\mathbf{0}$	$\mathbf{u}_h^{n-1}$	$\mathbf{u}_h^{n-1}$	$\mathbf{u}_h$

In addition, to quantitatively evaluate the performance of those simulations, we define the macroscopic energy of the filled elastomer in the following manner

$$\langle W \rangle \doteq \frac{1}{|\Omega_h|} \sum_E |E| \left[\Psi \left(\mathbf{I} + \Pi_E^0 \nabla \mathbf{u}_h \right) + U \left(J_E(\mathbf{u}_h) \right) \right], \tag{106}$$

where J_E is evaluated using the "Robust" approach with expression (33). When the matrix is purely incompressible, the second term in the above expression is simply zero for all the elements in the mesh. We also monitor the relation between the macroscopic deformation gradient $\langle \mathbf{F} \rangle$ and macroscopic first Piola–Kirchoff stress $\langle \mathbf{P} \rangle$ in the VEM and polygonal FEM simulations by equivalently monitoring the displacement–traction relationship at the lower-right corner of the unit cell (the location where we apply displacement in our simulations).

7.1. Filled elastomers with neo-Hookean matrix

In this subsection, the matrix is assumed to be compressible neo-Hookean material, which is described by the stored-energy function

$$W(\mathbf{F}) = \frac{\mu}{2} \left(\overline{\mathbf{F}} : \overline{\mathbf{F}} - 3 \right) + \frac{\kappa}{2} \left(\det \mathbf{F} - 1 \right)^2, \tag{107}$$

where μ and κ are the initial shear and bulk moduli. Throughout this subsection, the initial shear modulus is taken to be $\mu = 1$, and the filled elastomer is assumed to be subjected to uniaxial tension, whose macroscopic deformation $\langle \mathbf{F} \rangle$ gradient has the form $\langle \mathbf{F} \rangle = \lambda_1 \mathbf{e}_1 \otimes \mathbf{e}_1 + \lambda_2 \mathbf{e}_2 \otimes \mathbf{e}_2$ where λ_1 and λ_2 are the macroscopic stretches with λ_1 in the tensile direction.

We first study the influence of various choices of the stability parameter $\alpha_E(\mathbf{s}_h)$ on the performance of the displacement-based VEM. More specifically, we investigate the four choices of $\alpha_E(\mathbf{s}_h)$ as shown in Table 3. We assume two values of the initial bulk moduli, $\kappa = 10$ and $\kappa = 1000$, which represent compressible and nearly incompressible materials respectively. For all the cases, the target macroscopic stretch λ_1 is set as 2.

As a qualitative comparison, Fig. 17(a)–(b) depict the detailed views of the unit cell at the same applied macroscopic stretches using different choices of $\alpha_E(\mathbf{s}_h)$ in Table 3. These detailed views are taken from the deformed configurations at $\lambda_1 = 1.74$ for $\kappa = 10$ and from those at $\lambda_1 = 1.42$ for $\kappa = 1000$. As a reference, the detailed views obtained from the standard displacement-based and mixed FEM are also included. Additionally, Fig. 18(a)–(d) show the comparison of macroscopic responses (energy and relevant component of stress) as functions of the applied stretch λ_1 between the various choices of $\alpha_E(\mathbf{s}_h)$, with the ones obtained by the displacement-based FEM represented by the dashed lines.

Several immediate observations can be made. First, the displacement-based FEM apparently suffers from volumetric locking when the matrix becomes nearly incompressible, i.e. $\kappa = 1000$, as it produces over stiff macroscopic energy and stress. On the other hand, the proposed displacement-based VEM formulation appears free of volumetric locking and produces more reasonable macroscopic energy and stress. The displacement-based VEM with all the stabilization choices predicts almost identical macroscopic energies, although we note that the norm-based stabilization with $\mathbf{s}_h = \mathbf{u}_h^{n-1}$ and trace-based stabilization with $\mathbf{s}_h = \mathbf{u}_h$ produce a slightly stiffer macroscopic stress than the other two. Moreover, the detailed views in Fig. 17 indicate that the norm-based stabilization with $\mathbf{s}_h = \mathbf{0}$ leads to hourglass modes in the element at high deformation levels (the elements that are plotted in red). As we have discussed in Section 4, this is a consequence of the under-stabilizations of $\alpha_E(\mathbf{0})$ in those elements. The detailed views of other choices, on the other hand, do not contain hourglass modes in those elements and all are qualitatively similar to the one obtained with the mixed FEM.

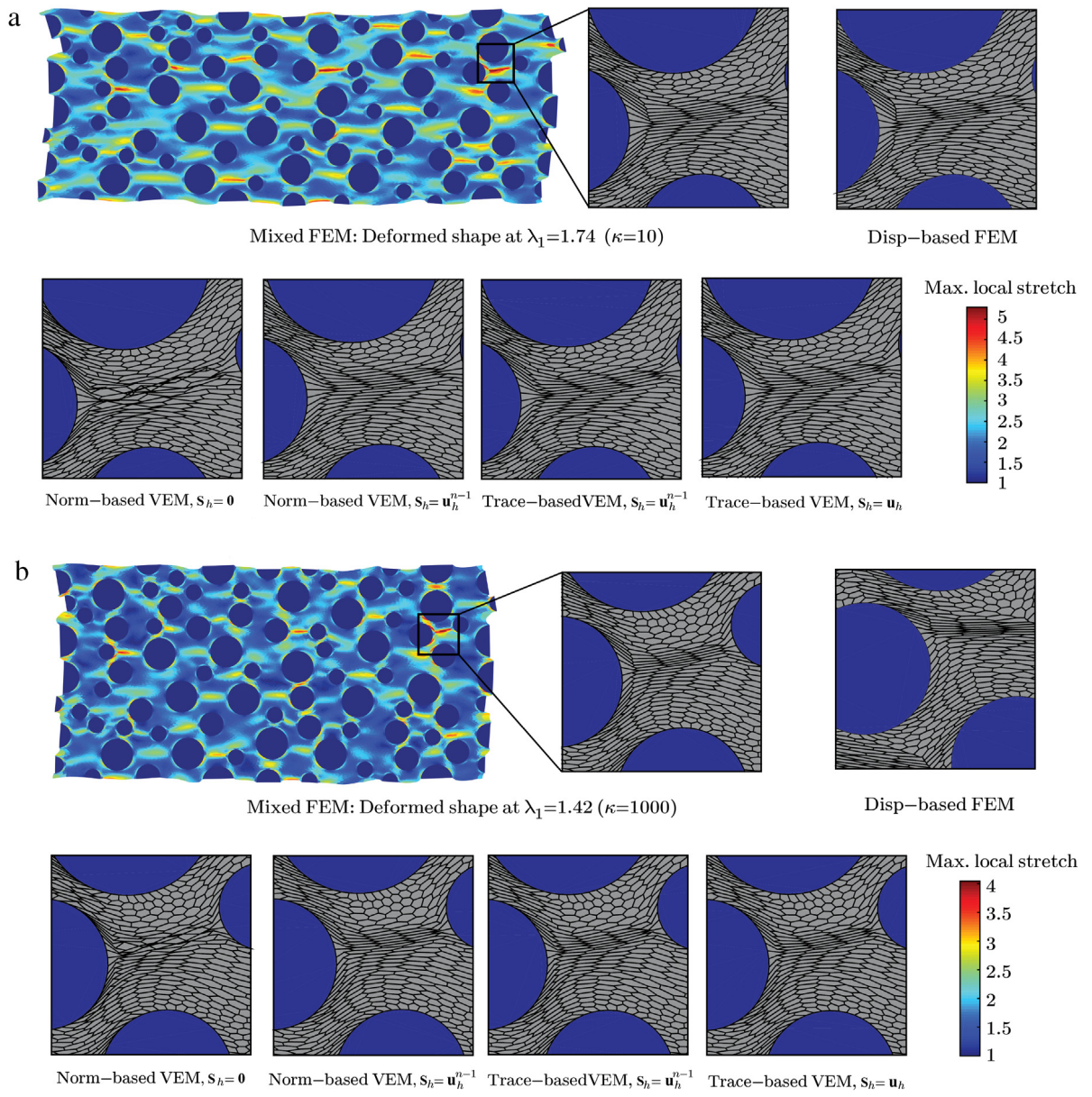

Fig. 17. Detailed views of the unit cell at the same applied macroscopic stretches obtained using the displacement-based and mixed FEM, and the displacement-based VEM using different choices of $\alpha_E(\mathbf{s}_h)$ in Table 3: (a) the case of $\kappa = 10$ at $\lambda_1 = 1.74$ and (b) the case of $\kappa = 1000$ at $\lambda_1 = 1.42$. (For interpretation of the references to color in this figure legend, the reader is referred to the web version of this article.)

Another major interest is the ability of the VEM to model large localized and heterogeneous deformations. To that end, we quantify the maximum global stretch λ_1 that the displacement-based VEM (with each stabilization choice) can achieve before non-converge occurs in the Newton–Raphson process; in general, the larger global stretch the unit cell reaches, the larger localized deformation it induces. Based on this measure, it is apparent that the norm-based stabilization with $\mathbf{s}_h = \mathbf{0}$ is the worst choice for both cases of $\kappa = 10$ and $\kappa = 1000$. With this choice, the unit cell reaches significantly less maximum global stretch than the other choices. The same happens with the displacement-based FEM due to the volumetric locking. On the other hand, as the incompressibility level of the matrix increases from $\kappa = 10$ to $\kappa = 1000$, we notice the advantage of using the trace-based stabilization for VEM, as well as choosing $\mathbf{s}_h = \mathbf{u}_h$ over $\mathbf{s}_h = \mathbf{u}_h^{n-1}$, in achieving larger global stretches. We note that since the displacement-based

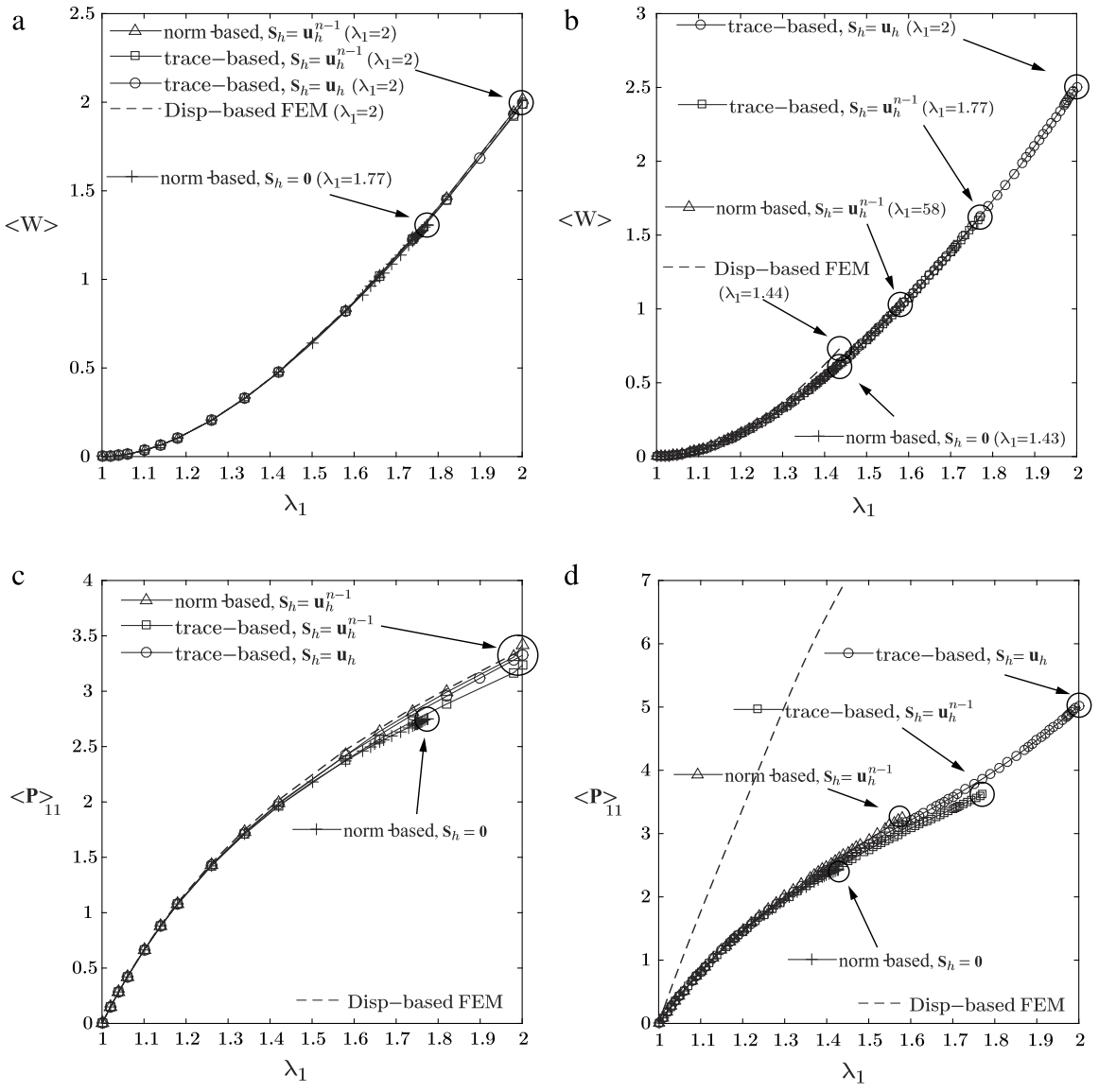

Fig. 18. Comparison of the macroscopic responses obtained by the displacement-based VEM with various stabilization techniques: (a) Macroscopic energy as a function of the applied stretch λ_1 for the case of $\kappa = 10$. (b) Macroscopic energy as a function of the applied stretch λ_1 for the case of $\kappa = 1000$. (c) Macroscopic stress as a function of the applied stretch λ_1 for the case of $\kappa = 10$. (d) Macroscopic stress as a function of the applied stretch λ_1 for the case of $\kappa = 1000$.

VEM is equivalent to the mixed VEM as discussed in Section 4, the above observations and discussions also apply to the mixed VEM formulation.

Our second study investigates the performance of the mixed VEM using different approaches to compute J_E. Both the "Robust" approach (i.e. Eqs. (36) and (38)) and the "Simple" approach (i.e. Eqs. (46)–(48)) are considered. Similarly to the preceding study, we choose two values of initial bulk moduli, $\kappa = 10$ and $\kappa = \infty$, representing compressible and purely incompressible matrices. In this study, we utilize the trace-based stabilization with $\mathbf{s}_h = \mathbf{u}_h$ and the target global stretch is set as $\lambda_1 = 2$.

We plot in Fig. 19(a)–(d) the macroscopic responses (macroscopic energy and relevant component of stress) as functions of the applied stretch λ_1 for the cases of $\kappa = 10$ and $\kappa = \infty$. It is noted from those figures that although the two approaches yield similar macroscopic responses, using the exact expression for J_E (the "Robust" approach) helps

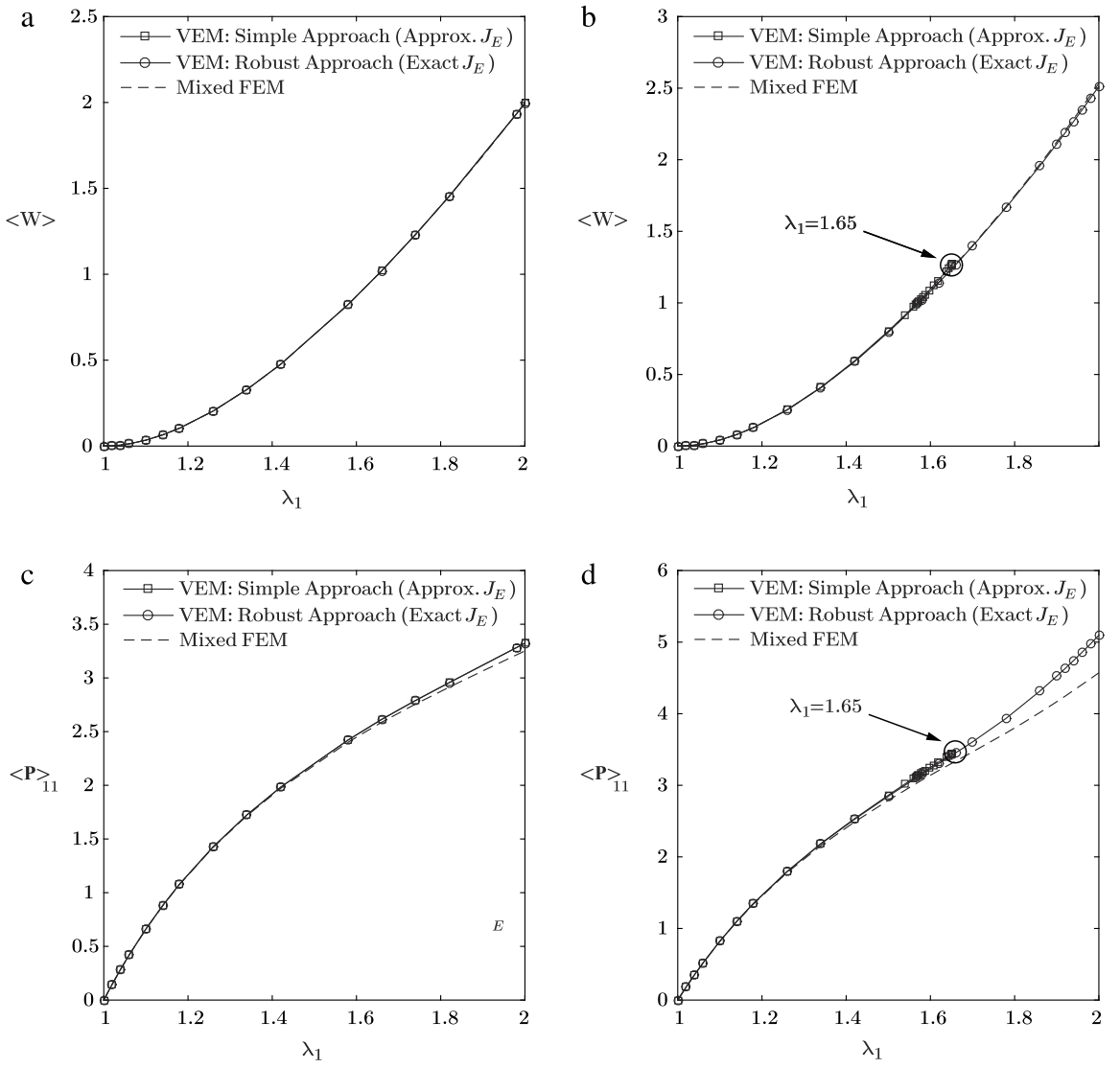

Fig. 19. Comparison of the macroscopic responses obtained by the mixed VEM with the two approaches to compute J_E: (a) Macroscopic energy as a function of the applied stretch λ_1 for the case of $\kappa = 10$. (b) Macroscopic energy as a function of the applied stretch λ_1 for the case of $\kappa = \infty$. (c) Macroscopic stress as a function of the applied stretch λ_1 for the case of $\kappa = 10$. (d) Macroscopic stress as a function of the applied stretch λ_1 for the case of $\kappa = \infty$.

the unit cell to reach a significantly larger global stretch than using the approximation of J_E (the "Simple" approach) when the material is nearly or purely incompressible.

We conclude from the above studies that the trace-based stabilizations generally yield more accurate macroscopic responses than the norm-based ones (when compared with the results obtained from the mixed FEM). Moreover, choosing $\mathbf{s}_h = \mathbf{u}_h$ instead of $\mathbf{s}_h = \mathbf{u}_h^{n-1}$ (although it seems to produce slightly stiffer macroscopic stress), as well as using the "Robust" approach to compute J_E, is more computationally demanding but typically helps the unit cell reach larger global stretches, especially as the matrix is approaching the incompressible limit. Consequently, for the remainder of this Section, the trace-based stabilization with $\mathbf{s}_h = \mathbf{u}_h$ and the "Robust" approach to compute J_E are adopted. We finally remark that, for such problems, linear and quadratic triangular and quadrilateral (conforming) elements are found to lead to a loss of convergence at much smaller global stretches when compared to the polygonal methods studied above, especially when the matrix phase is nearly or purely incompressible (see, e.g., Section 5.1 of [13]).

7.2. Filled elastomer with matrix described by other constitutive models

In the sequel, we adopt the mixed VEM formulation to study the nonlinear elastic responses of the filled elastomer when its matrix is characterized by other material models. The main purpose of this study is to thoroughly compare the performance of the mixed VEM with the mixed FEM for various material models. In particular, we consider the incompressible Mooney–Rivlin model

$$W(\mathbf{F}) = \begin{cases} C_1\left[I_1(\mathbf{F}) - 3\right] + C_2\left[I_2(\mathbf{F}) - 3\right] & \text{if } \det\mathbf{F} = 1 \\ +\infty & \text{otherwise,} \end{cases} \tag{108}$$

and the incompressible model utilized in [53,55] to describe a typical silicone rubber

$$W(\mathbf{F}) = \begin{cases} \dfrac{3^{1-\alpha_1}}{2\alpha_1}\mu_1\left[(I_1(\mathbf{F}))^{\alpha_1} - 3^{\alpha_1}\right] + \dfrac{3^{1-\alpha_2}}{2\alpha_2}\mu_2\left[(I_1(\mathbf{F}))^{\alpha_2} - 3^{\alpha_2}\right] & \text{if } \det\mathbf{F} = 1 \\ +\infty & \text{otherwise.} \end{cases} \tag{109}$$

In the Mooney–Rivlin model, we choose the material parameters to be $C_1 = 0.3$ and $C_2 = 0.2$, resulting in an initial shear modulus $\mu = 2(C_1 + C_2) = 1$. The material parameters for the typical silicone rubber are taken to be $\alpha_1 = 3.837$, $\alpha_2 = 0.559$, $\mu_1 = 0.032$ and $\mu_2 = 0.3$ with the initial shear modulus being $\mu = \mu_1 + \mu_2 = 0.332$. Two loading conditions are considered: (i) uniaxial tension whose macroscopic deformation gradient $\langle\mathbf{F}\rangle$ is of the form $\langle\mathbf{F}\rangle = \lambda\mathbf{e}_1 \otimes \mathbf{e}_1 + \lambda^{-1}\mathbf{e}_2 \otimes \mathbf{e}_2$ and (ii) simple shear whose macroscopic deformation gradient $\langle\mathbf{F}\rangle$ is of the form $\langle\mathbf{F}\rangle = \mathbf{I} + \gamma\mathbf{e}_1 \otimes \mathbf{e}_2$, where λ and γ are the applied global stretch and shear.

Under both loading conditions, Fig. 20 depicts the final deformed configurations of the unit cells with Mooney–Rivlin matrix obtained by the mixed VEM and mixed FEM at their respective maximum global deformation states. Similarly, Fig. 21 shows the deformed configurations of the unit cell with typical silicone rubber matrix obtained by the mixed VEM and mixed FEM at their respective maximum global deformation states. The color scale in each configuration corresponds to the maximum principal stretch of each element, with those having a value of 5 and above plotted red. Additionally, the macroscopic responses predicted by the VEM and FEM (macroscopic energies and relevant components of macroscopic stress) as functions of the applied stretch λ or shear γ are shown in Figs. 22 and 23, respectively for unit cells with Mooney–Rivlin matrix and typical silicone rubber matrix. In the plots, we also show the deformed configurations of the unit cell at the same levels of global deformations obtained by VEM and FEM, with the elements whose maximum principal stretches greater than 5 plotted read.

Several observations can be made from Figs. 20–23. First, for both material models considered, the results obtained from the mixed VEM and mixed FEM are in good qualitative and quantitative agreements. As shown in Figs. 22 and 23, the deformed configurations obtained by the VEM and FEM share similar patterns at the same global deformations levels. The macroscopic responses predicted by the VEM and FEM also match reasonably well, especially for the macroscopic energy. However, it is worthwhile noting that, similarly to the case of neo-Hookean matrix presented in the previous subsection, we also observe stiffer responses in the macroscopic stresses obtained by VEM than the ones by FEM for the unit cell with Mooney–Rivlin matrix. Furthermore, by comparing the maximum deformation levels reached by the unit cells modeled respectively by the VEM and FEM, it appears that the VEM and FEM have similar capabilities of modeling large localized deformations. As further investigation, we summarize in Table 4 the maximum global stretch/shear reached by the VEM and FEM for both material models and the corresponding maximum local principal stretches. It is interesting to note that for the unit cell with Mooney–Rivlin matrix, although the VEM yields a larger global stretch in uniaxial tension, the corresponding maximum local principal stretches in the FEM mesh are higher. We again underline that, on this same test, standard triangular and quadrilateral FEM would reach a much smaller global stretch when compared to the polygonal methods under study [12,13].

8. Concluding remarks

This paper introduces a VEM framework for two and three dimensional finite elasticity problems. Two VEM formulations are presented, which adopt a displacement-based and a two-field mixed variational principles respectively. The displacement-based VEM formulation appears to be free of volumetric locking as the material becomes nearly incompressible, at least for the proposed set of meshes. By construction, the proposed VEM formulations are able to

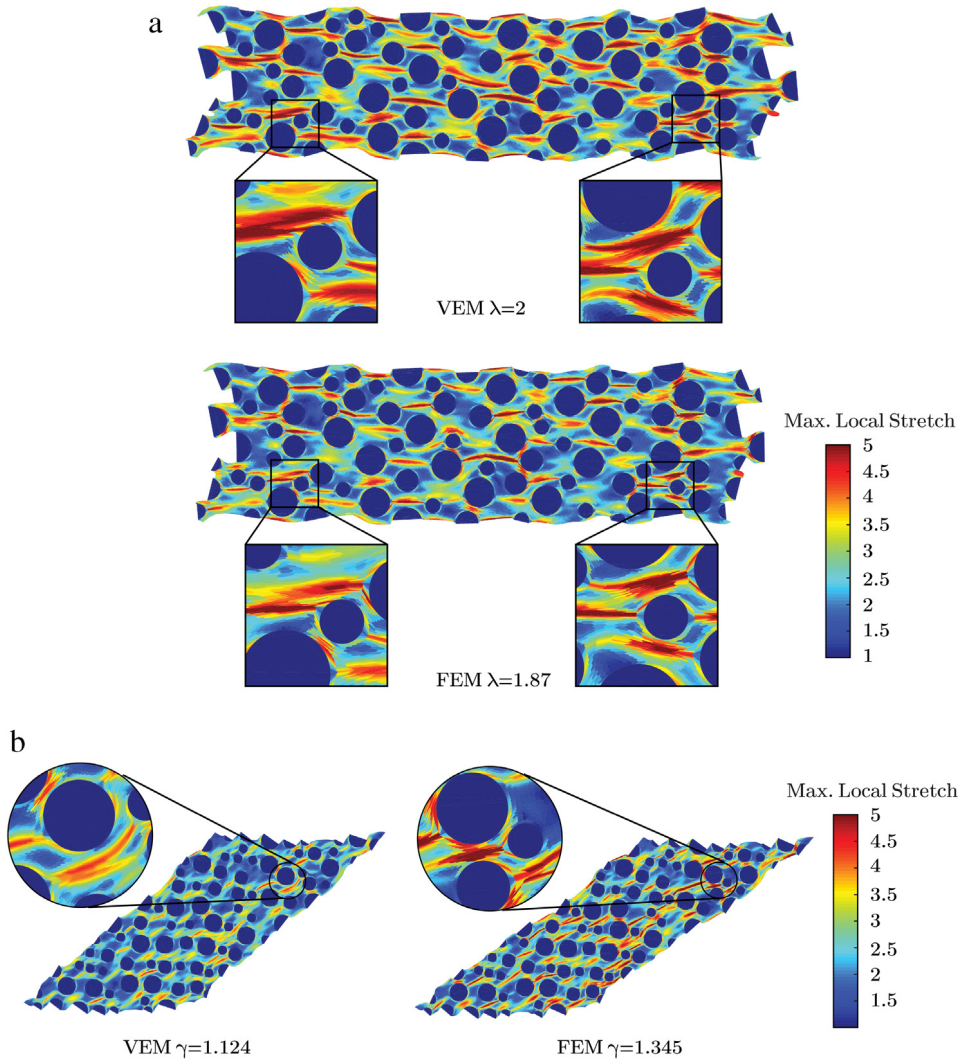

Fig. 20. The maximum deformed configurations of the unit cell obtained by the mixed VEM and mixed FEM for the Mooney–Rivlin matrix under (a) uniaxial tension and (b) simple shear.

Table 4
Summary of maximum principal stretches among all the elements in the mesh for the unit cell considering different material models and loading conditions.

		Mooney–Rivlin matrix		Typical silicone rubber matrix	
		Uniaxial tension	Simple shear	Uniaxial tension	Simple shear
Max. global stretch/shear	VEM	2	1.124	1.660	1.073
	FEM	1.870	1.345	1.716	1.077
Max. principal stretch	VEM	6.559	4.650	3.943	3.737
	FEM	7.015	8.022	4.384	3.903

efficiently handle a more general class of polygonal and polyhedral meshes than the standard FEM, including the ones with non-convex elements. Several numerical studies are presented, which confirm the convergence and accuracy of the VEM formulations. In particular, for three-dimensional problems, our numerical studies have further shown that the VEM formulations appear to produce convergent results even for meshes containing non-star shaped elements,

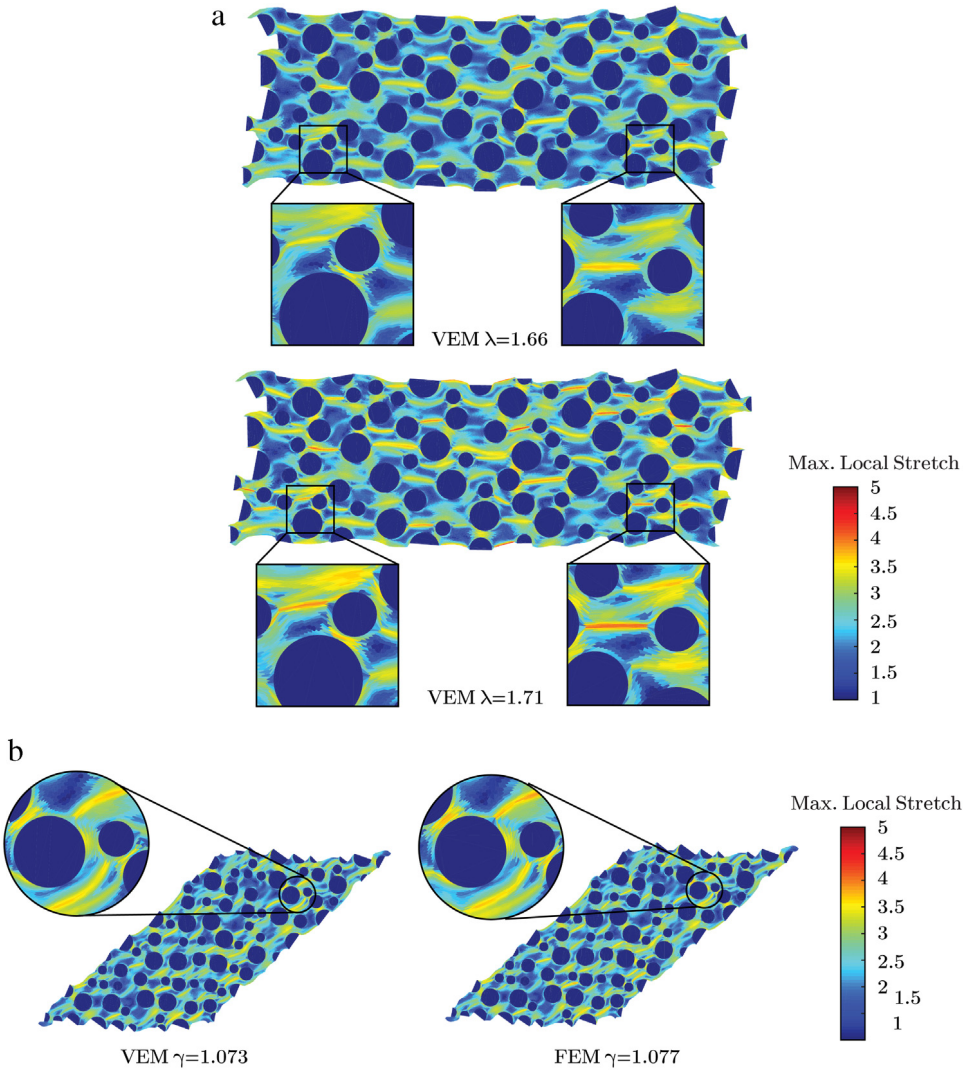

Fig. 21. The maximum deformed configurations of the unit cell obtained by the mixed VEM and mixed FEM for the typical silicone rubber matrix under (a) uniaxial tension and (b) simple shear. (For interpretation of the references to color in this figure legend, the reader is referred to the web version of this article.)

which makes the VEM formulation even more forgiving with respect to the quality of the mesh. We also show that, according to the definition of VEM spaces, closed-form expressions for the exact average volume changes over each polygonal/polyhedral elements can be derived. Those closed-form expressions render the VEM more accurate and robust, especially for irregular meshes, such as those containing elements with non star-shaped faces and in problems that involve large heterogeneous and localized deformations. Furthermore, different constructions of the loading terms are discussed and various stabilization strategies are studied, which are shown to have significant influence on the performance of the VEM formulations in finite elasticity problems, especially those involving large localized and heterogeneous deformations fields. A stabilization scheme is further proposed in this work for isotropic materials, which is based on the trace of the material tangent modulus tensor. We deploy the proposed VEM formulations to the study of nonlinear elastic response of a filled elastomer in 2D and demonstrate that they are able to capture large localized deformation fields in such problems.

The aforementioned work indicates that the VEM offers room for novel developments in nonlinear mechanics. We remark that several extensions are of interest, for instance, studies of the performance of VEM in capturing physical instabilities and development of more advanced stabilization schemes for finite elasticity problems.

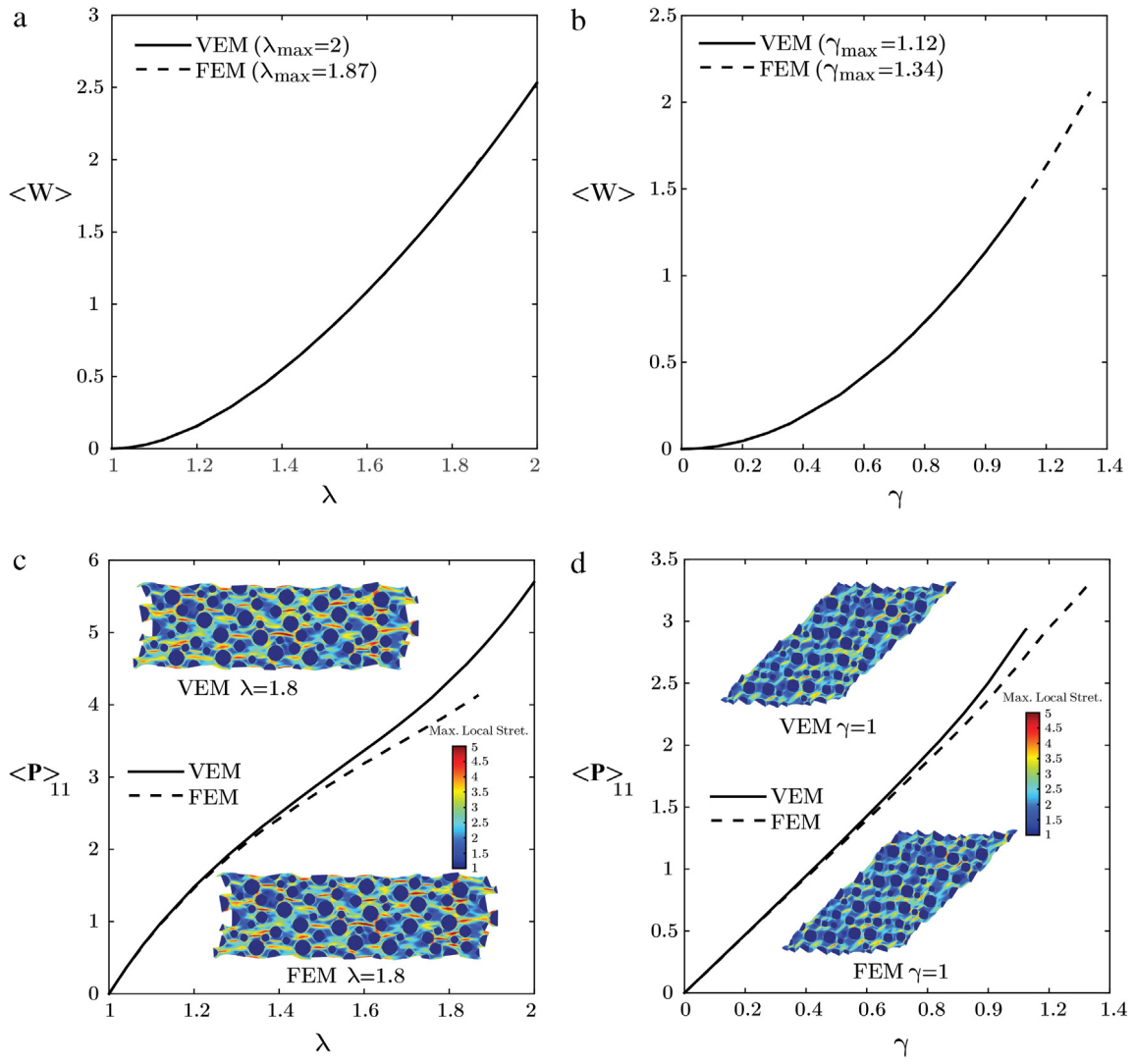

Fig. 22. Comparison of the macroscopic responses obtained by the mixed VEM and mixed FEM for Mooney–Rivlin matrix: (a) macroscopic energy as a function of the applied stretch λ under uniaxial tension; (b) macroscopic energy as a function of the applied shear γ under simple shear; (c) macroscopic stress as a function of the applied stretch λ under uniaxial tension; (d) macroscopic stress as a function of the applied shear γ under simple shear.

Acknowledgments

HC and GHP acknowledge support from the US National Science Foundation (NSF) under Grant CMMI #1624232 (formerly #1437535). LBV was partially supported by the European Research Council (ERC) under the European Unions Horizon 2020 research and innovation programme (Grant Agreement No. 681162). This support is gratefully acknowledged. The information presented in this paper is the sole opinion of the authors and does not necessarily reflect the views of the sponsoring agencies.

Appendix A. Trace-based stabilization parameter α_E for isotropic solids

We present a detailed derivation of the trace-based stabilization parameter α_E in (62) and (63). Considering a general function $\Phi(I_1, I_2, J)$, we have α_E be expanded as

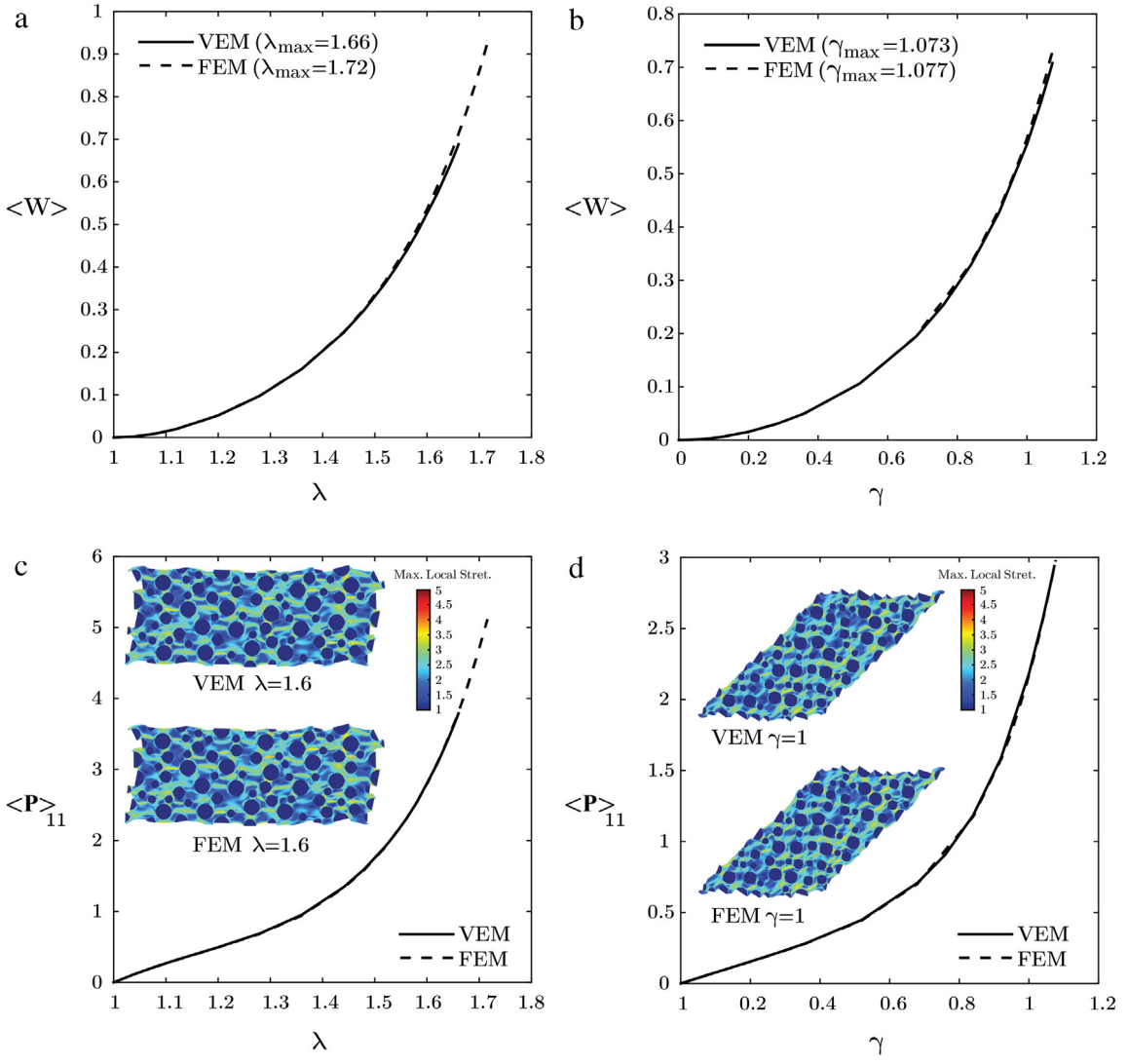

Fig. 23. Comparison of the macroscopic responses obtained by the mixed VEM and mixed FEM for typical silicone rubber matrix: (a) macroscopic energy as a function of the applied stretch λ under uniaxial tension; (b) macroscopic energy as a function of the applied shear γ under simple shear; (c) macroscopic stress as a function of the applied stretch λ under uniaxial tension; (d) macroscopic stress as a function of the applied shear γ under simple shear.

$$\begin{aligned}\alpha_E = \frac{1}{d^2}\mathrm{tr}\left(\frac{\partial^2\Phi}{\partial\mathbf{F}\partial\mathbf{F}}\right) = \frac{1}{d^2}\mathrm{tr}\Bigg[&\frac{\partial^2\Phi}{\partial I_1\partial I_1}\frac{\partial I_1}{\partial\mathbf{F}}:\frac{\partial I_1}{\partial\mathbf{F}} + \frac{\partial^2\Phi}{\partial I_2\partial I_2}\frac{\partial I_2}{\partial\mathbf{F}}:\frac{\partial I_2}{\partial\mathbf{F}} + \frac{\partial^2\Phi}{\partial J\partial J}\frac{\partial J}{\partial\mathbf{F}}:\frac{\partial J}{\partial\mathbf{F}} + 2\frac{\partial^2\Phi}{\partial I_1\partial I_2}\frac{\partial I_1}{\partial\mathbf{F}}:\frac{\partial I_2}{\partial\mathbf{F}}\\ &+2\frac{\partial^2\Phi}{\partial I_1\partial J}\frac{\partial I_1}{\partial\mathbf{F}}:\frac{\partial J}{\partial\mathbf{F}} + 2\frac{\partial^2\Phi}{\partial I_2\partial J}\frac{\partial I_2}{\partial\mathbf{F}}:\frac{\partial J}{\partial\mathbf{F}} + \frac{\partial\Phi}{\partial I_1}\mathrm{tr}\left(\frac{\partial^2 I_1}{\partial\mathbf{F}\partial\mathbf{F}}\right)\\ &+\frac{\partial\Phi}{\partial I_2}\mathrm{tr}\left(\frac{\partial^2 I_2}{\partial\mathbf{F}\partial\mathbf{F}}\right) + \frac{\partial\Phi}{\partial J}\mathrm{tr}\left(\frac{\partial^2 J}{\partial\mathbf{F}\partial\mathbf{F}}\right)\Bigg],\end{aligned} \tag{110}$$

where the dependences of α_E, Φ and its derivatives on I_1, I_2 and J are assumed. In the above equation, each component can be explicitly expressed as

$$\frac{\partial I_1}{\partial\mathbf{F}}:\frac{\partial I_1}{\partial\mathbf{F}} = 4I_1, \quad \frac{\partial I_2}{\partial\mathbf{F}}:\frac{\partial I_2}{\partial\mathbf{F}} = 4\left[2I_1I_2 - I_1\mathrm{tr}\left(\mathbf{C}^2\right) + \mathrm{tr}\left(\mathbf{C}^3\right)\right], \quad \frac{\partial J}{\partial\mathbf{F}}:\frac{\partial J}{\partial\mathbf{F}} = J^2\mathrm{tr}\left(\mathbf{C}^{-1}\right).$$

$$\frac{\partial I_1}{\partial \mathbf{F}} : \frac{\partial I_2}{\partial \mathbf{F}} = 4\left[I_1^2 - \mathrm{tr}\left(\mathbf{C}^2\right)\right] = 8I_2, \quad \frac{\partial I_1}{\partial \mathbf{F}} : \frac{\partial J}{\partial \mathbf{F}} = 4dJ, \quad \frac{\partial I_2}{\partial \mathbf{F}} : \frac{\partial J}{\partial \mathbf{F}} = 2\left(d-1\right) J I_1,$$
$$\mathrm{tr}\left(\frac{\partial^2 I_1}{\partial \mathbf{F}\partial \mathbf{F}}\right) = 2d^2, \quad \mathrm{tr}\left(\frac{\partial^2 I_2}{\partial \mathbf{F}\partial \mathbf{F}}\right) = 2\left(d-1\right)^2 I_1, \quad \mathrm{tr}\left(\frac{\partial^2 J}{\partial \mathbf{F}\partial \mathbf{F}}\right) = 0. \tag{111}$$

In the steps that follow, the Cayley–Hamilton theorem (see, for example, [56]) is adopted to further simplify the following two terms

$$\frac{\partial I_2}{\partial \mathbf{F}} : \frac{\partial I_2}{\partial \mathbf{F}} = 4\left[2I_1 I_2 - I_1 \mathrm{tr}\left(\mathbf{C}^2\right) + \mathrm{tr}\left(\mathbf{C}^3\right)\right], \text{ and } \frac{\partial J}{\partial \mathbf{F}} : \frac{\partial J}{\partial \mathbf{F}} = J^2 \mathrm{tr}\left(\mathbf{C}^{-1}\right). \tag{112}$$

In 2D, the Cayley–Hamilton theorem [56] states that $\mathbf{C} \in \mathbb{R}^{2\times 2}$ satisfies the following characteristic equation

$$\mathbf{C}^2 - I_1 \mathbf{C} + \det(\mathbf{C})\mathbf{I} = \mathbf{0}. \tag{113}$$

The following relation can be extracted from the above characteristic equation:

$$\mathrm{tr}\left(\mathbf{C}^3\right) - I_1 \mathrm{tr}\left(\mathbf{C}^2\right) = J^2 I_1 \text{ and } J^2 \mathrm{tr}\left(\mathbf{C}^{-1}\right) = I_1, \tag{114}$$

and consequently,

$$\frac{\partial I_2}{\partial \mathbf{F}} : \frac{\partial I_2}{\partial \mathbf{F}} = \left(8I_1 I_2 - 4J^2 I_1\right) \text{ and } \frac{\partial J}{\partial \mathbf{F}} : \frac{\partial J}{\partial \mathbf{F}} = I_1. \tag{115}$$

Combining (110), (111) and (115), we obtain the final expression for α_E in the 2D case

$$\alpha_E\left(I_1, I_2, J\right) = \frac{1}{4}\left[4I_1 \frac{\partial^2 \Phi}{\partial I_1 \partial I_1} + \left(8I_1 I_2 - 4J^2 I_1\right) \frac{\partial^2 \Phi}{\partial I_2 \partial I_2} + I_1 \frac{\partial^2 \Phi}{\partial J \partial J} + 16 I_2 \frac{\partial^2 \Phi}{\partial I_1 \partial I_2} + 8J \frac{\partial^2 \Phi}{\partial I_1 \partial J} + 2J I_1 \frac{\partial^2 \Phi}{\partial I_2 \partial J} + 8 \frac{\partial \Phi}{\partial I_1} + 2 I_1 \frac{\partial \Phi}{\partial I_2}\right]. \tag{116}$$

Similarly, the Cayley–Hamilton [56] in the 3D case states that $\mathbf{C} \in \mathbb{R}^{3\times 3}$ satisfies the following characteristic equation

$$\mathbf{C}^3 - I_1 \mathbf{C}^2 + I_2 \mathbf{C} - \det(\mathbf{C})\mathbf{I} = \mathbf{0}. \tag{117}$$

As a result, the following expressions can be obtained

$$\mathrm{tr}\left(\mathbf{C}^3\right) - I_1 \mathrm{tr}\left(\mathbf{C}^2\right) = 3J^2 - I_1 I_2 \text{ and } J^2 \mathrm{tr}\left(\mathbf{C}^{-1}\right) = I_2, \tag{118}$$

and, thus,

$$\frac{\partial I_2}{\partial \mathbf{F}} : \frac{\partial I_2}{\partial \mathbf{F}} = \left(4I_1 I_2 + 12J^2 I_1\right) \text{ and } \frac{\partial J}{\partial \mathbf{F}} : \frac{\partial J}{\partial \mathbf{F}} = I_2. \tag{119}$$

By combining (110), (111) and (119), we arrive at the final expression for α_E for the 3D case

$$\alpha_E\left(I_1, I_2, J\right) = \frac{1}{9}\left[4I_1 \frac{\partial^2 \Phi}{\partial I_1 \partial I_1} + \left(4I_1 I_2 + 12J^2\right) \frac{\partial^2 \Phi}{\partial I_2 \partial I_2} + I_2 \frac{\partial^2 \Phi}{\partial J \partial J} + 16 I_2 \frac{\partial^2 \Phi}{\partial I_1 \partial I_2} + 12J \frac{\partial^2 \Phi}{\partial I_1 \partial J} + 4J I_1 \frac{\partial^2 \Phi}{\partial I_2 \partial J} + 18 \frac{\partial \Phi}{\partial I_1} + 8 I_1 \frac{\partial \Phi}{\partial I_2}\right]. \tag{120}$$

Appendix B. On polyhedra with non star-convex faces

We provide detailed derivations of relations (81)–(84) in Section 4.7 when the polyhedral element E contains non star-convex faces. First, we are able to show that the utilized vertex-based quadrature rule on each face f can integrate

any linear functions exactly on f, even if f is not star-convex. Given any linear functions $\mathbf{p}_1$ in $[\mathcal{P}_1(E)]^3$, we can express it as $\mathbf{p}_1 = \mathbf{a} + \mathbf{B}\mathbf{X}$, where $\mathbf{a}$ and $\mathbf{B}$ are an arbitrary constant vector and a second order tensor, respectively. The exact face integral $\int_f \mathbf{p}_1 \otimes \mathbf{n}^f \mathrm{d}S$ is obtained as

$$\int_f \mathbf{p}_1 \otimes \mathbf{n}^f \mathrm{d}S = \int_f (\mathbf{a} + \mathbf{B}\mathbf{X}) \otimes \mathbf{n}^f \mathrm{d}S = |f| \left(\mathbf{a} + \mathbf{B}\mathbf{X}_C^f\right) \otimes \mathbf{n}^f, \tag{121}$$

where $\mathbf{X}_C^f$ is the centroid of face f. Applying the vertex based rule defined in (23) and (25) to the function $\mathbf{v} = \mathbf{p}_1$, we obtain

$$\begin{aligned}\sum_{j=1}^{m^f} \frac{|T_j^f|}{3} \left[\mathbf{p}_1\left(\mathbf{X}_j^f\right) + \mathbf{p}_1\left(\mathbf{X}_{j+1}^f\right) + \mathbf{p}_1\left(\mathbf{X}_s^f\right)\right] \otimes \mathbf{n}^f &= \sum_{j=1}^{m^f} \frac{|T_j^f|}{3} \left[3\mathbf{a} + \mathbf{B}\left(\mathbf{X}_j^f + \mathbf{X}_{j+1}^f + \mathbf{X}_s^f\right)\right] \otimes \mathbf{n}^f \\ = \left[\sum_{j=1}^{m^f} |T_j^f| \mathbf{a} + \mathbf{B}\left(\sum_{j=1}^{m^f} |T_j^f| \frac{\mathbf{X}_j^f + \mathbf{X}_{j+1}^f + \mathbf{X}_s^f}{3}\right)\right] &\otimes \mathbf{n}^f. \end{aligned} \tag{122}$$

Moreover, if we recall the definition of the signed area $|T_j^f|$ defined in (24), then we observe that for non star-convex faces

$$\sum_{j=1}^{m^f} |T_j^f| = |f|, \qquad \sum_{j=1}^{m^f} |T_j^f| \frac{\mathbf{X}_j^f + \mathbf{X}_{j+1}^f + \mathbf{X}_s^f}{3} = |f| \mathbf{X}_C^f, \tag{123}$$

and thus

$$\left[\sum_{j=1}^{m^f} |T_j^f| \mathbf{a} + \mathbf{B}\left(\sum_{j=1}^{m^f} |T_j^f| \frac{\mathbf{X}_j^f + \mathbf{X}_{j+1}^f + \mathbf{X}_s^f}{3}\right)\right] \otimes \mathbf{n}^f = |f| \left(\mathbf{a} + \mathbf{B}\mathbf{X}_C^f\right) \otimes \mathbf{n}^f = \int_f \mathbf{p}_1 \otimes \mathbf{n}^f \mathrm{d}S. \tag{124}$$

Notice that the above analysis also holds if f is not star-convex, implying that the vertex based quadrature rule is able to integrate any linear functions exactly even in those cases. This implies that (81) holds even if E contains non star-shaped faces.

Second, if the displacement field is linear, i.e. $\mathbf{u} = \mathbf{p}_1$, each deformed face $\widetilde{f}$ remains planar and the outward normal vector $\widetilde{\mathbf{n}}^f$ in the deformed configuration stays constant over each $\widetilde{f}$. Since the proofs of (82) and (83) for the "Simple" approach are more straightforward, we hereby prove the two expressions for the "Robust" approach. By applying $\mathbf{u} = \mathbf{p}_1$ to (41) and using (123), we obtain

$$\begin{aligned}\frac{1}{6|E|} \sum_{\widetilde{f}} \sum_{j=1}^{m^f} \left\{\widetilde{\mathbf{X}}_s^f \cdot \widetilde{\mathbf{X}}_j^f \wedge \widetilde{\mathbf{X}}_{j+1}^f\right\} &= \frac{1}{3|E|} \sum_{\widetilde{f}} \sum_{j=1}^{m^f} \left(|\widetilde{T}_j^f| \frac{\widetilde{\mathbf{X}}_j^f + \widetilde{\mathbf{X}}_{j+1}^f + \widetilde{\mathbf{X}}_s^f}{3}\right) \cdot \widetilde{\mathbf{n}}^f \\ &= \frac{1}{3|E|} \sum_{\widetilde{f}} \sum_{j=1}^{m^f} |\widetilde{f}| \widetilde{\mathbf{X}}_C^f \cdot \widetilde{\mathbf{n}}^f = \frac{1}{3|E|} \sum_{\widetilde{f}} \int_{\widetilde{f}} \widetilde{\mathbf{X}} \cdot \widetilde{\mathbf{n}}^f \mathrm{d}S = J_E(\mathbf{p}_1), \end{aligned} \tag{125}$$

where $|\widetilde{f}|$ is the (absolute) area of deformed face $\widetilde{f}$, and $\widetilde{\mathbf{X}}_C^f$ stands for the centroid of the deformed face $\widetilde{f}$. Again, no assumption is made whether f is star-convex with respect to $\mathbf{X}_s^f$, which proves relation (82) in Section 4.7.

Additionally, the first variation of $J_E(\mathbf{p}_1)$ with respect to any $\delta\mathbf{v}$ obtained in (42) can be recast as

$$\begin{aligned} DJ_E(\mathbf{u}) \cdot \delta\mathbf{v} &= \frac{1}{6|E|} \sum_{i=1}^{m} \left\{\delta\mathbf{v}(\mathbf{X}_i) \cdot \left[\sum_{\widetilde{f} \in \widetilde{\mathcal{F}}^i} \left(\beta_i^f \sum_{j=1}^{m_f} \widetilde{\mathbf{X}}_{j-1}^f \wedge \widetilde{\mathbf{X}}_j^f + \widetilde{\mathbf{X}}_s^f \wedge \left(\widetilde{\mathbf{X}}_{\mathcal{G}_f(i)-1}^f - \widetilde{\mathbf{X}}_{\mathcal{G}_f(i)+1}^f\right)\right)\right]\right\} \\ &= \frac{1}{6|E|} \sum_{f \in \partial E} \sum_{i=1}^{m^f} \delta\mathbf{v}\left(\mathbf{X}_i^f\right) \cdot \left[\beta^f \sum_{j=1}^{m^f} \widetilde{\mathbf{X}}_{j-1}^f \wedge \widetilde{\mathbf{X}}_j^f + \widetilde{\mathbf{X}}_s^f \wedge \left(\widetilde{\mathbf{X}}_{i-1}^f - \widetilde{\mathbf{X}}_{i-1}^f\right)\right] \end{aligned}$$

$$= \frac{1}{3|E|} \sum_{f\in\partial E} \sum_{i=1}^{m^f} \delta\mathbf{v}\left(\mathbf{X}_i^f\right) \cdot \left(\beta^f |\widetilde{f}| + |\widetilde{T}_j^f| + |\widetilde{T}_{j-1}^f|\right) \widetilde{\mathbf{n}}^f. \tag{126}$$

Pushing back the above expression to the undeformed configuration using the Nanson's formula [38] yields

$$\begin{aligned} DJ_E(\mathbf{u}) \cdot \delta\mathbf{v} &= \frac{1}{3|E|} \sum_{f\in\partial E} \sum_{i=1}^{m^f} \delta\mathbf{v}\left(\mathbf{X}_i^f\right) \cdot \left(\beta^f |\widetilde{f}| + |\widetilde{T}_j^f| + |\widetilde{T}_{j-1}^f|\right) \widetilde{\mathbf{n}}^f \\ &= \frac{1}{3|E|} \sum_{f\in\partial E} \sum_{i=1}^{m^f} \delta\mathbf{v}\left(\mathbf{X}_i^f\right) \cdot \left[\left(\beta^f |f| + |T_j^f| + |T_{j-1}^f|\right) \frac{\partial J}{\partial \mathbf{F}}(\mathbf{F}(\mathbf{p}_1))\, \mathbf{n}^f\right] \\ &= \frac{\partial J}{\partial \mathbf{F}}(\mathbf{F}(\mathbf{p}_1)) : \sum_{f\in\partial E} \sum_{i=1}^{m^f} w_i^f\, \delta\mathbf{v}\left(\mathbf{X}_i^f\right) \otimes \mathbf{n}^f = |E| \frac{\partial J}{\partial \mathbf{F}}(\mathbf{F}(\mathbf{p}_1)) : \Pi_E^0(\nabla(\delta\mathbf{v})), \end{aligned} \tag{127}$$

and therefore we prove (83).

Finally relation (84) in Section 4.7 can be derived as follows:

$$\begin{aligned} G_h^{\mathbf{v}}(\mathbf{p}_1, \widehat{p}_0, \delta\mathbf{v}_h) &= \sum_E |E| \left[\frac{\partial \Psi}{\partial \mathbf{F}}(\mathbf{F}(\mathbf{p}_1)) : \Pi_E^0 \nabla(\delta\mathbf{v}_h) + \widehat{q}_0|_E\, DJ_E(\mathbf{p}_1) \cdot \delta\mathbf{v}_h|_E\right] - \langle \mathbf{t}, \delta\mathbf{v}_h\rangle_h \\ &= \left[\frac{\partial \Psi}{\partial \mathbf{F}}(\mathbf{F}(\mathbf{p}_1)) + \frac{\partial U}{\partial J}(\mathbf{p}_1) \frac{\partial J}{\partial \mathbf{F}}(\mathbf{F}(\mathbf{p}_1))\right] : \sum_E |E| \Pi_E^0 \nabla(\delta\mathbf{v}_h) \\ &\quad - \sum_{f\in\Gamma_h^{\mathbf{t}}} \sum_{v\in f} w_v^f\, \mathbf{t}(\mathbf{X}_v) \cdot \delta\mathbf{v}_h(\mathbf{X}_v) \\ &= \mathbf{P} : \sum_E \sum_{f\in\partial E} \sum_{j=1}^{m^f} \left[w_j^f\, \delta\mathbf{v}_h\left(\mathbf{X}_j^f\right) \otimes \mathbf{n}^f\right] - \sum_{f\in\Gamma_h^{\mathbf{t}}} \sum_{j=1}^{m^f} w_j^f\, \mathbf{P}\mathbf{n}^f \cdot \delta\mathbf{v}_h\left(\mathbf{X}_j^f\right) \\ &= \mathbf{P} : \sum_{f\in\Gamma_h^{\mathbf{t}}} \sum_{j=1}^{m^f} \left[w_j^f\, \delta\mathbf{v}_h\left(\mathbf{X}_j^f\right) \otimes \mathbf{n}^f\right] \\ &\quad - \sum_{f\in\Gamma_h^{\mathbf{t}}} \sum_{j=1}^{m^f} w_j^f\, \mathbf{P}\mathbf{n}^f \cdot \delta\mathbf{v}_h\left(\mathbf{X}_j^f\right) = 0 \quad \forall \delta\mathbf{v}_h \in \mathcal{K}_h^0. \end{aligned} \tag{128}$$

Appendix C. Nomenclature

$\mathbf{P}$	First Piola–Kirchhoff stress tensor
$\mathbf{F}$	Deformation gradient tensor
$\mathbf{X}$	Position vector in the reference configuration
Ω	Undeformed configuration
$\Gamma^{\mathbf{X}}$	Part of the domain boundary where displacement $\mathbf{u}^0$ is prescribed
$\Gamma^{\mathbf{t}}$	Part of the domain boundary where traction $\mathbf{t}$ is prescribed
$\mathbf{f}$	Body force per unit undeformed volume
$\mathbf{t}$	Applied boundary traction per unit undeformed area
$W(\mathbf{X}, \mathbf{F})$	Stored-energy function
$U(\mathbf{X}, J)$	Volumetric part of the stored-energy function that depends only on $J = \det\mathbf{F}$
$\widehat{U}^*(\mathbf{X}, \widehat{q})$	Legendre transformed function of $U(\mathbf{X}, J)$ in J

(*continued on next page*)

$\Psi(\mathbf{X}, \mathbf{F})$	The remainder part of the stored-energy function
$\Pi(\mathbf{v})$	Potential energy in the displacement-based formulation
$\Pi_h^{VEM}(\mathbf{v}_h)$	VEM approximation of the potential energy in the displacement-based formulation
$\widehat{\Pi}(\mathbf{v}, \widehat{q})$	Potential energy in the mixed $\mathbf{F}$-formulation
$\widehat{\Pi}_h^{VEM}(\mathbf{v}_h, \widehat{q}_h)$	VEM approximation of the potential energy in the mixed $\mathbf{F}$-formulation
$\mathcal{K}$	Space of kinematically admissible displacements
$\mathcal{Q}$	Space consists of square integrable functions
Ω_h	A discretization of the domain Ω
$\Gamma_h^{\mathbf{t}}$	The boundary of the mesh where traction is applied
$\Gamma_h^{\mathbf{X}}$	The boundary of the mesh where displacement is applied
$\mathcal{K}_h$	Discrete global VEM displacement space
$\mathcal{Q}_h$	Discrete global VEM pressure space
E	A generic element of the mesh Ω_h in the undeformed configuration
f	A generic face of element E in the undeformed configuration
e	A generic edge of element E in the undeformed configuration
$\mathbf{X}_i$	The ith vertex of element E in the undeformed configuration
$\mathbf{X}_j^f$	The jth vertex on face f of element E with local numbering
$\mathbf{X}_s^f$	The triangulation point on face f of element E
T_j^f	The triangulated subfaces of f
$\mathcal{F}_i$	The set of faces that connect to $\mathbf{X}_i$ in E
$\mathcal{G}_f$	A map utilized to denote the relation between the global numbering and local numbering on f of element E
β_j^f	The weight associated with $\mathbf{X}_j^f$ in defining $\mathbf{X}_s^f$
$\mathbf{n}_e$	The outward normal of edge e in 2D in the undeformed configuration
∇	Gradient operator with respect to the undeformed configuration
Δ	Laplacian operator with respect to the undeformed configuration
$\mathbf{n}_f$	The outward normal of face f in 3D
w_j^f	The weight associated with $\mathbf{X}_j^f$ defined in a vertex-based quadrature rule to integration functions on f that is first order accurate
w_v^E	The weight associated with vertex v to integration functions over E that is first order accurate
$\mathcal{V}(E)$	Local VEM displacement space on element E
$\mathcal{P}_k(E)$	Polynomial space of order k on element E
Π_E^0	A tensor-valued $\mathcal{L}^2$ projection which projects second order tensors onto its average over E
Π_E^∇	A vector-valued projection which projects vectors from $\mathcal{V}(E)$ onto $[\mathcal{P}_1(E)]^d$
$\widetilde{\mathbf{X}}_i$	The ith vertex of element E in the deformed configuration
$\widetilde{\mathbf{X}}_j^f$	The jth vertex on face $\widetilde{f}$ of element $\widetilde{E}$ with local numbering
$\mathbf{X}_C^E$	The centroid of E
$\widetilde{E}$	A generic element of the mesh Ω_h in the deformed configuration
$\widetilde{f}$	A generic face of element $\widetilde{E}$ in the deformed configuration
$\widetilde{e}$	A generic edge of element $\widetilde{E}$ in the deformed configuration
$\widetilde{\mathbf{X}}_s^f$	The triangulation point on face $\widetilde{f}$ of element $\widetilde{E}$
$\widetilde{\mathcal{F}}_i$	The set of faces that connect to $\widetilde{\mathbf{X}}_i$ in $\widetilde{E}$
$\widetilde{\mathbf{n}}_e$	The outward normal of edge $\widetilde{e}$ in 2D
$\widetilde{\nabla}$	Gradient operator with respect to the deformed configuration
$\widetilde{\mathbf{n}}_f$	The outward normal of face $\widetilde{f}$ in 3D
$\widetilde{T}_j^f$	The triangulated subfaces of $\widetilde{f}$
J_E	The area/volume average of $J = \det \mathbf{F}$ over E
$S_{h,E}(\cdot, \cdot)$	Bilinear form in the stabilization term associated with E

(*continued on next page*)

α_E	Stabilization parameter associated with E
d	Dimension
$\mathbf{u}_h$	Equilibrium displacement field
$\mathbf{u}_h^{n-1}$	Equilibrium displacement field obtained in the previous Newton–Raphson step
$\mathbf{C}$	Right Cauchy deformation tensor $\mathbf{C} = \mathbf{F}^T\mathbf{F}$
I_1	First invariant of the right Cauchy deformation tensor $\mathbf{C}$
I_2	Second invariant of the right Cauchy deformation tensor $\mathbf{C}$
J	Determinant of deformation gradient $J = \det \mathbf{F}$
$\phi(I_1, I_2, J)$	Another form of $\Psi(\mathbf{F})$ that depends solely on the invariants $I_1 I_2$ and J for isotropic solids
$\epsilon_{0,\mathbf{u}}$	The $\mathcal{L}^2$-norm of the displacement error
$\epsilon_{1,\mathbf{u}}$	The $\mathcal{H}^1$-seminorm of the displacement error
$\epsilon_{0,\widehat{p}}$	The $\mathcal{L}^2$-norm of the pressure error
$\epsilon^v_{0,\mathbf{u}}$	The $\mathcal{L}^2$-type displacement error using only vertex values
$\epsilon^v_{1,\mathbf{u}}$	The $\mathcal{H}^1$-type displacement error using only vertex values
$\epsilon^v_{0,\widehat{p}}$	The $\mathcal{L}^2$-type pressure error

References

[1] A. Aggarwal, E.R. May, C.L. Brooks III, W.S. Klug, Nonuniform elastic properties of macromolecules and effect of prestrain on their continuum nature, Phys. Rev. E 93 (1) (2016) 012417.

[2] J.E. Bishop, Simulating the pervasive fracture of materials and structures using randomly close packed voronoi tessellations, Comput. Mech. 44 (4) (2009) 455–471.

[3] N. Sukumar, J.E. Bolander, Voronoi-based interpolants for fracture modelling, in: Tessellations in the Sciences: Virtues, Techniques and Applications of Geometric Tilings, Springer Verlag, 2009.

[4] D.W. Spring, S.E. Leon, G.H. Paulino, Unstructured polygonal meshes with adaptive refinement for the numerical simulation of dynamic cohesive fracture, Int. J. Fract. 189 (1) (2014) 33–57.

[5] S.E. Leon, D.W. Spring, G.H. Paulino, Reduction in mesh bias for dynamic fracture using adaptive splitting of polygonal finite elements, Internat. J. Numer. Methods Engrg. 100 (8) (2014) 555–576.

[6] C. Talischi, G.H. Paulino, A. Pereira, I.F.M. Menezes, PolyTop: a Matlab implementation of a general topology optimization framework using unstructured polygonal finite element meshes, Struct. Multidiscip. Optim. 45 (3) (2012) 329–357.

[7] C. Talischi, G.H. Paulino, C.H. Le, Honeycomb Wachspress finite elements for structural topology optimization, Struct. Multidiscip. Optim. 37 (6) (2009) 569–583.

[8] C. Talischi, G.H. Paulino, A. Pereira, I.F.M. Menezes, Polygonal finite elements for topology optimization: A unifying paradigm, Internat. J. Numer. Methods Engrg. 82 (2010) 671–698.

[9] C Talischi, A Pereira, G.H. Paulino, I.F.M. Menezes, M.S. Carvalho, Polygonal finite elements for incompressible fluid flow, Internat. J. Numer. Methods Fluids 74 (2014) 134–151.

[10] S.O.R. Biabanaki, A.R. Khoei, P. Wriggers, Polygonal finite element methods for contact-impact problems on non-conformal meshes, Comput. Methods Appl. Mech. Engrg. 269 (2014) 198–221.

[11] S.O.R. Biabanaki, A.R. Khoei, A polygonal finite element method for modeling arbitrary interfaces in large deformation problems, Comput. Mech. 50 (1) (2012) 19–33.

[12] H. Chi, C. Talischi, O. Lopez-Pamies, G.H. Paulino, Polygonal finite elements for finite elasticity, International Journal for Numerical Methods in Engineering 101 (2015) 305–328.

[13] H. Chi, C. Talischi, O. Lopez-Pamies, G.H. Paulino, A paradigm for higher order polygonal elements in finite elasticity, Comput. Methods Appl. Mech. Engrg. 306 (2016) 216–251.

[14] M. Floater, A. Gillette, N. Sukumar, Gradient bounds for Wachspress coordinates on polytopes, SIAM J. Numer. Anal. 52 (1) (2014) 515–532.

[15] Michael Floater, Géza Kós, Martin Reimers, Mean value coordinates in 3D, Comput. Aided Geom. Design 22 (7) (2005) 623–631.

[16] P. Joshi, M. Meyer, T. DeRose, B. Green, T. Sanocki, Harmonic coordinates for character articulation, in: ACM Transactions on Graphics, vol. 26, ACM, 2007, p. 71.

[17] Sebastian Martin, Peter Kaufmann, Mario Botsch, Martin Wicke, Markus Gross, Polyhedral finite elements using harmonic basis functions, Comput. Graph. Forum 27 (5) (2008) 1521–1529.

[18] J. Bishop, A displacement-based finite element formulation for general polyhedra using harmonic shape functions, Internat. J. Numer. Methods Engrg. 97 (1) (2014) 1–31.

[19] M. Arroyo, M. Ortiz, Local maximum-entropy approximation schemes: a seamless bridge between finite elements and meshfree methods, Internat. J. Numer. Methods Engrg. 65 (13) (2006) 2167–2202.

[20] K. Hormann, N. Sukumar, Maximum entropy coordinates for arbitrary polytopes, in: Eurographics Symposium on Geometry Processing, vol. 27, 2008, pp. 1513–1520.

[21] N Sukumar, Quadratic maximum-entropy serendipity shape functions for arbitrary planar polygons, Comput. Methods Appl. Mech. Engrg. 263 (2013) 27–41.
[22] C. Talischi, G.H. Paulino, Addressing integration error for polygonal finite elements through polynomial projections: A patch test connection, Math. Models Methods Appl. Sci. 24 (08) (2014) 1701–1727.
[23] C. Talischi, A. Pereira, I.F.M Menezes, G.H. Paulino, Gradient correction for polygonal and polyhedral finite elements, Internat. J. Numer. Methods Engrg. 102 (3–4) (2015) 728–747.
[24] G. Manzini, A. Russo, N. Sukumar, New perspective on polygonal and polyhedral finite element method, Math. Models Methods Appl. Sci. 24 (08) (2014) 1665–1699.
[25] L. Beirão da Veiga, F. Brezzi, A. Cangiani, G. Manzini, L.D. Marini, A. Russo, Basic principles of virtual element methods, Math. Models Methods Appl. Sci. 23 (1) (2013) 199–214.
[26] L. Beirão da Veiga, F. Brezzi, L.D. Marini, A. Russo, The hitchhiker's guide to the virtual element method, Math. Models Methods Appl. Sci. 24 (08) (2014) 1541–1573.
[27] L. Beirão da Veiga, F. Brezzi, L.D. Marini, Virtual elements for linear elasticity problems, SIAM J. Numer. Anal. 51 (2) (2013) 794–812.
[28] Lourenco Beirão da Veiga, Gianmarco Manzini, A virtual element method with arbitrary regularity, IMA J. Numer. Anal. 34 (2) (2014) 759–781.
[29] F. Brezzi, L.D. Marini, Virtual element methods for plate bending problems, Computer Methods in Applied Mechanics and Engineering 253 (2013) 455–462.
[30] A.L. Gain, C. Talischi, G.H. Paulino, On the virtual element method for three-dimensional linear elasticity problems on arbitrary polyhedral meshes, Computer Methods in Applied Mechanics and Engineering 282 (2014) 132–160.
[31] F. Brezzi, R.S. Falk, L. Donatella Marini, Basic principles of mixed virtual element methods, ESAIM Math. Model. Numer. Anal. 48 (04) (2014) 1227–1240.
[32] L. Beirão da Veiga, F. Brezzi, L.D. Marini, A. Russo, Virtual element method for general second-order elliptic problems on polygonal meshes, Mathematical Models and Methods in Applied Sciences 26 (2014) 729–750.
[33] David Mora, Gonzalo Rivera, Rodolfo Rodríguez, A virtual element method for the Steklov eigenvalue problem, Math. Models Methods Appl. Sci. 25 (8) (2015) 1421–1445.
[34] M.F. Benedetto, S. Berrone, S. Pieraccini, S. Scialò, The virtual element method for discrete fracture network simulations, Comput. Methods Appl. Mech. Engrg. 280 (2014) 135–156.
[35] L. Beirão da Veiga, C. Lovadina, D. Mora, A virtual element method for elastic and inelastic problems on polytope meshes, Comput. Methods Appl. Mech. Engrg. 295 (2015) 327–346.
[36] P.F. Antonietti, L. Beirao da Veiga, S. Scacchi, M. Verani, A C^1 Virtual element method for the Cahn–Hilliard equation with polygonal meshes, SIAM J. Numer. Anal. 54 (1) (2016) 34–56.
[37] P. Wriggers, W.T. Rust, B.D. Reddy, A virtual element method for contact, Comput. Mech. 58 (6) (2016) 1039–1050.
[38] R.W. Ogden, Nonlinear Elastic Deformations, Courier Dover Publications, 1997.
[39] R.W. Ogden, Volume changes associated with the deformation of rubber-like solids, J. Mech. Phys. Solids 24 (6) (1976) 323–338.
[40] R.W. Ogden, Nearly isochoric elastic deformations: application to rubberlike solids, J. Mech. Phys. Solids 26 (1) (1978) 37–57.
[41] J.C. Simo, R.L. Taylor, K.S. Pister, Variational and projection methods for the volume constraint in finite deformation elasto-plasticity, Computer Methods in Applied Mechanics and Engineering 51 (1) (1985) 177–208.
[42] U. Brink, E. Stein, On some mixed finite element methods for incompressible and nearly incompressible finite elasticity, Comput. Mech. 19 (1) (1996) 105–119.
[43] B. Ahmad, A. Alsaedi, F. Brezzi, L.D. Marini, A. Russo, Equivalent projectors for virtual element methods, Comput. Math. Appl. 66 (3) (2013) 376–391.
[44] L. Beirão da Veiga, K. Lipnikov, A mimetic discretization of the Stokes problem with selected edge bubbles, SIAM J. Sci. Comput. 32 (2) (2010) 875–893.
[45] D.S. Malkus, T.J.R. Hughes, Mixed finite element methods–reduced and selective integration techniques: a unification of concepts, Computer Methods in Applied Mechanics and Engineering 15 (1) (1978) 63–81.
[46] M.S. Floater, Mean value coordinates, Comput. Aided Geom. Design 20 (1) (2003) 19–27.
[47] M.A. Crisfield, Non-Linear Finite Element Analysis of Solids and Structures: Advanced Topics, John Wiley & Sons, Inc., 1997.
[48] C. Talischi, G.H. Paulino, A. Pereira, I.F.M. Menezes, PolyMesher: A general-purpose mesh generator for polygonal elements written in Matlab, Struct. Multidiscip. Optim. 45 (3) (2012) 309–328.
[49] R.S. Thedin, A. Pereira, I.F. Menezes, G.H. Paulino, Polyhedral mesh generation and optimization for finite element computations, in: Proceedings of the XXXV Ibero-Latin American Congress on Computational Methods in Engineering, 2014.
[50] G.H. Paulino, A.L. Gain, Bridging art and engineering using Escher-based virtual elements, Struct. Multidiscip. Optim. 51 (4) (2015) 867–883.
[51] O Lopez-Pamies, A new I_1-based hyperelastic model for rubber elastic materials, C. R. Mecanique 338 (1) (2010) 3–11.
[52] J. Segurado, J. Llorca, A numerical approximation to the elastic properties of sphere-reinforced composites, J. Mech. Phys. Solids 50 (10) (2002) 2107–2121.
[53] O. Lopez-Pamies, T. Goudarzi, K. Danas, The nonlinear elastic response of suspensions of rigid inclusions in rubber: II—A simple explicit approximation for finite-concentration suspensions, J. Mech. Phys. Solids 61 (2013) 19–37.
[54] H. Chi, O. Lopez-Pamies, G.H. Paulino, A variational formulation with rigid-body constraints for finite elasticity: Theory, finite element implementation, and applications, Comput. Mech. 57 (2016) 325–338.
[55] T. Goudarzi, D.W. Spring, G.H. Paulino, O. Lopez-Pamies, Filled elastomers: A theory of filler reinforcement based on hydrodynamic and interphasial effects, J. Mech. Phys. Solids 80 (2015) 37–67.
[56] M.E. Gurtin, An Introduction to Continuum Mechanics, vol. 158, Academic press, 1982.